Detailed modelling of innovative solutions for producing and using renewable fuels like hydrogen and biomethane

Politecnico di Bari

Department of Mechanics, Mathematics and Management
MECHANICAL AND MANAGEMENT ENGINEERING
Ph.D. Program
SSD: ING-IND/08–FLUID MACHINERY

Final Dissertation

Detailed modelling of innovative solutions for producing and using renewable fuels like hydrogen and biomethane

---

by
Vincenzo Di Domenico

Supervisors:

Prof. Riccardo Amirante

Prof. Paolo Tamburrano

Coordinator of Ph.D. Program:
Prof. Giuseppe Casalino

Course n°38, 01/01/2023-31/12/2025

Politecnico di Bari

Department of Mechanics, Mathematics and Management
MECHANICAL AND MANAGEMENT ENGINEERING
Ph.D. Program
SSD: ING-IND/08–FLUID MACHINERY

Final Dissertation

Detailed modelling of innovative solutions for producing and using renewable fuels like hydrogen and biomethane

by
Vincenzo Di Domenico:
Vincenzo Di Domenico

Referees:
Prof. Nathan P. Sell
Prof. Barbara Zardin

Supervisors:
Prof. Riccardo Amirante
Prof. Paolo Tamburrano

Coordinator of Ph.D Program:
Prof. Giuseppe Casalino

Course n°38, 01/01/2023-31/12/2025

Politecnico di Bari

LIBERATORIA PER L'ARCHIVIAZIONE DELLA TESI DI DOTTORATO

Al Magnifico Rettore
del Politecnico di Bari

Il sottoscritto Vincenzo Di Domenico nato a Terlizzi il 17/08/1996

residente a Ruvo di Puglia in via Giovanni Liberatore, 58 e-mail numberonevins96@gmail.com

iscritto al 3° anno di Corso di Dottorato di Ricerca in Ingegneria Meccanica e Gestionale (DRIMEG) ciclo XXXVIII

ed essendo stato ammesso a sostenere l'esame finale con la prevista discussione della tesi dal titolo:

"Modellazione dettagliata di soluzioni innovative per produzione e utilizzo di combustibili rinnovabili quali idrogeno e biometano"

DICHIARA

1) di essere consapevole che, ai sensi del D.P.R. n. 445 del 28.12.2000, le dichiarazioni mendaci, la falsità negli atti e l'uso di atti falsi sono puniti ai sensi del codice penale e delle Leggi speciali in materia, e che nel caso ricorressero dette ipotesi, decade fin dall'inizio e senza necessità di nessuna formalità dai benefici conseguenti al provvedimento emanato sulla base di tali dichiarazioni;
2) di essere iscritto al Corso di Dottorato di ricerca in Ingegneria Meccanica e Gestionale (DRIMEG) ciclo XXXVIII, corso attivato ai sensi del "*Regolamento dei Corsi di Dottorato di ricerca del Politecnico di Bari*", emanato con D.R. n.286 del 01.07.2013;
3) di essere pienamente a conoscenza delle disposizioni contenute nel predetto Regolamento in merito alla procedura di deposito, pubblicazione e autoarchiviazione della tesi di dottorato nell'Archivio Istituzionale ad accesso aperto alla letteratura scientifica;
4) di essere consapevole che attraverso l'autoarchiviazione delle tesi nell'Archivio Istituzionale ad accesso aperto alla letteratura scientifica del Politecnico di Bari (IRIS-POLIBA), l'Ateneo archivierà e renderà consultabile in rete (nel rispetto della Policy di Ateneo di cui al D.R. 642 del 13.11.2015) il testo completo della tesi di dottorato, fatta salva la possibilità di sottoscrizione di apposite licenze per le relative condizioni di utilizzo (di cui al sito http://www.creativecommons.it/Licenze), e fatte salve, altresì, le eventuali esigenze di "embargo", legate a strette considerazioni sulla tutelabilità e sfruttamento industriale/commerciale dei contenuti della tesi, da rappresentarsi mediante compilazione e sottoscrizione del modulo in calce (Richiesta di embargo);
5) che la tesi da depositare in IRIS-POLIBA, in formato digitale (PDF/A) sarà del tutto identica a quelle **consegnate**/inviate/da inviarsi ai componenti della commissione per l'esame finale e a qualsiasi altra copia depositata presso gli Uffici del Politecnico di Bari in forma cartacea o digitale, ovvero a quella da discutere in sede di esame finale, a quella da depositare, a cura dell'Ateneo, presso le Biblioteche Nazionali Centrali di Roma e Firenze e presso tutti gli Uffici competenti per legge al momento del deposito stesso, e che di conseguenza va esclusa qualsiasi responsabilità del Politecnico di Bari per quanto riguarda eventuali errori, imprecisioni o omissioni nei contenuti della tesi;
6) che il contenuto e l'organizzazione della tesi è opera originale realizzata dal sottoscritto e non compromette in alcun modo i diritti di terzi, ivi compresi quelli relativi alla sicurezza dei dati personali; che pertanto il Politecnico di Bari ed i suoi funzionari sono in ogni caso esenti da responsabilità di qualsivoglia natura: civile, amministrativa e penale e saranno dal sottoscritto tenuti indenni da qualsiasi richiesta o rivendicazione da parte di terzi;
7) che il contenuto della tesi non infrange in alcun modo il diritto d'Autore né gli obblighi connessi alla salvaguardia di diritti morali od economici di altri autori o di altri aventi diritto, sia per testi, immagini, foto, tabelle, o altre parti di cui la tesi è composta.

Luogo e data Bari, 02/03/2026 Firma Vincenzo Di Domenico

Il/La sottoscritto, con l'autoarchiviazione della propria tesi di dottorato nell'Archivio Istituzionale ad accesso aperto del Politecnico di Bari (POLIBA-IRIS), pur mantenendo su di essa tutti i diritti d'autore, morali ed economici, ai sensi della normativa vigente (Legge 633/1941 e ss.mm.ii.),

CONCEDE

- al Politecnico di Bari il permesso di trasferire l'opera su qualsiasi supporto e di convertirla in qualsiasi formato al fine di una corretta conservazione nel tempo. Il Politecnico di Bari garantisce che non verrà effettuata alcuna modifica al contenuto e alla struttura dell'opera.
- al Politecnico di Bari la possibilità di riprodurre l'opera in più di una copia per fini di sicurezza, back-up e conservazione.

Luogo e data Bari, 02/03/2026 Firma Vincenzo Di Domenico

This work has been supported under the National Recovery and Resilience Plan (NRRP), Mission 4, Component 2, Investment 1.4—Call for tender No. 3138 of 16 December 2021 of the Italian Ministry of University and Research, funded by the European Union—NextGenerationEU [Award Number: CNMS named MOST, Concession Decree No. 1033 of 17 June 2022, adopted by the Italian Ministry of University and Research, CUP: D93C22000410001, Spoke 14 ‘‘Hydrogen and New Fuels’’].

Abstract

This PhD research has the aim to develop novel and innovative technologies, in the context of an increasing interest in renewable energy production and utilisation. As the traditional methods, in most of the cases, are considered polluting and low-efficient, this study was conducted under the guiding principle of achieving a zero-carbon footprint. The first objective is to devise strategies for producing conventional fuels—such as methane—in a manner that ensures the overall lifecycle of the fuel results in a net-zero CO_2 balance. Fuels produced through such processes can be classified as "biofuels". More specifically, an innovative production strategy for biomethane has been developed, making use of a novel architecture – i.e. the pipe-in-pipe architecture – and optimisation algorithms, to ensure the best compromise between performance and compactness of the system.

Furthermore, Hydrogen is increasingly considered a promising alternative energy carrier due to its potential for zero carbon emissions. Its high energy content makes it attractive for applications such as aviation, railways and automotive. This research work focused on aviation. Nevertheless, challenges remain in storage and handling because of the physical properties of hydrogen: its low density imposes a storage in liquid form, which is, on the other hand, hard to maintain, because of the low temperatures required. Research efforts have focused on overcoming these obstacles, with preliminary models and strategies developed to ensure efficient and reliable integration into energy systems.

Another focus was on the vaporizer, which was designed to meet the operative conditions of the aforementioned fuel system. To minimise the occupied volume for the vaporizer on board, the pipe-in-pipe architecture was again used, along with a parametric tuning of the numeric model, thus allowing to obtain a limited total volume for the pipes along with an enhanced performance, also ensuring that the material constituting the tubes could successfully withstand the pressure imposed by the system.

Table of Contents

1. INTRODUCTION

This chapter gives an overview of the research work carried during my doctoral studies. First the environmental challenges are brought to the evidence, in relation with the need to approach to a zero-emission scenario, by means of an innovative approach to obtain traditional fuels (specifically methane), which, compared with the conventionally obtained ones, result to have a zero-carbon net footprint, considering their entire lifecycle.

In second place, hydrogen is taken under consideration as an alternative and clean fuel. One of the most promising applications for hydrogen is aviation: the latter is considered in my work and a novel aircraft fuel system powered by hydrogen is presented. Because of the physical limitations given by the nature of hydrogen itself, there is the need to store it in liquid form and deliver it in gaseous form inside the fuel system. This implies a complication in the metering process, which is handled with the use of a convergent divergent nozzle with supersonic flow.

1.1. Environmental challenges and fuels for the future

The current global scenario is pushing in the last decades towards sustainable alternatives, which implies as a first step the reduction of the carbon emissions. This could be achieved with renewable energy sources, as well as with ***biofuels***. It is possible to define a fuel as biofuel, when this is obtained by means of processes that are able to withdraw some CO_2 from the environment and use it to synthetise the fuel itself. This implies the fact that after the biofuel has been combusted, the CO_2 net balance is equal to zero.

In accordance with European Union policies on energy security and decarbonization, Italy has promoted biomethane production since 2018 through the implementation of the Biomethane Decree, which recognizes the strategic role of biomethane derived from agricultural and agro-industrial sources[1], [2]. Biomethane is of particular interest due to its near carbon-neutral nature, as it is obtained by upgrading biogas through the separation of methane (CH_4) from carbon dioxide (CO_2) and other minor components produced during anaerobic digestion. The separation of multiphase and multicomponent systems is commonly investigated through fluid-dynamic analyses, as discussed in [3]. Depending on the upgrading technology, biomethane purities between 95% and 98% can be achieved.

Following upgrading, biomethane liquefaction represents a crucial step in the supply chain. As highlighted in [4], pipeline transport may be ineffective or infeasible in several contexts [5]. Liquefaction significantly increases fuel density and reduces storage volume, thereby enabling more efficient transportation and facilitating its use in heavy-duty applications, such as trucks and ships. In addition, studies reported in [2] indicate that transporting liquid biomethane can be more cost-effective than transporting compressed gaseous biomethane. Several liquefaction technologies have been proposed and compared in the literature; for instance, [6] presents a thermodynamic assessment of five different liquefaction processes.

Biomethane is chemically equivalent to natural gas and can therefore replace it across a wide range of applications, including power generation—particularly in small-scale plants [7], [8]—as well as light- and heavy-duty transportation. Its large-scale deployment could reduce dependence on imported natural gas and contribute to long-term carbon-neutrality goals, with positive environmental impacts [9], [10]. To enable a significant increase in biomethane availability, both upgrading and liquefaction processes are currently the subject

of intensive research. In parallel, novel feedstocks are being investigated to further expand biomethane production, as shown in [11], [12], [13].

Liquefaction technologies are well established in the natural gas sector, with both large-scale and small-scale plants implementing a wide range of technical solutions [14]. However, due to the limited flow rates typical of biomethane upgrading plants, only small-scale liquefaction technologies are suitable for biomethane applications. This constraint has led to increasing interest in small-scale liquefaction systems, which are now widely addressed in recent research studies [15], [16], [17], [18].

Among small-scale liquefaction processes, the Single Mixed Refrigerant (SMR) cycle—particularly the Poly Refrigerated Integrated Cycle (PRICO)—is the most widely adopted. Its application to small-scale plants has been investigated from exergetic and economic perspectives in [19] and [20]. Much of the literature focuses on optimizing heat-exchanger configurations within the PRICO process, typically formulated as a multi-objective optimization problem [21]. Moreover, [22] highlights the strong dependence of process performance on the mixed-refrigerant composition and ambient conditions, while further optimization studies addressing operating parameters and mixture compositions are reported in [23], [24], [25], [26], [27], [28], [29], [30].

Cryogenic heat exchangers play a central role in liquefaction systems. A comprehensive review of cryogenic heat exchanger technologies is provided in [31], with particular emphasis on recent advances in liquefaction and on the two main designs currently employed: coil-wound and plate-fin heat exchangers. Despite their high thermal performance, these components are associated with considerable manufacturing costs, which significantly affect the economic feasibility of small-scale plants.

In this framework, this research work investigates a novel SMR-based liquefaction process that shares conceptual similarities with the PRICO cycle, relying on a closed thermodynamic loop including compression, cooling, expansion, and heat exchange of a mixed refrigerant. Unlike conventional approaches, simpler heat exchanger designs are adopted, with the aim of reducing capital costs compared to more complex solutions such as cascade processes, whose limited suitability for small-scale applications has been demonstrated in [32].

The proposed biomethane liquefaction plant was first introduced and partially analysed in [33], while its performance under fixed operating conditions was further assessed in[34]. In that study, an overall coefficient of performance of approximately 0.26 was reported for a biomethane mass flow rate of 0.03 kg/s, representing a competitive value with respect to current commercial biomethane liquefaction technologies. Building on these previous investigations, the present study extends the analysis by examining the influence of key operating parameters on plant performance. A parametric analysis is therefore conducted with the dual objective of maximizing the overall coefficient of performance and minimizing the total heat-exchanger length, using the analytical model developed in [33] and [34].

1.2. An innovative hydrogen-based aircraft fuel system

Hydrogen-based propulsion offers several pathways to more environmentally sound, next-generation aircraft [35], [36], [37], [38]. To that effect, several feasibility studies have suggested that a 50–90% reduction in flight emissions is possible in the next 10–15 years for aircraft leveraging hydrogen combustion or fuel cell technology compared to forecasts for kerosene-fuelled aircraft [39]. At present, the combustion route is a more practical option for a wider array of aircraft due to insufficient hydrogen fuel cell power densities [35], [39]. Aircraft powered by hydrogen combustion are also envisioned to have a large technology

overlap with existing kerosene designs, which aids development and adoption of the technology in the short term. Indeed, companies such as Moog, Eaton Aerospace, and Parker Aerospace, well established in the fluid power domain, are also extremely active in the emerging field of hydrogen fuel systems. On this path, the present research work aims to give a contribution to the development of a new technology, capable of implementing hydrogen as a fuel for a fuel system mounted on board of an aircraft. The main issues related to this technology would be:

- Extremely low density (0.082 kg/m^3 at 1 atm and 25 °C) for gaseous hydrogen to be stored in a tank on board, which implies a low quantity of fuel compared to the requirements for a continental flight
- To minimise the occupied volume and, therefore, maximise the content of fuel available on the aircraft, liquid storage is considered, thus implying the need to maintain the liquid form, which is stable for temperatures lower than 33 K
- The difficulty to maintain the liquid form given its low temperature, implies the need to perform the vaporization after the withdraw from the tank, meaning that the fuel needs to be handled in compressible state, which is dependant from the pressure and the temperature of the fuel.
- The compressibility of the fuel during the metering phase implies that a robust method needs to be developed to control the exact mass flow rate needed, based on the requirements of the user.

These issues have been faced, and a preliminary model has been presented, along with preliminary simulated results. In addition, two of the components in the fuel system, namely the metering valve and the vaporizer heat exchanger, are focused with specifical considerations.

1.3. Research Contribution

The original contributions of my research work are listed below:

- ✓ Creating a numerical model and a calculation code, allowing to parametrise and optimise a biomethane liquefaction plant from a performative perspective as well as for a reduced a total occupied volume, also taking into account for the thermodynamical transformations of the species involved
- ✓ Creating a numerical model and calculation code, allowing to parametrise and optimise a heat exchanger with the aim to vaporize hydrogen by using nitrogen as the heat carrier fluid. The model has been tuned to obtain the minimum occupied volume and the minimum mass of the system, also taking into account for the thermodynamical transformations of the species involved
- ✓ Creating a numerical and thermodynamical model for an innovative aircraft fuel system powered with hydrogen and capable of simulating variable flight conditions and, for those conditions, returning the time evolution of the main parameters characterising the system. The system is driven by a double closed loop control, implemented by PI controllers, in order to properly regulate the rotational speed of the centrifugal pump and, at the same time, the opening degree of the metering valve, which is modelled as a convergent-divergent nozzle, with supersonic flow happening

1.4. List of publications

In this section, a list of the publications authored and co-authored by the thesis author is presented:

1. Di Domenico, V., Tamburrano, P., Distaso, E., Sciatti, F., & Amirante, R. (2023). Detailed performance analysis of a novel small-scale biomethane liquefaction plant. *Journal of Physics: Conference Series*, *2648*(1), 012014. [40]
2. Sciatti, F., Di Domenico, V., Zagaria, L., Adeyemi, D., Tamburrano, P., Plummer, A., Sell, N., Distaso, E., & Amirante, R. (2024). PRELIMINARY DESIGN AND MODELLING OF A HYDROGEN-POWERED AIRCRAFT FUEL SYSTEM. *FPMC 2024*. [41]
3. Di Domenico, V., Tamburrano, P., Sciatti, F., Distaso, E., Foglia, M. M., & Amirante, R. (2024). A Novel Hydrogen-Nitrogen Heat Exchanger For Aeronautical Applications. *Journal of Physics: Conference Series*, *2893*(1), 012082. [42]
4. Sciatti, F., Di Domenico, V., Tamburrano, P., Distaso, E., & Amirante, R. (2025). An Innovative Cryogenic Heat Exchanger Design for Sustainable Aviation. *Energies 2025, Vol. 18, Page 1261*, *18*(5), 1261. [43]
5. Sciatti, F., di Domenico, V., Tamburrano, P., Caprioli, E., Distaso, E., & Amirante, R. (2025). Simulation and Control of an Advanced Metering Valve for Hydrogen-Powered Aircraft Fuel Systems Using Simscape Language. *Journal of Physics: Conference Series*, *3143*(1), 012067. [44]
6. Di Domenico, V., Sciatti, F., Tamburrano, P., Distaso, E., & Amirante, R. (2025). Optimization of a novel biomethane small-scale liquefaction plant by means of a Multi-Objective Genetic Algorithm. *Journal of Physics: Conference Series*, *3143*(1), 012021. [45]
7. Sciatti, F., Di Domenico, V., Tamburrano, P., Sell, N., Plummer, A. R., Distaso, E., ... & Amirante, R. (2024, June). Numerical Analysis of a High-Power Piezoelectric Pump using Computational Fluid Dynamics (CFD) Simulations. In *Global Fluid Power Society Symposium* (pp. 289-303). Cham: Springer Nature Switzerland.[46]
8. Sciatti, F., Di Domenico, V., Tamburrano, P., Sell, N., Plummer, A. R., Distaso, E., ... & Amirante, R. (2024, November). Investigation of Cavitation Phenomena in a "High-Power" Piezohydraulic Pump: A Computational Fluid Dynamics (CFD) Approach. In *Journal of Physics: Conference Series* (Vol. 2893, No. 1, p. 012060). IOP Publishing.[47]

2. LITERATURE REVIEW

In this chapter, a literature review encompassing the research strands carried out in my doctoral studies is proposed. In the first section of the chapter, all the technologies related to the liquefaction plants are considered. Subsequently, the state of the art for the green-powered aviation will be described, with particular reference to the role of hydrogen in the global transition, towards a sustainable global model.

2.1. Liquefaction technologies

The liquefaction of methane, and in general of natural gases, is performed with the use of three different technologies, illustrated below. The product of the liquefaction is called Liquid Natural Gas (LNG).

1. ***Cascade processes***, which consist in subtracting heat from the fuel with independent and subsequent refrigerant loops, with decreasing working temperatures, until the liquid point is not reached (see **Figure 1**).

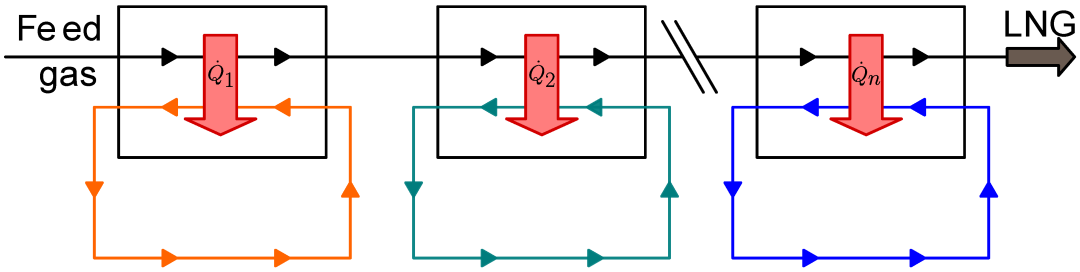

Figure 1. *Generic working principle of a cascade liquefaction process.*

2. ***Single Mixed Refrigerant*** technology (**SMR**) is inspired from the cascade technology, but in this case, there is a unique refrigerant loop, where the refrigerant is a mixture of several refrigerants in a fixed ratio (see **Figure 2**).

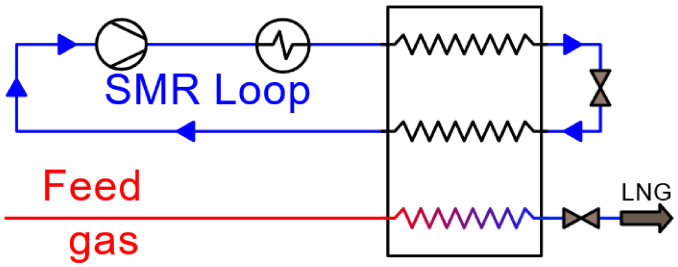

Figure 2. *Generic working principle of the Single Mixed Refrigerant process.*

3. ***Gas expansion processes***, make use of mechanical expanders in place of Joule-Thompson valves and in most of the applications, the used refrigerant is Nitrogen. Because of its ease of implementation and compactness, this technology is widely used for offshore liquefaction plants. An example of schematic can be observed in **Figure 3**.

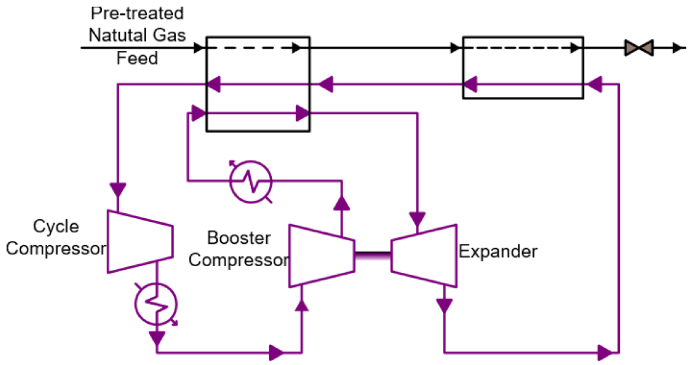

***Figure 3**. Generic schematic for gas expansion processes.*

2.1.1. Cascade processes

Historically, cascade processes were the first method implemented for producing liquefied natural gas. The first plant was created in 1964, on behalf of Compangnie Algerienne de Methane Liquide (CAMEL) [47], [48]. The process involved three distinct cooling stages: initially, a propane cycle reduced the gas temperature to −30 °C; next, an ethylene cycle cooled it further to approximately −100 °C; finally, a methane cycle brought the gas to its liquid state at about −160 °C, ready for the shipping or the transportation in general. To drive the compressors, steam turbines were used and seawater was used to perform condensation of the same steam [49]. **Figure 4** illustrates the architecture of the plant mentioned above.

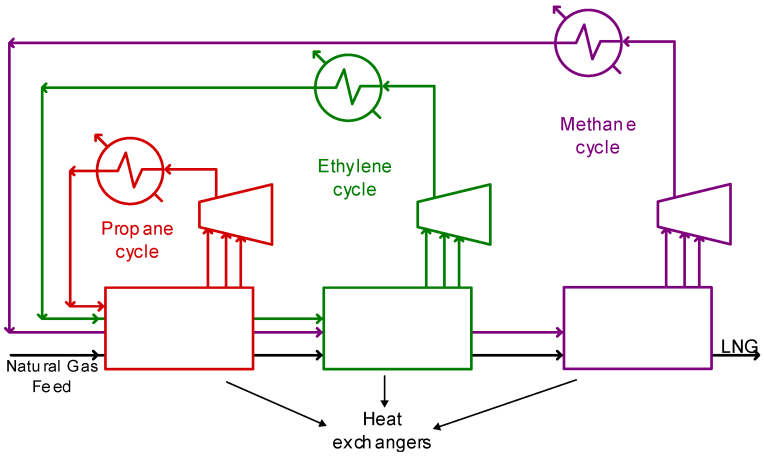

***Figure 4**. Classic cascade process, as described in [47].*

This system has evolved in the last decades, in the direction of a major efficiency and a minor specific energy consumption. To this aim, different levels of pressures have been introduced for each cycle, as shown in **Figure 5**, where the Phillips' Optimized Process (POC) is represented [47], [50]. In this case, the vapours coming from the storage tanks and the loading processes can be reused for the aim of the liquefaction, thus making the process more efficient [51]. The compressors are driven by turbines, which, in the latest versions of the POC process are highly efficient aero-derivative turbines [52].

The POC process has then been further improved by introducing a methane open cycle, allowing for more flexibility of the plant and clearly an improved efficiency [53]. Despite the base plant for the methane open cycle POC process (see **Figure 6**) is more efficient then the basic POC, a further improvement has been achieved, by inserting expanders in place of Joule Thompson valves. This implies an energy recovery by means of the expanders, which are able to produce electric energy and thus reduce the energetic impact of the entire process itself, since the cost per processed natural gas mass unit becomes much lower, the production

of Liquid Natural Gas (LNG) is enhanced and the CO_2 emissions are dramatically reduced [53].

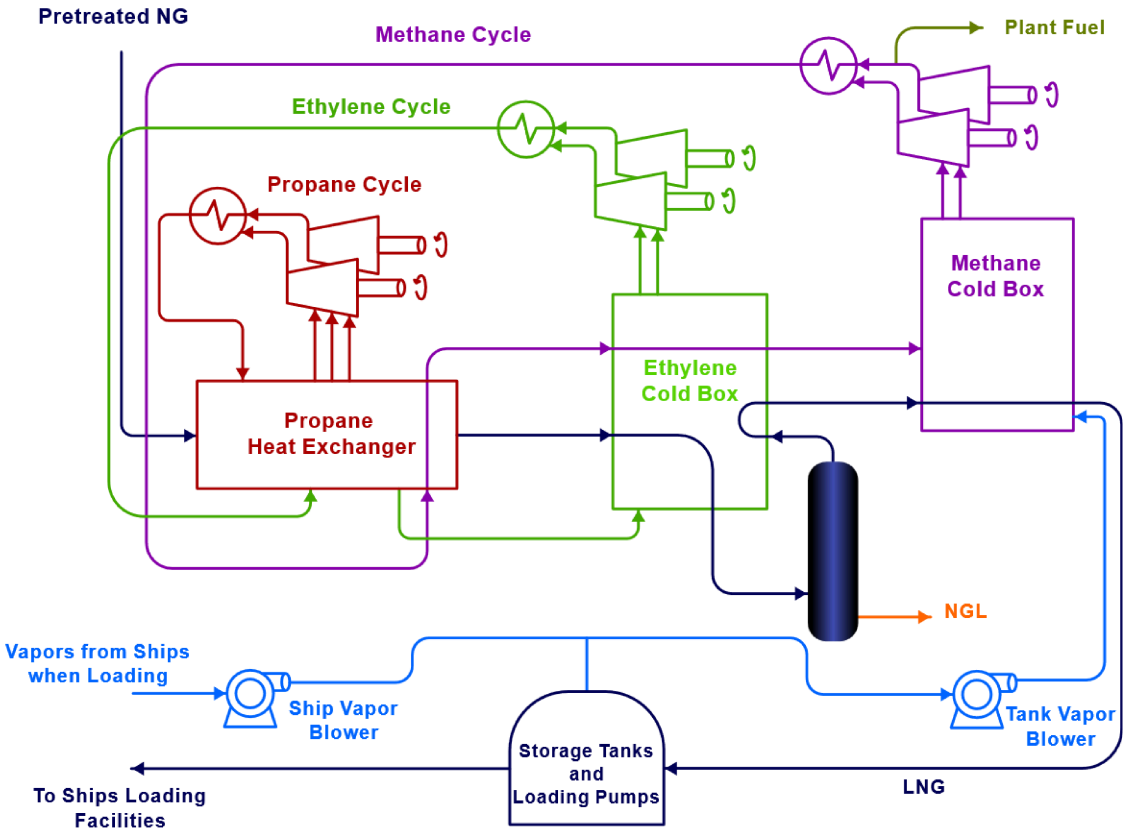

***Figure 5**. Phillips' Optimised Cascade Process.*

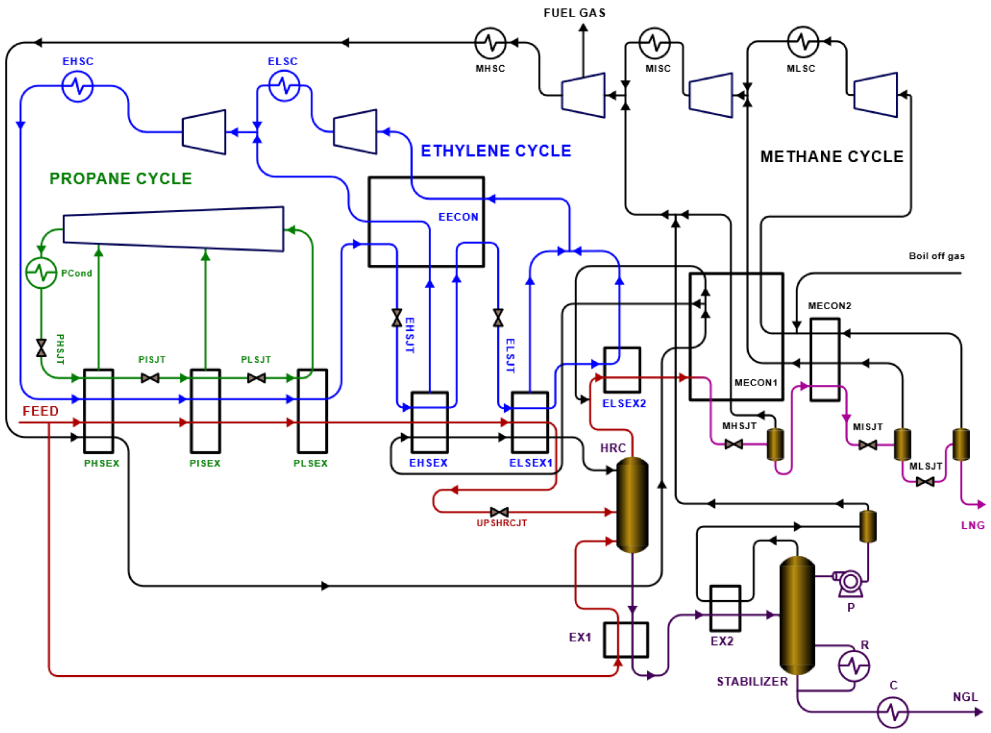

***Figure 6.** Open cycle POC process.*

2.1.2. SMR Processes

Despite extremely efficient, the cascade processes require notably high investment costs for the plant and the maintenance. For this reason, SMR processes were tested: in this case, the cooling cycle is unique, but the refrigerant is a mixture of several chemical species, thus providing an intermediate performance compared to the pure components of the mixture alone. Notably, the efficiency of the SMR plants is slightly inferior compared to the cascade plants but the initial costs for plant are much lower. On the other hand, a higher consumed power is required, due to the greater flows to be processed by the plant.

A noteworthy example is the plant presented by Technip/Air [54], where a two different MR are used. With reference to **Figure 7**, the pre-cooling cycle is performed with a mixture of methane and propane (blue line): the mixed refrigerant is compressed and chilled in a multi-stage compression; subsequently, it is cooled down by using the same refrigerant being throttled. The pre-cooling refrigerant, after being cooled down, is responsible for the liquefaction of a second mixed refrigerant, which is a mixture of ethane and propane (orange line), possessing a higher critical temperature. After being liquified, the second refrigerant is capable of withdrawing heat from the natural gas feed, thus bringing it to liquid state.

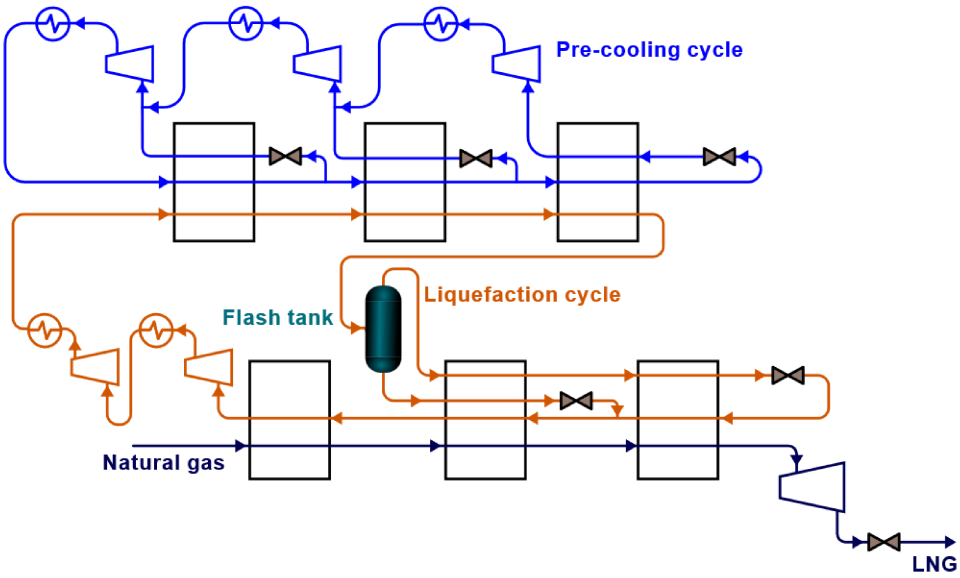

***Figure** 7. SMR process presented by Technip/Air.*

Another process, used mainly for small-scale and offshore plants, is the Poly Refrigerant Integrated Cycle Operation (PRICO) process, which is proprietary by the Black and Veatch company. This has been used for the first time in 1955 for an LNG plant. Its ease of implementation makes it a largely used process, using a blend of nitrogen and hydrocarbons (like methane, ethane, propane, and isopentane) in one closed refrigeration loop to cool and condense the gas. Its simplicity, compactness, low cost, and flexibility make it ideal for base load LNG, peak shaving, and vehicle fuel applications, offering rapid startup/shutdown and reduced personnel needs compared to other methods. Based on [47], [55], [56], **Figure 8** shows the working principles of a PRICO process. The refrigerant (green line) is compressed and chilled. After the chilling, a part of the refrigerant has been liquified: after a phase separation, the refrigerant is throttled and enters the main heat exchanger for the first time. By throttling the stream again, after it exits the heat exchanger for the first time, a temperature gradient is created, in order to subtract heat from the refrigerant itself as well as

from the natural gas, which exits the main heat exchanger in liquid form, and after a passage in a Joule-Thompson valve, the LNG is finally stored.

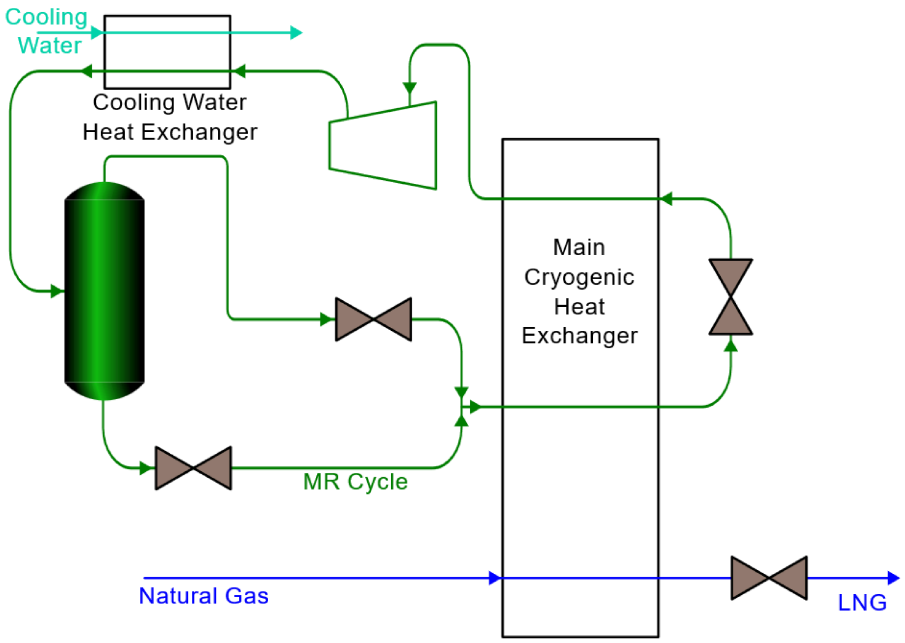

***Figure 8**. Working principles of a PRICO process.*

A third SMR process is the propane precooled mixed refrigerant (C3MR), shown in **Figure 9**. In this case, a precooling with pure Propane (C_3H_8) is performed, thus bringing the natural gas roughly to -40°C, by using three or more pressure levels. Afterwards, a mixed refrigerant, composed by nitrogen, methane, ethane, propane and in some cases butane, is used in a second heat exchanger, for the final heat withdrawal, in order to obtain the LNG, delivered at temperatures ranging between -150 °C and -162 °C. After the precooling cycle, the processed refrigerant is separated in a high-pressure separator. The liquid and vapor mixed-refrigerant (MR) streams then follow distinct paths through the main cryogenic heat exchanger (MCHE). The liquid MR stream contributes to cooling in the warm section of the MCHE, which lowers the temperature of the natural gas. It is expanded across a Joule–Thomson (J–T) valve on the shell side, evaporates, and flows downward to provide cooling for the lower bundle. Meanwhile, the vapor MR stream is responsible for liquefying and subcooling the natural gas to −162 °C in the cold section. This stream also passes through a J–T valve and then flows downward to cool the cold bundle. Afterward, the vapor and liquid MR streams are combined to partially cool the lower bundle.

The fully vaporized MR is compressed to 45–48 bar, then cooled and partially liquefied—first by ambient air and cooling water, and subsequently by propane in the precooling cycle. Precooling occurs in a kettle-type heat exchanger, and the MR cycle employs a coil-wound heat exchanger (CWHE) as the MCHE. Propane compression is handled by a centrifugal compressor. Historically, MR compression relied solely on centrifugal compressors driven by steam turbines. Modern plants, however, use axial compressors for the low-pressure stage and centrifugal compressors for the high-pressure stage, both powered by gas turbines. [47], [57].

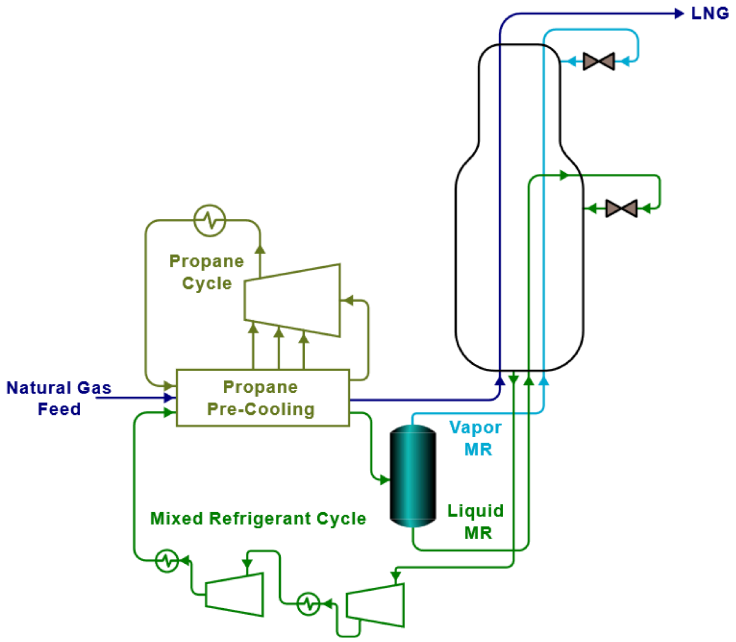

Figure 9. *Scheme representing a C3MR process.*

Shell and APCI introduced the Dual Mixed Refrigerant (DMR) process to address the limitations imposed by compressor size when using pure propane in the C3MR process. As illustrated in **Figure 10**, this configuration closely resembles the C3MR process, featuring two distinct cycles: precooling and liquefaction. In the precooling cycle, a mixed refrigerant—primarily composed of ethane and propane—replaces pure propane, offering greater design flexibility while retaining the same compressor arrangement. During this stage, natural gas is cooled to approximately −50 °C. It is then liquefied and subcooled to around −153 °C in the liquefaction cycle using a mixture of nitrogen, methane, ethane, and propane. The final LNG product is obtained at its atmospheric boiling point of about −161 °C through a liquid expander and an end-flash vessel.

A key feature of the DMR process is the use of two mixed-refrigerant cycles for liquefaction arranged in parallel. This configuration reduces pressure drop, enhances system reliability, and improves overall process efficiency [47], [58].

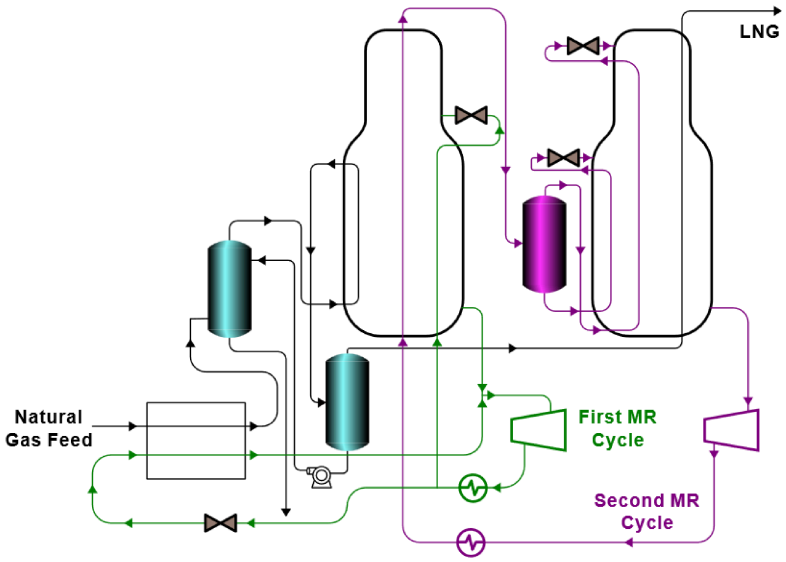

Figure 10. *Scheme representing the DMR process.*

The AP-X process (see **Figure 11**), developed by APCI is an evolution of the C3MR process as it incorporates three distinct cycles: a propane precooling cycle, a mixed refrigerant cycle, and a nitrogen subcooling cycle. A key innovation of this process is the use of a nitrogen expander cycle for LNG subcooling, replacing the traditional mixed refrigerant approach. In the initial stage, natural gas is precooled to approximately −30 °C using kettle-type heat exchangers in the propane cycle. It is then cooled and liquefied to around −120 °C within the main cryogenic heat exchanger (MCHE) using a mixed refrigerant. Subcooling is achieved through cold gaseous nitrogen supplied by the nitrogen expander. Within the nitrogen cycle, nitrogen is compressed to high pressure and cooled to near ambient temperature. The high-pressure nitrogen passes through a plate-fin heat exchanger (PFHE) economizer, where it exchanges heat with low-pressure nitrogen returning to the compressor. Subsequently, the high-pressure nitrogen is expanded to low pressure in an expander, further reducing its temperature. Compared to the C3MR process, the nitrogen expander subcooling cycle enables a reduction in both propane and mixed refrigerant flow without compromising production, allowing for significantly higher capacities—up to approximately 8 MTPA—using existing equipment. Coil-wound heat exchangers (CWHEs) are employed for both the mixed refrigerant and nitrogen subcooling cycles [47], [59].

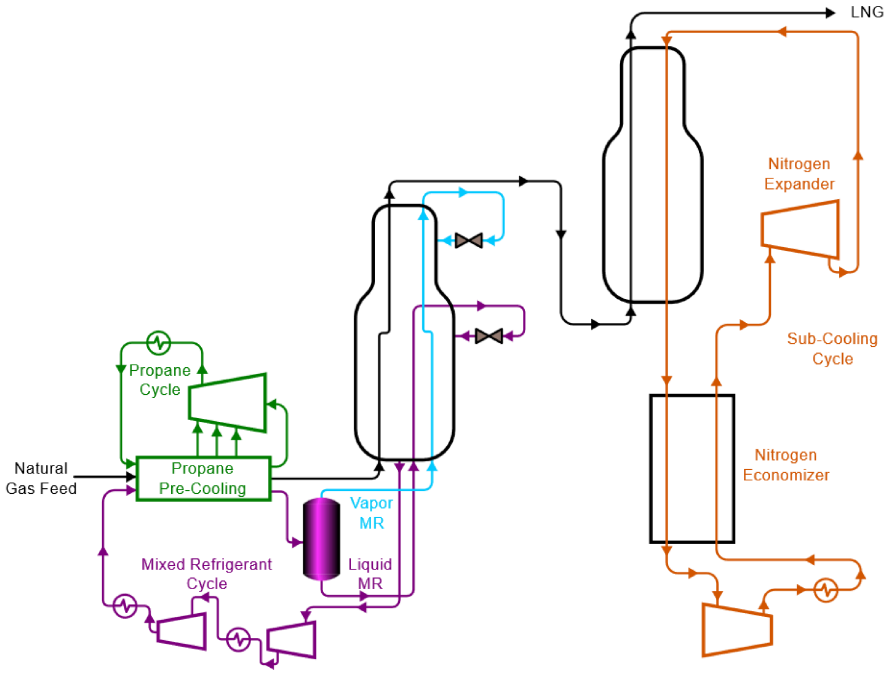

***Figure 11**. Representation of the AP-X process.*

The Mixed Fluid Cascade (MFC) process (see **Figure 12**), developed by Linde in collaboration with Statoil, was implemented in the Snohvit LNG project and enables a single train capacity of approximately 4 MTPA. Similar to the traditional cascade process, the MFC process incorporates three stages: precooling, liquefaction, and subcooling. However, it achieves higher efficiency by using three mixed refrigerants instead of three pure refrigerants. These mixed refrigerants—comprising methane, ethane, propane, and nitrogen—differ in composition across each cycle. Another distinguishing feature is the variation in power requirements among the cycles, unlike the uniform distribution seen in the Phillips Optimized Cascade (POC) process. For heat exchange, the precooling cycle

employs plate-fin heat exchangers (PFHE), while the liquefaction and subcooling cycles utilize coil-wound heat exchangers (CWHE) [47], [60].

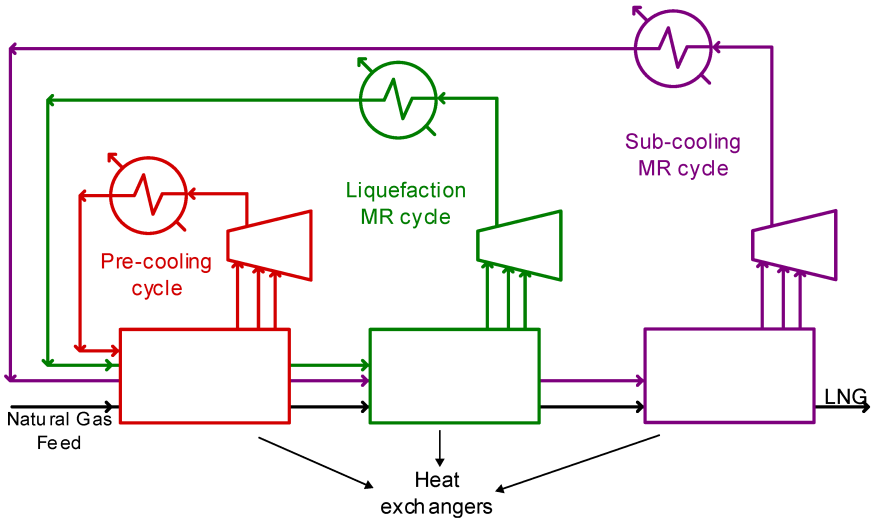

***Figure 12**. Representation of the MFC process.*

2.1.3. Gas expansion processes

Nitrogen expander processes, based on reverse-Brayton and Claude cycles, are primarily employed in offshore and small-scale liquefaction plants. These processes have long been utilized for cryogenic liquefaction applications, including LNG peak-shaving operations and industrial gas liquefiers [61].

A simplified single nitrogen expander cycle is depicted in **Figure 13**. In this process, refrigeration is achieved through compression and work expansion using nitrogen as the refrigerant. High-pressure nitrogen is first cooled in heat exchangers while low-pressure nitrogen returns to the compressor. The high-pressure stream is then expanded in an expander, reducing its temperature and simultaneously generating useful work, typically supplied to a booster compressor. The low-pressure nitrogen exiting the expander provides cooling for liquefying natural gas and for the high-pressure nitrogen in the heat exchangers. Nitrogen circulating through these exchangers is compressed by the main cycle compressor and the booster compressor. Due to the use of a pure gas refrigerant across a wide temperature range, the process efficiency is relatively low. Consequently, the single nitrogen expander cycle is best suited for small-capacity plants [62].

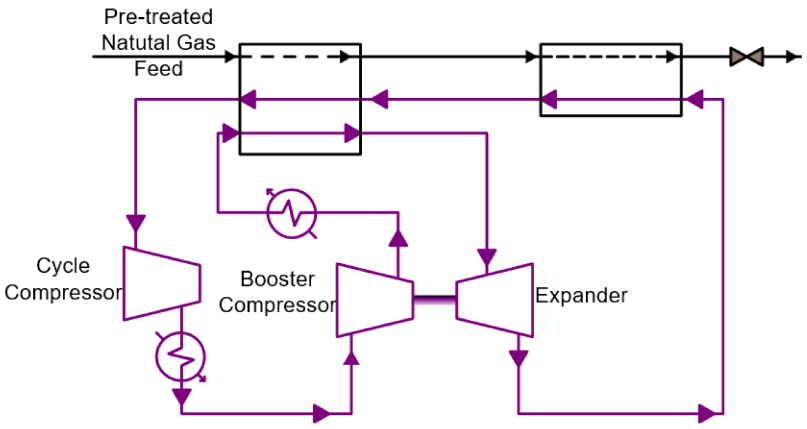

***Figure 13**. Single expander process.*

The double nitrogen expander process is an adaptation of the single nitrogen expander cycle and has been widely employed for liquefying nitrogen and oxygen over the past few decades. This configuration incorporates two expander cycles—warm and cold—as illustrated in **Figure 14**. Both cycles enable natural gas to be liquefied and subcooled at smaller temperature differences, which reduces specific power consumption but requires larger heat exchangers. In this process, nitrogen can be replaced with methane as the refrigerant, potentially lowering the specific power for liquefaction. However, this advantage is offset by the safety concerns associated with using a hydrocarbon refrigerant instead of inert nitrogen [63].

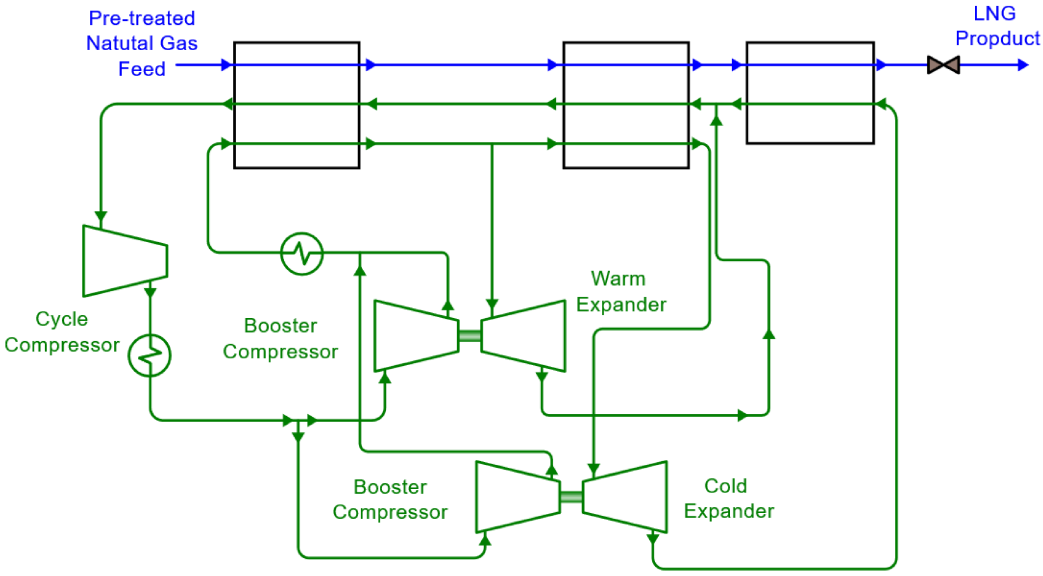

Figure 14. *Double expander process.*

As illustrated in **Figure 15**, the dual independent expander process utilizes two separate refrigeration cycles—methane and nitrogen—to enhance process efficiency by minimizing the temperature difference between liquefaction and subcooling. Although this configuration requires a larger heat exchanger compared to a single expander process, it significantly reduces the specific power requirement. However, the inclusion of methane as a refrigerant introduces safety concerns, as the use of a hydrocarbon increases the risk of jet fires and blast pressure damage. Consequently, additional spacing between equipment is necessary to ensure safe operation [64], [65].

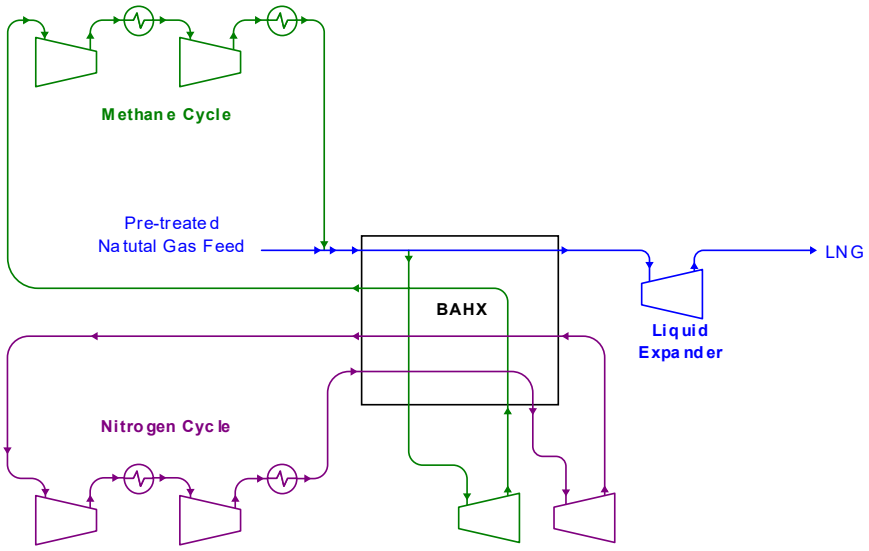

***Figure 15**. Dual independent expander process.*

BHP and Linde developed the compact LNG (cLNG) process, which is similar to the SMR process but uses pure nitrogen as the refrigerant. As shown in **Figure 16**, this process operates with two nitrogen expansion pressure levels to enhance thermodynamic efficiency. To achieve the low temperatures required for natural gas liquefaction, the cLNG process employs both self-cooling and turbo expanders. The power generated by the turbo expander is recovered and utilized for recompressing the refrigerant [47], [66].

Several other expander-based processes have been introduced to improve efficiency. For instance, incorporating propane precooling can reduce power consumption by approximately 20% in conventional expander systems. Various vendors have developed proprietary solutions, including EXP by Kryopak, MiniLNG by Hamworthy, Optimized Expander Cycle by Kanfa Aragon, and LNG Smart Liquefaction Technologies (OCX-Angle, OCX-R, OCX-2, and NDX-1) by Mustang Engineering [67], [68], [69], [70].

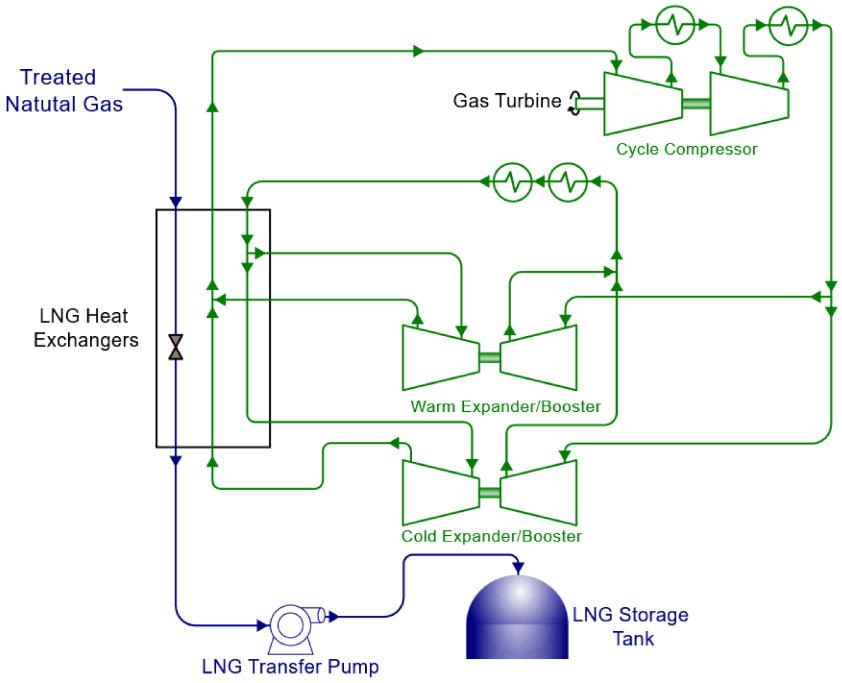

Figure 16. *cLNG process.*

2.2. Green-Powered aviation scenario

The global aviation sector is currently undergoing a structural transformation characterized by the transition from fossil-based kerosene to zero-carbon energy sources, guided by the International Civil Aviation Organization's (ICAO) Long-Term Aspirational Goal (LTAG) of achieving net-zero carbon emissions by 2050 [71], [72]. This state of the art is defined by a "basket of measures" approach, integrating Sustainable Aviation Fuels (SAF), disruptive aircraft technologies, operational improvements, and market-based economic instruments.

2.2.1. Sustainable Aviation Fuels (SAF): Near-Term Scaling and Technological Pathways

SAF is currently the most critical lever for decarbonization, projected to provide approximately 65% of the total emissions reductions required by 2050 [73]. Below the main aspects encompassing the transition.

• Mandates and Policy Frameworks: The regulatory landscape is increasingly shaped by mandatory blending targets, such as the ReFuelEU Aviation regulation in Europe, which requires a minimum SAF share of 2% in 2025, rising to 70% by 2050 [71], [74]. Non-compliance with these mandates carries severe financial penalties, often estimated at 2 to 13 times the cost of the fuel itself [75], [76].

• Technological Pathways: The market is currently dominated by HEFA (Hydroprocessed Esters and Fatty Acids), which utilizes waste oils and fats but faces a "feedstock ceiling" as global supplies are limited. To surpass this limit, the industry is maturing Alcohol-to-Jet (AtJ) and Power-to-Liquid (PtL) pathways; the latter, often called e-SAF, utilizes renewable hydrogen and captured CO_2 to create a virtually unconstrained but energy-intensive fuel source [76].

• Accounting and Integrity: Robust tracking is essential to avoid double-counting; current systems include the IATA SAF Registry (launched in 2025) and the CORSIA Central Registry (CCR), which track environmental attributes independently of physical fuel molecules [77].

• Financial Reality: Despite the potential, financial think tanks like Carbon Tracker highlight that SAF impact remains limited by high price premiums—currently 2 to 5 times the price of conventional jet fuel—and a lack of credible long-term production plans [78].

2.2.2. Disruptive Aircraft Architectures and Propulsion Systems

Technological research has shifted toward disruptive designs targeting an Entry into Service (EIS) by 2035 [74], [79].

• Hybrid-Electric Regional Systems: For the 50–100 seat regional market, projects such as AMBER and HERA are maturing 2MW-class hybrid powertrains that utilize batteries for high-power phases (takeoff/climb) while burning SAF for cruise, aiming for a 30-50% reduction in total fuel burn [80].

• Hydrogen Propulsion: Liquid hydrogen (LH_2) is the leading candidate for zero-carbon flight due to its high specific energy (approx. 120 MJ/kg) compared to kerosene (43 MJ/kg) [36]. However, it requires cryogenic storage at 20.4 K (-253°C) in insulated tanks, which significantly increases fuselage diameter and aerodynamic drag [35], [37], [74].

• Engine Innovation: The RISE (Revolutionary Innovation for Sustainable Engines) and OFELIA programs are validating Open Fan architectures, which remove the engine nacelle to achieve a 20% reduction in fuel burn over 2020-state-of-the-art engines [77], [80].

• Battery-Electric Limitations: Due to current specific energy limits (~2 MJ/kg), purely battery-electric aircraft are deemed suitable only for short-range missions of approximately 200–450 nm [36].

2.2.3. Operational Efficiency and Air Traffic Management (ATM)

Operational improvements offer immediate, scalable CO_2 reductions of 6% to 11% by 2050.

• SESAR and Trajectory-Based Operations (TBO): Europe is transitioning to the Digital European Sky under SESAR 3, replacing rigid airways with dynamic, 4D trajectory-based flight paths [81].

• Vertical and Horizontal Flight Efficiency: Inefficiencies in the vertical trajectory during cruise currently result in excess fuel consumption. Concepts like Free Route Airspace (FRA) allow pilots to fly direct routes, as demonstrated in Nigeria's Kano FIR, saving hundreds of kilograms of fuel per flight [77].

• Ground Operations: Reducing APU (Auxiliary Power Unit) usage and implementing electric taxiing (e.g., TaxiBot) are prioritized to improve local air quality at airports [74], [77].

2.2.4. Non-CO_2 Climate Impacts: Science and Mitigation

Research indicates that non-CO_2 effects—specifically contrail cirrus and nitrogen oxides (NO_x)—may be responsible for two-thirds of aviation's total climate impact.

• Contrail Avoidance: Persistent contrails form in Ice Supersaturated Regions (ISSRs). New operational strategies involve small altitude adjustments to avoid these pancake-shaped regions, which could reduce contrail warming significantly despite a marginal CO2 penalty.

• Aromatics and Soot: The use of aromatic-free fuels (like 100% SAF) has been shown in the ECLIF3 flight trials to reduce soot particle emissions and ice crystal formation by over 25%, drastically thinning contrails.

• Monitoring Frameworks: A new non-CO_2 Monitoring, Reporting, and Verification (MRV) framework will begin in the EU on January 1, 2025, to calculate the CO2-equivalent impact per flight.

2.2.5. Economic Instruments, Financing, and the Path to 2050

The transition requires a multitrillion-dollar investment, estimated at $175 billion per year through 2050.

• Market-Based Measures (MBMs): CORSIA manages international aviation emissions growth, while the EU ETS operates a cap-and-trade system for regional flights; the baseline for CORSIA has been tightened to 85% of 2019 levels to increase stringency [74], [77].

• Climate Financing: ICAO has launched the Finvest Hub to connect clean energy project developers with institutional investors and multilateral development banks.

• Carbon Removals: For residual emissions that cannot be abated by 2050 (estimated at 10%–20% of the baseline), the industry relies on Direct Air Carbon Capture and Storage (DACCS) and other permanent removal technologies [74].

In conclusion, no single solution alone can achieve net-zero aviation; success depends on a synchronized deployment of disruptive airframes, a global scale-up of e-SAF production, and the modernization of global airspace management.

2.2.6. Liquid hydrogen storage strategies and technologies

The implementation of liquid hydrogen (LH_2) storage in commercial aviation represents a radical shift from conventional kerosene-based architectures, necessitating a comprehensive integration of advanced material science, cryogenic thermodynamics, and disruptive airframe design.

2.2.6.1. Thermodynamic and Volumetric Aspects

Hydrogen is characterized by a superior gravimetric energy density of approximately 120 MJ/kg, nearly three times that of kerosene (43 MJ/kg) [35], [37], [77]. However, its volumetric density is extremely low, requiring four times the storage volume of conventional jet fuel to provide equivalent energy [82]. Unlike sustainable aviation fuels (SAF) that suffer from minor energy density limitations, LH_2 must be maintained in a liquid state at cryogenic temperatures of 20.4 K (-253°C) to be viable for mass transport. This requires sophisticated pressure vessels and thermal control systems to mitigate boil-off and handle the fuel's high permeability [80], [82].

2.2.6.2. Material Selection: Metallics vs. Advanced Composites

The design of LH_2 cryotanks is categorized by the selection of metallic alloys or polymeric composites, each presenting distinct advantages in durability and mass efficiency [79], [83].
• **Metallic Solutions**: Aluminum-lithium alloys (e.g., Al 2050, Al 2195) and austenitic stainless steels (e.g., 304L, 316L) are favoured for their mature manufacturability and high damage tolerance [82], [83]. These "Type 1" vessels are resistant to hydrogen embrittlement, a phenomenon where atomic hydrogen reduces a metal's ductility and toughness. Current safety standards identify Al 6061-T6 and 300-series stainless steels as having negligible susceptibility to embrittlement in typical LH_2 environments.
• **Composite Solutions**: Carbon fibre-reinforced plastic (CFRP) tanks offer the potential for a 20-40% reduction in structural weight compared to aluminium [83], [84], [85]. However, standard composites become brittle at 20 K and are prone to microcracking under the thermomechanical cycling required for aviation (typically 10,000 to 60,000 cycles) [83], [84]. To address this, NASA has developed unique ionic liquid (IL) epoxies that maintain toughness and resist delamination at cryogenic temperatures [85]. The Phoebus project is currently validating large-scale linerless CFRP tanks to reduce mass for space and aviation applications [84].

2.2.6.3. Passive and Active Thermal Control Systems

To minimize evaporation, LH_2 tanks utilize a combination of sophisticated insulation technologies [79], [83], [86].
• **Passive Insulation**: The standard state of the art involves double-walled vacuum pressure vessels using Multilayer Insulation (MLI), which consists of reflective metal foils separated by Dacron netting [37], [87]. NASA's Multipurpose Hydrogen Test Bed (MHTB) demonstrated that a variable-density MLI layup could reduce heat leaks by 41% compared to traditional systems [87]. For ground-hold phases, Spray-on Foam Insulation (SOFI) is utilized to prevent air liquefaction on the tank surface [87]. Additionally, Glass Bubble thermal insulation (K1 microspheres) has shown a 40-100% improvement in performance over perlite powder [88], [89].

• **Active Management (ZBO)**: To achieve "Zero Boil-Off" (ZBO), Integrated Refrigeration and Storage (IRAS) systems employ an internal heat exchanger with helium refrigerant to remove energy directly from the LH_2 [89], [90]. This active cooling allows for loss-free storage for indefinite periods [90]. Thermal network models indicate that heat ingress is significantly more sensitive to the warm boundary (ambient) temperature than the cold boundary temperature, emphasizing the importance of managing cold spots at structural supports [88].

2.2.6.4. Airframe Integration and Aerodynamic Trade-offs

The volumetric requirements of LH_2 necessitate a departure from traditional "wing tank" designs toward "dry wing" concepts [36], [90].
• **Fuselage Integration**: Storing LH_2 in tanks positioned fore and aft of the cabin or along the top of the fuselage increases the frontal area and wetted surface, resulting in higher parasitic drag [35], [74].
• **External Mounting**: Suspending tanks under the wings provides inertial relief to the wing structure but introduces substantial aerodynamic penalties [37], [83].
• **Disruptive Designs**: Blended Wing Body (BWB) and clean-sheet architectures are being explored to better accommodate large LH2 volumes without sacrificing the lift-to-drag ratio [74], [79], [91]. Retrofitting existing regional turboprops with hydrogen powertrains is considered a near-term path, while clean-sheet designs targeting 2035 aim for 30-40% efficiency gains.

2.2.6.5. Operational Safety, Certification, and Economic Viability

Transitioning to LH_2 involves complex regulatory and logistical hurdles [79], [92].
• **Safety Infrastructure**: Refuelling hydrogen requires specialized safety clearance zones, currently cited at a 20-meter radius, which significantly impacts airport turnaround times [74], [77]. Systems must include redundant pressure relief devices, hydrogen sensors, and specialized venting systems to prevent detonation [86].
• **Standardization**: International guidelines, including ICAO's LTAG and the KGS Code, are being revised to address the unique risks of liquid hydrogen, such as oxygen enrichment and cryogenic burns [82], [86].
• **Economics**: Hydrogen-powered single-aisle aircraft are projected to have a 21% higher cost per available seat kilometer (CASK) than conventional types, driven by a 31% increase in acquisition costs and a 47% rise in maintenance. Despite these costs, hydrogen is essential for reaching net-zero targets that SAF alone cannot meet [36], [79], [93].
In conclusion, the successful deployment of LH_2 storage depends on the maturation of cryogenic-stable materials, the optimization of active thermal management, and the establishment of a global hydrogen infrastructure at airports.

3. Innovative heat exchangers using the pipe-in-pipe architecture

One of the main challenges with traditional heat exchangers is balancing efficiency and system size: typically, higher efficiency comes at the cost of increased volume. This chapter introduces the pipe-in-pipe architecture, an innovative design that achieves both high efficiency and compactness. Two practical applications are discussed: the first involves implementing a PRICO process for biomethane liquefaction, while the second focuses on vaporizing liquid hydrogen—stored in its cryogenic state—before converting it to gas for use in an aircraft fuel system.

3.1. The pipe-in-pipe architecture

The pipe-in-pipe architecture is an innovative design featuring two coaxial pipes, where the hot fluid flows through the inner pipe and the cold fluid circulates in the annular space between the inner and outer pipes. A turbulence enhancement system is incorporated inside the inner pipe to improve heat transfer. This can be achieved using elements such as twisted tape inserts, dimples, fins, ball turbulators, wire-wrapped cores, or other innovative designs, all aimed at increasing internal turbulence and, consequently, the convective heat transfer coefficient [94]. This heat exchanger configuration offers a simpler alternative to traditional small-scale liquefaction processes, which typically rely on complex multi-flow designs like spiral wound heat exchangers (SWHEs). **Figure 17a** depicts the typical cross-sectional geometry as well as the working principles of the pipe-in-pipe architecture, while **Figure 17b** depicts its longitudinal section.

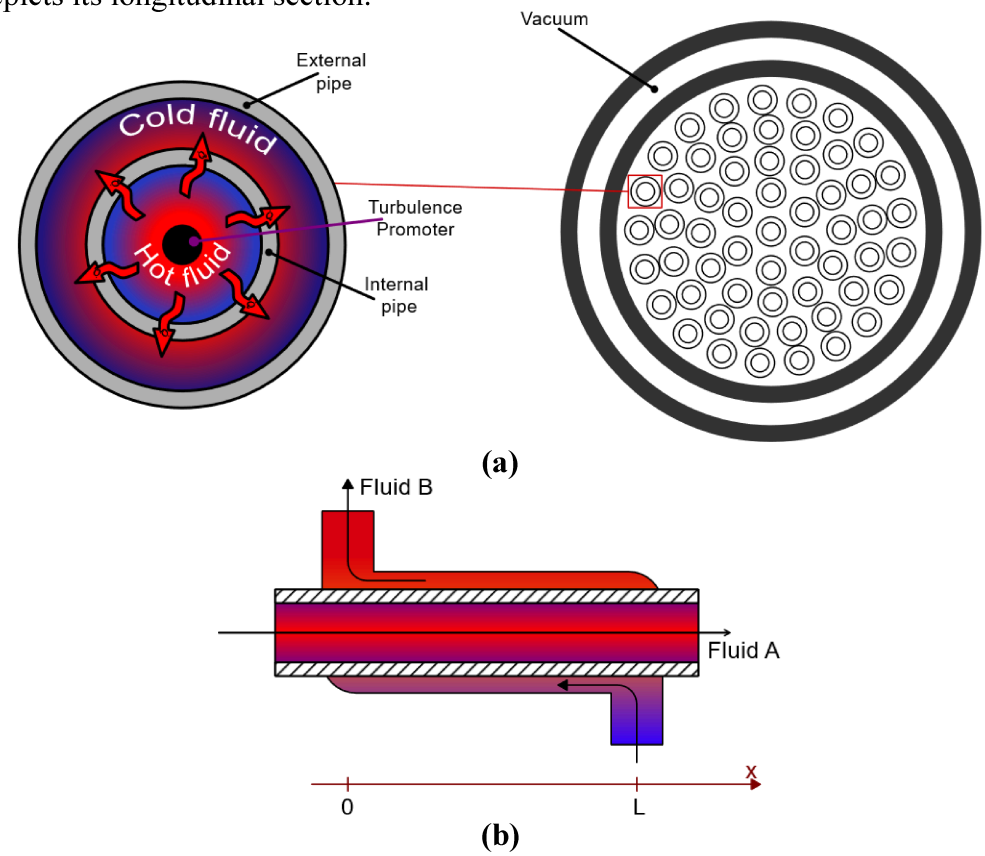

***Figure 17**. Representative scheme of the pipe-in-pipe architecture.*

3.1.1. An innovative PRICO process with the use of the pipe-in-pipe architecture

3.1.1.1 The plant description

This section introduces a novel process along with the corresponding plant design. The innovation lies in combining the pipe-in-pipe architecture with the overall plant layout, as illustrated in **Figure 18**. Conventional SMR systems for small-scale applications often face a major limitation: they depend on intricate multi-stream heat exchangers. In very small biomethane plants, this results in increased complexity and cost, further exacerbated by the proprietary nature of such equipment and the need for advanced process modelling [26], [31].

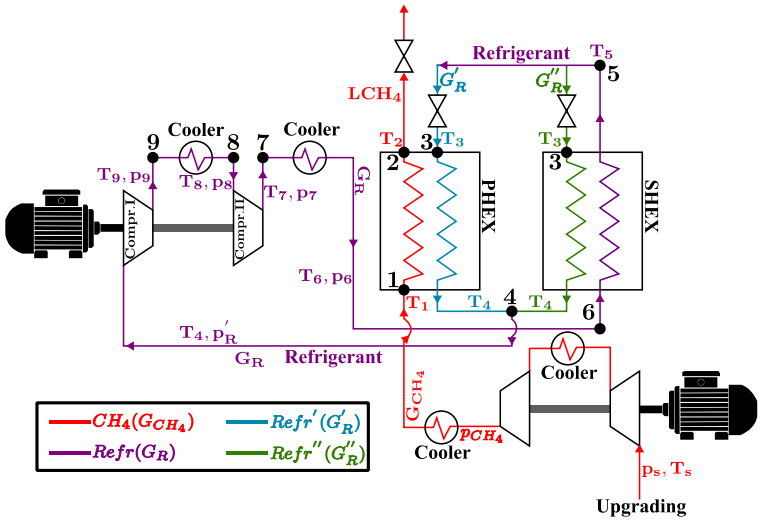

***Figure 18**. Layout of the proposed plant.*

The proposed SMR liquefaction process overcomes these limitations by employing two pipe-in-pipe heat exchangers: the primary heat exchanger (PHEX) and the secondary heat exchanger (SHEX). The plant is in phase of manufacturing at "Sistemi Energetici", in Foggia, Italy. Biomethane from the upgrading plant enters the liquefaction unit as a gas at supply pressure p_s and temperature T_s, with a flow rate G_{CH_4}. It is then compressed in a two-stage intercooled system (or optionally three-stage) and cooled in the final cooler, resulting in compressed biomethane at pressure p_{CH_4} and temperature T_1, ready for the PHEX.

Inside the PHEX, biomethane is liquefied through counterflow heat exchange with a cold refrigerant (Refr′), which is a mixture of nitrogen, methane, ethane and propane with $\chi_{N_2} = 0.1$, $\chi_{CH_4} = 0.34$, $\chi_{C_2H_6} = 0.41$ and $\chi_{C_3H_8} = 0.15$ as the molar fraction, respectively. The aforementioned refrigerant enters at pressure p'_R, temperature T_3, and flow rate G'_R. The liquefied biomethane exits at cryogenic temperature $T_2 (T_2 > T_3)$, while Refr′ leaves as a gas at temperature $T_4 (T_4 < T_1)$.

The SHEX, together with two expansion valves, generates the cold refrigerant stream Refr′ at p'_R and T_3. The full refrigerant flow G_R is first compressed in a two-stage intercooled system (or optionally three-stage), then cooled in the final cooler to T_6. It enters the SHEX at high pressure p_R and low temperature T_6, where it is liquefied and further cooled to T_5 by exchanging heat with a portion of the same refrigerant (Refr″) that has undergone Joule–Thomson expansion through the right-hand valve. The two refrigerant streams, Refr and

Refr″, differ in flow rates (G_R' and $G_R'' = G_R - G_R'$) but share identical pressure and temperature at the heat exchanger outlets, ensuring easy mixing in the next process stage.

3.1.1.2. The governing equations of the process

The thermodynamic model for the proposed process was initially developed and validated in [33], and its governing equations are outlined below. It employs the FluidProp libraries by Asimptote and assumes that the heat exchangers are perfectly insulated from the environment—a reasonable assumption given the use of vacuum-based insulation systems. The model is structured into three key stages:

1. Calculation of temperatures
2. Determination of heat transfer coefficients
3. Assessment of performance parameters

Thermophysical properties of the refrigerant, which is a multicomponent mixture, are computed using the Perturbed-Chain Polar Statistical Associating Fluid Theory (PCP-SAFT) model. Biomethane, considered as pure CH_4, is characterized using the FreeStanMix model.

Encompassing the calculation of the temperatures, it is needed to take into account for the thermal power balance on both the exchangers:

$$G_{CH_4} \cdot (i_1 - i_2) = G_R{}'(i_3 - i_4) = G_R \cdot (i_4 - i_6) \quad (1)$$

$$G_R \cdot (i_6 - i_5) = (G_R - G_R{}') \cdot (i_3 - i_4) \quad (2)$$

where i_1 and i_2 are the biomethane enthalpies at the inlet and outlet of the PHEX; i_3 and i_4 are the enthalpies of $G_R{}'$ at the inlet and outlet of the PHEX, respectively. Similarly, i_6 and i_5 are the enthalpies of G_R at the inlet and outlet of the SHEX, where $i_5 = i_3$ (iso-enthalpic expansion); i_3 and i_4 are also the enthalpies of $G_R{}'' = G_R - G_R{}'$ at the inlet and outlet of the SHEX, respectively. The calculation requires the following input data:

- **For biomethane:** inlet temperature to the primary heat exchanger (PHEX, T_1), outlet temperature from the PHEX (T_2), flow rate (G_{CH_4}), and operating pressure in the PHEX (p_{CH_4}).
- **For the refrigerant:** in the PHEX (*Refr′*) and in the secondary heat exchanger (SHEX, *Refr″*), the required inputs are the outlet temperature (T_4) and operating pressure ($p_{R'}$). The operating conditions of *Refr″* are identical to those of *Refr′* to enable direct mixing.
- **For the total refrigerant stream (Refr)** in the SHEX, the inputs include the inlet temperature (T_6) and operating pressure (p_R).

Using the FluidProp libraries and the governing equations, all enthalpies, temperatures at key points, and flow rates in the heat exchangers can be determined.
The geometry of the heat exchangers—both assumed to be of the pipe-in-pipe type—is also an input. For each unit, this includes: the number of external pipes (n_t, equal to the number of internal pipes), the internal and external diameters of the inner pipes ($d_{i,i}$, $d_{e,i}$), and the

internal diameter of the outer pipes ($d_{i,e}$). For major clarity related to the geometry, see **Figure 19**.

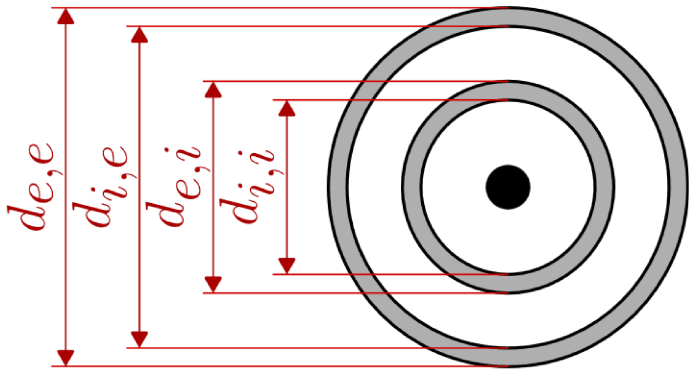

***Figure 19**. Geometric parameters of the pipe-in-pipe architecture.*

In both heat exchangers, the hot fluid flows through the inner pipe, and the cold fluid circulates in the annular space. In the PHEX, biomethane serves as the hot fluid (*H*) and *Refr'* as the cold fluid (*C*). In the SHEX, *Refr* is the hot fluid, while *Refr"* is the cold fluid. The effective heat transfer areas for the hot (A_H) and cold (A_C) streams are then calculated accordingly:

$$A_H = k_{A_H} \cdot \frac{\pi \cdot {d_{i,i}}^2}{4} \tag{3}$$

$$A_C = \frac{\pi \cdot ({d_{i,e}}^2 - {d_{e,i}}^2)}{4} \tag{4}$$

The coefficient k_{A_H}, with a value less than one, accounts for the reduction of the internal pipe's cross-sectional area due to the installation of a turbulence enhancement system. Knowing both the effective heat transfer areas and the geometry of the turbulence enhancer makes it possible to determine the hydraulic diameters for the hot fluid ($d_{h,H}$) and cold fluid ($d_{h,C}$) as follows:

$$d_{h_H} = \frac{4 \cdot A_H}{p_p + \pi \cdot d_{i,i}} \tag{5}$$

$$d_{h_C} = \frac{4 \cdot A_C}{\pi \cdot d_{i,e} + \pi \cdot d_{e,i}} \tag{6}$$

where parameter p_p represents the perimeter of the turbulence enhancer. For calculation purposes, both heat exchangers are divided into *n* modules. Within each module (see **Figure 20**), the cold fluid experiences a temperature change described by:

$$\Delta T_c = \frac{T_4 - T_3}{n} \tag{7}$$

The outlet temperature of the cold fluid in module i ($i = 1, \dots n$) is calculated as follows:

$$(T_{out,C})_i = (T_{in,C})_i + \Delta T_C \tag{8}$$

$$(T_{in,C})_i = (T_{out,C})_{i-1} \tag{9}$$

For both heat exchangers, in the first module ($i = 1$), the cold fluid inlet temperature $(T_{in,C})_1$ equals T_3; in the last module ($i = n$), the cold fluid outlet temperature $(T_{out,C})_n$ equals T_4. Knowing the inlet temperature $(T_{in,C})_i$ and outlet temperature $(T_{out,C})_i$ for each module allows calculation of the refrigerant's inlet enthalpy $(i_{in,C})_i$ and outlet enthalpy $(i_{out,C})_i$ using the FluidProp libraries. The thermal power exchanged in each module is then computed as follows:

$$(\dot{Q}_{exc})_i = G_C \cdot [(i_{out,C})_i - (i_{in,C})_i] \tag{10}$$

where G_C=G_R' for the PHEX and G_C=G_R'' for the SHEX. The calculation of $(\dot{Q}_{exc})_i$ allows the enthalpy of the hot fluid to be calculated at the inlet of each module, as follows:

$$(i_{in,H})_i = (i_{out,H})_i + \frac{(\dot{Q}_{exc})_i}{G_H} \tag{11}$$

$$(i_{out,H})_i = (i_{in,H})_{i-1} \tag{12}$$

where $G_H = G_{CH_4}$ for the PHEX and G_H=G_R for the SHEX. In the first module ($i = 1$), $(i_{out,H})_1$=i_2 for the PHEX and $(i_{out,H})_1$=i_5 for the SHEX. Once the outlet and inlet enthalpies of the hot fluid, $(i_{out,H})_i$ and $(i_{in,H})_i$, have been determined for each module, the corresponding temperatures $(T_{out,H})_i$ and $(T_{in,H})_i$ can be computed using the FluidProp libraries, based on pressure and enthalpy values.

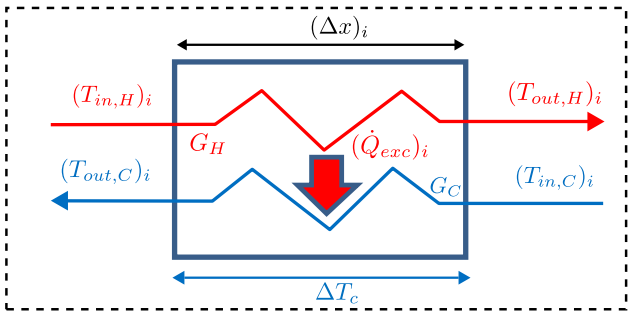

Figure 20. *Schematic of a single submodule.*

Regarding the heat transfer coefficients, once the temperatures of both fluids have been determined in each module—specifically, the cold fluid inlet and outlet temperatures ($(T_{in,c})_i$, $(T_{out,c})_i$) and the hot fluid inlet and outlet temperatures ($(T_{in,H})_i$, $(T_{out,H})_i$)—the heat transfer coefficients can then be calculated. The pressure of biomethane exceeds its critical value, while that of "Refr" is near the critical point. As a result, the convective heat transfer coefficient for both fluids can be evaluated using average thermophysical properties. In contrast, the pressures of Refr′ and Refr″ are significantly below their respective critical pressures, leading to pronounced differences between the vapor and liquid phases. For Refr′ and Refr″, a specialized method is necessary to calculate the convective heat transfer within the two-phase region (vapor quality 0<q<1). However, when q=0 (pure liquid) or q=1 (pure

vapor), the same procedure used for biomethane and Refr can be applied to Refr′ and Refr″; this method is described below. In each module of the heat exchanger, the average temperatures of the cold and hot fluids are calculated as:

$$(\overline{T_H})_i = \frac{(T_{in,H})_i + (T_{out,H})_i}{2};\ (\overline{T_C})_i = \frac{(T_{in,C})_i + (T_{out,C})_i}{2} \tag{13}$$

Using the FluidProp libraries, the average temperatures in each module enable the calculation of the following properties for both hot and cold fluids in every module:

- average densities $\bar{\rho}_{H,i}$ and $\bar{\rho}_{C,i}$
- average thermal conductivities $\bar{\lambda}_{H,i}$ and $\bar{\lambda}_{C,i}$,
- average viscosities $\bar{\mu}_{H,i}$ and $\bar{\mu}_{C,i}$,
- average specific heats $\overline{C_{pH,i}}$ and $\overline{C_{pC,i}}$.

The average velocities of the hot and cold fluids in each module can then be calculated as:

$$(\bar{V}_x)_i = \frac{G_x}{n_t \cdot (\overline{\rho_x})_i \cdot A_x} \tag{14}$$

where either $x=H$ (hot fluid) or $x=C$ (cold fluid). Subsequently, the average Reynolds numbers for the hot and cold fluids are determined in each module according to the following expressions:

$$(\overline{Re_x})_i = \frac{(\bar{V}_x)_i \cdot (\overline{\rho_x})_i \cdot d_{h,x}}{(\overline{\mu_x})_i} \tag{15}$$

The use of average fluid properties also enables the calculation of the Prandtl numbers for both the cold and hot fluids in each module:

$$(\overline{Pr_x})_i = \frac{(\overline{\mu_x})_i \cdot (\overline{cp_x})_i}{(\overline{\lambda_x})_i} \tag{16}$$

The average Nusselt number for each module $(\overline{Nu_x})_i$ depends on the Reynolds Number. In the case of laminar flow with a constant rate of heat transfer:

$$(\overline{Nu_x})_i = 4.36 \ \ if\ (\overline{Re_x})_i < 2300. \tag{17}$$

The Gnielinski correlation is considered the most reliable formulation for characterizing transitional and turbulent flow regimes:

$$(\overline{Nu_x})_i = \frac{\frac{\xi}{8} \cdot ((\overline{Re_x})_i - 1000) \cdot (\overline{Pr_x})_i)}{1 + 12.7\left(\frac{\xi}{8}\right)^{0.5} \cdot \left((\overline{Pr_x})_i^{\frac{2}{3}} - 1\right)};\quad where\ (\xi)_i = (1.82 \cdot log(\overline{Re_x})_i - 1.64)^{-2} \\ if\ 2300 < (\overline{Re_x})_i < 10^6 \tag{18}$$

where the symbol $(\xi)_i$ represents the friction factor in the case of smooth tubes, in each module from the Filonienko relationship. For extremely elevated Reynolds numbers, the Chilton-Colburn expression is used:

$$(\overline{Nu_x})_i = 0.023 \cdot (\overline{Re_x})_i^{0.8} \cdot (\overline{Pr_x})_i^{1/3} \quad if\ (\overline{Re_x})_i > 10^6 \tag{19}$$

These equations, extensively validated in the literature [95] [96], are considered reliable for fully developed hydrodynamic and thermal flow conditions. The convective heat transfer coefficients for both the hot and cold fluids are then calculated as follows [96]:

$$\left(\overline{h_H}\right)_i = k_{h,H} \cdot \frac{(\overline{Nu_H})_i \cdot (\overline{\lambda_H})_i}{d_{h,H}};\ \left(\overline{h_C}\right)_i = \frac{(\overline{Nu_C})_i \cdot (\overline{\lambda_C})_i}{d_{h,C}} \tag{20}$$

The factor $k_{h,H}$ accounts for the turbulence enhancement induced by the internal turbulence enhancer. The convective heat transfer calculations described above are considered accurate for single-phase fluids and for two-phase fluids near critical conditions. Consequently, these methods are applied to methane (CH_4) and the refrigerant (Refr). They are also used for the cold refrigerant streams Refr' and Refr'' and when the vapor quality q=0 (pure liquid) or q=1 (pure vapor). However, for vapor quality values 0<q<1, an alternative approach is necessary for Refr' and Refr'', as their pressures are well below the critical pressure. Here, the subscript C refers to the cold fluid (both Refr' and Refr'' are cold fluids).
For each module of the heat exchanger, the thermophysical properties of the vapor and liquid phases are calculated using the FluidProp libraries. These properties include:

- vapor viscosity $\left(\overline{\mu_{C,v}}\right)_i$ and liquid viscosity $\left(\overline{\mu_{C,l}}\right)_i$,
- vapor specific heat $\left(\overline{Cp_{C,v}}\right)_i$ and liquid specific heat $\left(\overline{Cp_{C,l}}\right)_i$,
- vapor density $\left(\overline{\rho_{C,v}}\right)_i$ and liquid density $\left(\overline{\rho_{C,l}}\right)_i$,
- vapor thermal conductivity $\left(\overline{\lambda_{C,v}}\right)_i$ and liquid thermal conductivity $\left(\overline{\lambda_{C,l}}\right)_i$.

Among the various correlations available in the literature, Chen's correlation is recognized as one of the most effective for calculating convective heat transfer coefficients in two-phase flows. Using this method, the convective heat transfer coefficient $\left(\overline{h_c}\right)_i$ is expressed as the sum of two components [97]:

$$\left(\overline{h_C}\right)_i = \left(\overline{h_{NC}}\right)_i + \left(\overline{h_{lf}}\right)_i \tag{21}$$

where $\left(\overline{h_{NC}}\right)_i$ represents the contribution from nucleate boiling, which typically increases with the temperature difference between the wall and the saturation temperature. In this study, this term is neglected due to the minimal temperature difference observed. The term $\left(\overline{h_{lf}}\right)_i$ corresponds to the convective heat transfer between the wall and the liquid film, calculated as follows [97]:

$$\left(\overline{h_{lf}}\right)_i = 0.023 \cdot \left(\overline{Re_{lf}}\right)_i^{0.8} \cdot (\overline{Pr_{lf}})_i^{0.4} \cdot \frac{(\overline{\lambda_{C,l}})_i}{d_{h_C}} \cdot F \tag{22}$$

where $(\overline{\mathrm{Re_{lf}}})_i$ and $(\overline{\mathrm{Pr_{lf}}})_i$ are the Reynolds number and Prandtl number of the liquid film, calculated as:

$$\left(\overline{Re_{lf}}\right)_i = \ (1-q)\cdot\frac{G_C\cdot d_{h_C}}{n_t\cdot A_C\cdot(\overline{\mu_{C,l}})_i} \tag{23}$$

$$(\overline{Pr_{lf}})_i = \ \frac{(\overline{\mu_{C,l}})_i\cdot(\overline{cp_{C,l}})_i}{(\overline{\lambda_{C,l}})_i} \tag{24}$$

The Reynolds number factor F is a function of the Martinelli parameter $(\overline{x_{tt}})_i$:

$$F = 3\cdot\left(\frac{1}{(\overline{x_{tt}})_i}\right)^{0.684} \quad if\ (\overline{x_{tt}})_i < 5 \tag{25}$$

$$F = 1 \quad if\ (\overline{x_{tt}})_i \geq 5 \tag{26}$$

where the Martinelli parameter is given by [97]:

$$(\overline{x_{tt}})_i = \left(\frac{1-q}{q}\right)^{0.9}\cdot\left(\frac{\left(\overline{\rho_{C,v}}\right)_i}{\left(\overline{\rho_{C,l}}\right)_i}\right)^{0.5}\cdot\left(\frac{\left(\overline{\mu_{C,l}}\right)_i}{\left(\overline{\mu_{C,v}}\right)_i}\right)^{0.1} \tag{27}$$

Regarding the performance parameters calculation, the mean heat transfer coefficient U_i in module i is calculated as [96]:

$$U_i = \frac{1}{\frac{1}{\left(\overline{h_C}\right)_i} + \frac{1}{\left(\overline{h_H}\right)_i}\cdot\frac{d_{i,i}}{d_{e,i}}} \tag{28}$$

Knowing the values of $(\dot{Q}_{exc})_i$ and U_i in each module enables the calculation of the required heat exchange length for that module:

$$\Delta x_i = \frac{(\dot{Q}_{exc})_i}{\pi\cdot d_{e,i}\cdot n_t\cdot U_i\cdot(\overline{\Delta T})_i} \tag{29}$$

where $(\overline{\Delta T})_i$ is the logarithmic mean temperature difference:

$$(\overline{\Delta T})_i \ = \ \frac{[(T_{in,H})_i - (T_{out,C})_i] - [(T_{out,H})_i - (T_{in,C})_i]}{ln\left(\frac{(T_{in,H})_i - (T_{out,C})_i}{(T_{out,H})_i - (T_{in,C})_i}\right)} \tag{30}$$

where $(T_{in,H})_i - (T_{out,C})_i$ and $(T_{out,H})_i - (T_{in,C})_i$ can be represented as ΔT_1 and ΔT_2, respectively. The overall length of the heat exchanger is given by:

$$L_y = \sum_{i=1}^{n}\Delta x_i \tag{31}$$

where either *y=PHEX* or *y=SHEX.* The pressure drops for both the hot and cold fluids is calculated using the Darcy formula, based on the average fluid properties, as follows:

$$\Delta p = \sum_{i=1}^{n} \frac{1}{2} \cdot k_{\Delta p_H} \cdot (f_H)_i \cdot \left(\overline{V_H}\right)_i^{\,2} \cdot \left(\overline{\rho_H}\right)_i \cdot \frac{\Delta x_i}{d_{h,H}} \tag{32}$$

$$\Delta p_C = \sum_{i=1}^{n} \frac{1}{2} \cdot (f_C)_i \cdot \left(\overline{V_C}\right)_i^{\,2} \cdot \left(\overline{\rho_C}\right)_i \cdot \frac{\Delta x_i}{d_{h,C}} \tag{33}$$

where $k_{\Delta p_H}$ is greater than 1 and accounts for the additional pressure drop caused by the turbulence enhancer system. The friction factors f_H and f_C for the hot and cold fluids, respectively, are calculated for rough tubes using the Haaland formula when the flow is turbulent, as detailed in [96]:

$$(f_x)_i = \frac{64}{\left(\overline{Re_x}\right)_i} \quad \text{if } \left(\overline{Re_x}\right)_i < 2300 \tag{34}$$

$$(f_x)_i = \frac{1}{\left(-1.8 \cdot log\left(\frac{\varepsilon}{d_{h,x}{}^{3,7}}\right)^{1.11} + \frac{6.9}{\left(\overline{Re_x}\right)_i}\right))^2} \text{ if } \left(\overline{Re_x}\right)_i \geq 2300 \tag{35}$$

where Ɛ is the roughness of the tubes.

The coefficient of performance (COP) of the entire system is calculated as follows. The compressors' isothermal work is determined assuming ideal gas behaviour. Accordingly, the power required to compress the refrigerant and the biomethane are, respectively:

$$P_{compr,R} = G_R \cdot \left(\frac{R_R \cdot {T_R}^I \cdot ln{\beta_R}^I}{{\eta_R}^I} + \frac{R_R \cdot {T_R}^{II} \cdot ln{\beta_R}^{II}}{{\eta_R}^{II}} \right) \tag{36}$$

$$P_{compr,CH_4} = G_{CH_4} \cdot \left(\frac{R_{CH_4} \cdot {T_{CH_4}}^I \cdot ln{\beta_{CH_4}}^I}{{\eta_{CH_4}}^I} + \frac{R_{CH_4} \cdot {T_{CH_4}}^{II} \cdot ln{\beta_{CH_4}}^{II}}{{\eta_{CH_4}}^{II}} \right) \tag{37}$$

where R is the elastic constant; T^I and T^{II} represent the inlet temperatures for the first and second compression stages, respectively, with $T_R^I = T_4$ and $T_R^{II} = T_8$. The compression ratios for the first and second stages are denoted by β^I and β^{II}. The overall efficiencies for the first and second stages, η^I and η^{II}, are defined as $\eta = \eta_{isth} \cdot \eta_m \cdot \eta_v$, where η_{isth} is the isothermal efficiency, η_m the mechanical efficiency, and η_v the volumetric efficiency.

Assuming the refrigerant capacity of the final coolers is provided by chillers with coefficient of performance COP_{chil}, the electric power consumed by the chillers is calculated as follows:

$$P_{chil,R} = \frac{G_R \cdot ({i_{ex,R}}^{II} - i_6)}{COP_{chil,R}} \tag{38}$$

$$P_{chil,CH_4} = \frac{G_{CH_4} \cdot ({i_{ex,CH_4}}^{II} - i_1)}{COP_{chil,CH_4}} \tag{39}$$

where ${i_{ex}}^{II}$ is the enthalpy at the outlet of the second compressor (with ${i_{ex,R}}^{II} = i_7$), calculated by applying the first law of thermodynamics and considering the internal work performed. For cooling in the intercoolers of both biomethane and refrigerant streams, chilled water may be employed; nonetheless, the energy consumed by the associated water circulation pumps is disregarded in this study, given its negligible contribution to the overall power demand.

Two coefficients of performance are evaluated in this analysis. The first coefficient is determined by omitting the power requirements of the biomethane compressors and chillers, which facilitates a fair comparison with natural gas liquefaction processes that receive the feed gas already under compression:

$$COP_1 = \frac{G_{CH_4}(i_1 - i_2)}{P_{compr,R} + P_{chil,R}} \tag{40}$$

The second coefficient of performance accounts for the power consumption of the biomethane compressors and the associated chiller as well:

$$COP_2 = \frac{G_{CH_4}(i_1 - i_2)}{P_{compr,R} + P_{chil,R} + P_{compr,CH_4} + P_{chil,CH_4}} \tag{41}$$

Both COP_1 and COP_2 serve as key metrics to assess the performance of the proposed plant, alongside the specific energy consumption, which is quantified using the following parameters:

$$E_{n,1} = \frac{P_{compr,R} + P_{chil,R}}{G_{CH_4}} \tag{42}$$

$$E_{n,2} = \frac{P_{compr,R} + P_{chil,R} + P_{compr,CH_4} + P_{chil,CH_4}}{G_{CH_4}} \tag{43}$$

The value of $E_{n,2}$ includes the power consumed by the biomethane compressors and chiller, providing a more accurate estimate of the energy consumption. In contrast, $E_{n,1}$ is useful for comparison with liquefaction processes reported in the literature that do not account for the power required for biomethane compression and precooling. For the sake of clarity **Figure 21** and **Figure 22** depict the interaction between the input variables, the input parameters and the intermediate variables, in order to obtain the desired outputs.

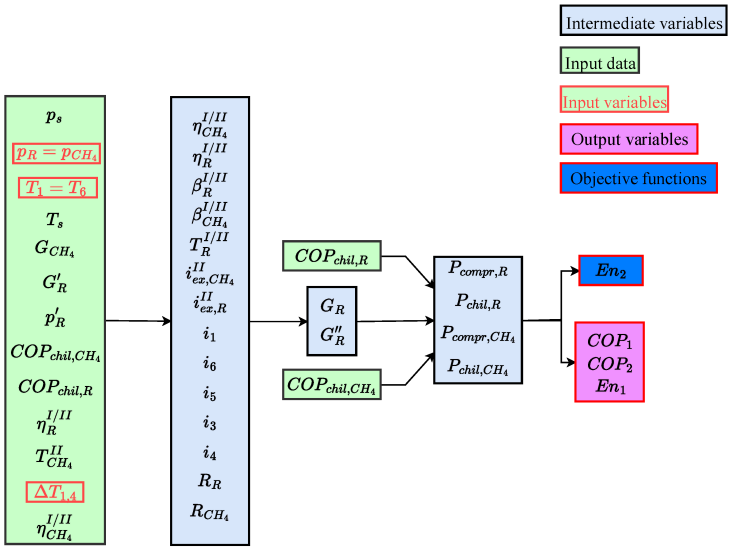

Figure 21. *Flowchart for the calculation of the specific energy consumption* E_{n2}.

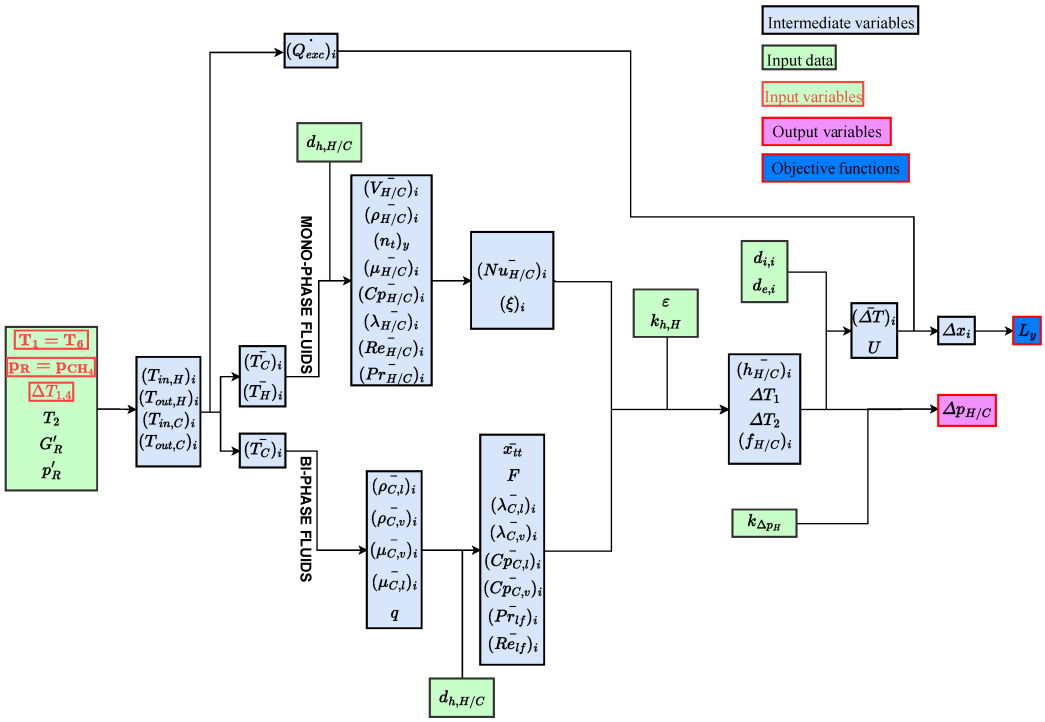

Figure 22. *Flowchart for the calculation of the total length of the pipes* L_{tot}.

3.1.1.2. Results

Two complementary studies were carried out by the author [40], [98]. The first study explored how variations in thermodynamic input parameters can affect the plant's performance through a domain analysis. The second study applied an optimization algorithm to achieve an improved balance between energy efficiency and system compactness. This section will first present the variables and parameters that remained constant, followed by the detailed results of each study.

In the calculation, the PHEX is divided into 40 modules, whilst the SHEX into 30 modules. An important consideration is that throughout all calculations, the molar fractions of the components of the refrigerant mixture are assumed to remain constant. Specifically, the fractions are set as follows: $\chi_{N_2} = 0.1$, $\chi_{CH_4} = 0.34$, $\chi_{C_2H_6} = 0.41$, $\chi_{C_3H_8} = 0.15$. These values were determined through a trial-and-error approach, as documented in [99].

Possible data for these applications (i.e., for small scale biomethane plants) are used in this optimization process. The input thermodynamic and operating parameters, including temperatures and flow rates, designated for optimizing the proposed biomethane liquefaction plant are delineated as follows:

- The gaseous biomethane supply temperature is set at $T_s = 30$ [°C] with a pressure p_s=1.5 [bar], consistent with values present in the literature [99];
- The temperature assumed by the gaseous biomethane upon entering the liquefaction plant is equivalent to the supply temperature provided by the upgrading plant, $T_{CH_4}^{I}=T_s=30$ [°C] [99];
- The temperature assumed by the gaseous biomethane after the first intercooled compression stage, is considered equal to $T_{CH_4}^{II} = 25$ [°C] [99];
- The compressor efficiencies for both biomethane and refrigerant remain consistent across the first and second stages, with values set to $\eta_{CH_4}^{I}=\eta_{CH_4}^{II}=\eta_R^{I}=\eta_R^{II}=0.82$ [99];
- The performance coefficients for both biomethane and refrigerant in the chiller (COP_{chil,CH_4} and $COP_{chil,R}$) are assumed constant at an average value of 3 [99];
- The mass flow rate of the biomethane is taken equal to $G_{CH_4} = 0.03$ [kg/s] [99];
- The exit temperature of the biomethane after the liquefaction process in the PHEX is considered equal to $T_2 = -158$ [°C], which is a typical value reported in literature [99];
- The pressure of the refrigerant (Refr) before entering the two-stage intercooled compressor is taken equal to $p_R^I = 1.5$ [bar]. Considering negligible pressure drops in the PHEX and SHEX, this pressure is also assumed for Refr' and Refr" at the inlet of the PHEX and SHEX, respectively [99];
- The mass flow rate of the refrigerant (Refr') flowing in the PHEX is set to $G_R' = 0.033$ [kg/s], according to [99];
- The coefficient taking in account the turbulence enhancement produced by the internal turbulence enhancer is considered equal to $k_{h,H} = 1.6$ [99].

A summary of the values considered for all these thermodynamic and operating parameters used as inputs in the optimization problem is presented in the following **Table 1**.

Table 1. *Input thermodynamic and operating parameters and corresponding nomenclature.*

Parameter	Symbol	Value
Biomethane supply temperature	T_s	30 [°C]
Biomethane supply pressure	p_s	1.5 [bar]
Biomethane inlet temperature of the first compressor	${T_{CH_4}}^{I} = T_s$	30 [°C]
Biomethane inlet temperature of the second compressor	${T_{CH_4}}^{II}$	25 [°C]
Efficiency of the biomethane compressors	${\eta_{CH_4}}^{I} = {\eta_{CH_4}}^{II}$	0.82
Coefficient of performance of the biomethane chiller	COP_{chil,CH_4}	3
Biomethane mass flow rate	G_{CH_4}	0.03 [kg/s]
Biomethane outlet temperature in the $PHEX$	T_2	-158 [°C]
Operating pressure of the refrigerant ($Refr$)	$p_R{}'$	1.5 [bar]
Efficiency of the refrigerant compressors	${\eta_R}^{I} = {\eta_R}^{II}$	0.82
Coefficient of performance of the refrigerant chiller	$COP_{chil,R}$	3
Refrigerant ($Refr'$) mass flow rate in the $PHEX$	$G_R{}'$	0.033 [kg/s]
Turbulence enhancement coefficient produced by the internal turbulence enhancer	$k_{h,H}$	1.6
Biomethane supply temperature	T_s	30 [°C]
Biomethane supply pressure	p_s	1.5 [bar]

Instead, **Table 2** provides a summary of the key geometric parameters related to the heat exchangers, both PHEX and SHEX, used as inputs. Some of these parameters are presented as ratios of specific quantities, such as the external diameter to internal diameter of the internal pipe. **Table 3** and **Table 4** display the intermediate variables required to calculate the two target functions, along with their corresponding nomenclature.

***Table 2**. Input geometric parameters and corresponding nomenclature.*

Parameter	Symbol	Value
$PHEX$ number of pipes	$(n_t)_{PHEX}$	25
$SHEX$ number of pipes	$(n_t)_{SHEX}$	40
Turbulence enhancement coefficient (internal pipe)	k_{A_H}	0.196
Pressure drop enhancement coefficient (internal pipe)	$k_{\Delta p_H}$	4.35
Effective areas of the hot fluid	A_H	61.73 [mm^2]
Effective areas of the cold fluid	A_C	110.74 [mm^2]
Hydraulic diameter of the cold fluid	d_{hC}	3 [mm]
Hydraulic diameter of the hot fluid	d_{hH}	1.992 [mm]
Turbulence enhancer perimeter	p_p	55 [mm]
Internal diameter of the internal pipe	$d_{i,i}$	20 [mm]
External diameter/internal diameter of the internal pipe	$d_{e,i}/d_{i,i}$	1.1
Intern. diameter of the ext. pipe/ext. diameter of the internal pipe	$d_{i,e}/d_{e,i}$	1.136
Roughness of the pipes/internal diameter of the internal pipe	$\varepsilon/d_{i,i}$	0.001

***Table 3.** Intermediate variables for the calculation of the performative variables and corresponding nomenclature.*

Variable	Symbol
Gas constant of the biomethane	R_{CH_4}
Gas constant of the refrigerant	R_R
Compression ratios of the first and second biomethane compressor	$(\beta^I_{CH_4}, \beta^{II}_{CH_4})$
Compression ratios of the first and second refrigerant compressor	$(\beta^I_R, \beta^{II}_R)$
Refrigerant inlet temperature of the first compressor	$T_R{}^I$
Refrigerant inlet temperature of the first compressor	$T_R{}^{II}$
Biomethane outlet enthalpy from the second compression stage	i^{II}_{ex,CH_4}
Refrigerant outlet enthalpy from the second compression stage	$i^{II}_{ex,R}$
Biomethane $PHEX$ inlet enthalpy	i_1
$Refr$' and $Refr$'' inlet enthalpy	i_3
$Refr$' and $Refr$'' outlet enthalpy	i_4
$Refr\ SHEX$ outlet enthalpy	i_5
$Refr\ SHEX$ inlet enthalpy	i_6
$Refr$ mass flow rate	G_R
$Refr$'' mass flow rate in the SHEX	G''_R
Compression power of the refrigerant	$P_{compr,R}$
Chilling power of the refrigerant	$P_{chil,R}$
Compression power of the biomethane	P_{compr,CH_4}

***Table 4**. Intermediate variables for L_{tot} calculation and corresponding nomenclature.*

Variable	Symbol
Inlet temperatures of the hot and cold fluids in module i	$((T_{in,H})_i, (T_{in,C})_i)$
Outlet temperatures of the hot and cold fluids in module i	$((T_{out,H})_i, (T_{out,C})_i)$
Thermal power exchanged in module i	$(\dot{Q}_{exc})_i$
Average temperatures of the hot and cold fluids in module i	$((\overline{T_H})_i, (\overline{T_C})_i)$
Average velocities of the hot and cold fluids in module i	$((\overline{V_H})_i, (\overline{V_C})_i)$
Average densities of the hot and cold fluids in module i	$((\overline{\rho_H})_i, (\overline{\rho_C})_i)$
Average viscosities of the hot and cold fluids in module i	$((\overline{\mu_H})_i, (\overline{\mu_C})_i)$
Average specific heats at constant pressure of the hot and cold fluids in module i	$((\overline{cp_H})_i, (\overline{cp_C})_i)$
Average thermal conductivities of the hot and cold fluids in module i	$((\overline{\lambda_H})_i, (\overline{\lambda_C})_i)$
Average Reynolds number of the hot and cold fluids in module i	$((\overline{Re_H})_i, (\overline{Re_C})_i)$
Average Prandtl number of the hot and cold fluids in module i	$((\overline{Pr_H})_i, (\overline{Pr_C})_i)$
Friction factor for smooth tubes in module i	$(\xi)_i$
Average Nusselt number of the hot and cold fluids in module i	$((\overline{Nu_H})_i, (\overline{Nu_C})_i)$
Convective heat exchange coefficient for the hot and the cold fluid in module i	$\left((\overline{h_H})_i, (\overline{h_C})_i\right)$
Vapor quality of the fluid in module i	q
Density of the liquid part of the cold fluid in module i	$(\overline{\rho_{C,l}})_i$
Density of the vapor part of the cold fluid in module i	$(\overline{\rho_{C,v}})_i$
Viscosity of the liquid part of the cold fluid in module i	$(\overline{\mu_{C,l}})_i$
Viscosity of the vapor part of the cold fluid in module i	$(\overline{\mu_{C,v}})_i$
Specific heat of the liquid part of the cold fluid in module i	$(\overline{cp_{C,l}})_i$
Specific heat of the vapor part of the cold fluid in module i	$(\overline{cp_{C,v}})_i$
Thermal conductivity of the liquid part of the cold fluid in module i	$(\overline{\lambda_{C,l}})_i$
Thermal conductivity of the vapor part of the cold fluid in module i	$(\overline{\lambda_{C,v}})_i$
Martinelli parameter in module i	$(\overline{x_{tt}})_i$
Reynolds number factor	F
Prandtl number of the liquid film in module i	$(\overline{Pr_{lf}})_i$
Reynolds number of the liquid film in module i	$\left(\overline{Re_{lf}}\right)_i$
Convection contribution from wall to liquid film in module i	$\left(\overline{h_{lf}}\right)_i$
Convective heat transfer coefficient of the cold fluid in module i (in two-phase flows)	$\left(\overline{h_C}\right)_i$
Temperature difference 1 between the hot and cold fluid in module i	$\Delta T_1 = (T_{in,H})_i - (T_{out,C})_i$
Temperature difference 2 between the hot and cold fluid in module i	$\Delta T_2 = (T_{out,H})_i - (T_{in,C})_i$
Logarithmic mean temperature difference in module i	$(\overline{\Delta T})_i$
Mean heat transfer coefficient in module i	U_i
Friction factors in rough tubes for the hot and the cold fluids in module i	$((f_H)_i, (f_C)_i)$
Length for the heat exchange in module i	Δx_i

3.1.1.2.1. The effects of a domain exploration on the system performance

In order to assess how the variation of the thermodynamical inputs affected the performance of the system, in the first study a light domain exploration was performed. $T_1 = T_6$ and $p_{CH_4} = p_R$ were varied as specified in **Table 5**, also considering that T_4 has been constrained to be $T_4 = (T_1 - 7)°C$.

***Table 5**. Explored values of the input variables.*

p_{CH_4} $[bar]$	60	58	56	54	52	50	48	46
T_1 $[°C]$	10	-7.5	-5	-2.5	0	2.5	5	

Table 6 and **Table 7** show the outcome of the calculations for COP_{tot} and L_{tot}, respectively. Some combinations of the explored input values have led to temperature cross in the heat exchangers and, therefore, to unfeasible lengths. These cases are highlighted in red in **Table 6** and **Table 7**. Other sets of values have also been discarded, namely those cases that create a temperature difference between the hot fluid and the cold fluid less than 2°C. The aforementioned cases have been highlighted in orange in **Table 6** and **Table 7**. The values highlighted in green are those obtained in [34] for the same molar fraction composition of the refrigerant.
The results shown in **Table 6** and **Table 7** show that the combination of (COP_{tot}, L_{tot}) can further be improved, compared to results of [34], by adjusting the operating data. The results of **Table 6** and **Table 7** are also shown, in graphical form, in **Figure 23**, which plots the trend of the two output parameters as a function of p_{CH_4} and T_1 and does not comprise the orange-highlighted sets of values.

***Table 6**. Results concerning the overall coefficient of performance, COP_{tot}.*

COP_{tot}		p_{CH_4} $[bar]$							
		60	58	56	54	52	50	48	46
T_1 $[°C]$	-10	NaN	NaN	0.2843	0.2844	0.2842	0.2838	0.2832	0.2822
	-7.5	NaN	NaN	0.2797	0.2794	0.2788	0.2780	0.2769	0.2753
	-5	NaN	0.2746	0.2746	0.2739	0.2729	0.2715	0.2698	0.2676
	-2.5	0.2704	0.2697	0.2688	0.2676	0.2661	0.2643	0.2619	0.2590
	0	0.2648	0.2637	0.2624	0.2607	0.2586	0.2561	0.2531	0.2494
	2.5	0.2585	0.2570	0.2552	0.2529	0.2502	0.2470	0.2432	0.2386
	5	0.2515	0.2495	0.2471	0.2443	0.2409	0.2369	0.2321	0.2265

***Table 7**. Results concerning the total length of the heat exchangers, L_{tot}.*

L_{tot} $[m]$		p_{CH_4} $[bar]$							
		60	58	56	54	52	50	48	46
T_1 $[°C]$	-10	NaN	NaN	10.15	9.39	9.41	9.59	10.13	11.18
	-7.5	NaN	NaN	9.47	9.32	9.50	9.76	10.11	11.31
	-5	NaN	9.48	9.20	9.27	8.99	9.29	9.81	11.42
	-2.5	9.81	9.23	9.04	9.05	9.25	9.31	9.79	10.76
	0	9.07	8.94	9.03	9.22	9.39	9.77	10.34	10.97
	2.5	8.93	8.96	8.98	9.17	9.44	9.71	10.29	11.25
	5	9.15	9.18	8.84	9.01	9.13	9.47	9.96	10.63

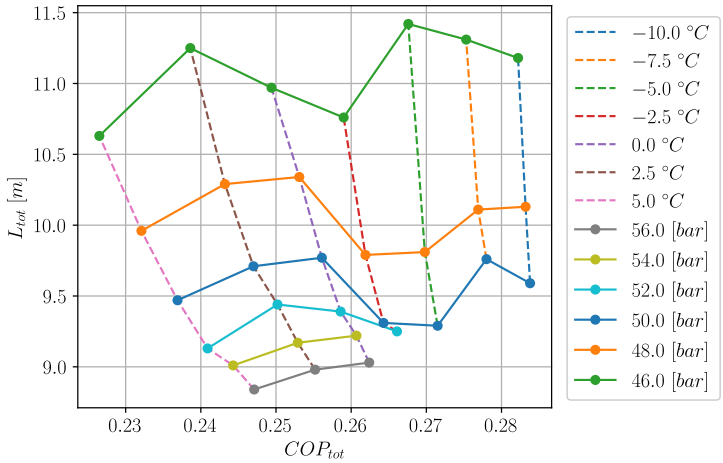

***Figure 23**. Graphical form of the data collected in **Table 6** and **Table 7** (only feasible values).*

Analysing **Figure 23**, the following considerations can be deduced:

- In the considered cases, for fixed values of p_{CH_4}, the decrease in T_1 causes a corresponding increase in the COP_{tot} value (representing the performance of the system in this analysis). The maximum of COP_{tot} is obtained for the minimum possible value of T_1. Instead, for fixed values of p_{CH_4}, the trend of L_{tot} is not predictable, presenting oscillations as a function of T_1.
- For fixed values of T_1, the increase in p_{CH_4} always makes COP_{tot} increase; instead, for fixed values of T_1, L_{tot} constantly decreases with the increasing pressure.
- The maximum value of COP_{tot} is 0,2838, obtained for p_{CH_4} = 50 bar and $T_1 = -10°C$; the minimum value of L_{tot} is 8,84 m, obtained for p_{CH_4} = 56 bar and $T_1 = 5°C$.
- The pressure drops are not shown, as they are very low for all the cases considered, being much less than 1 bar.
- This analysis has shown that imposing $T_1 = -10°C$ could be a very good solution to obtain high values of COP_{tot}. The downside is that complex and expensive chillers capable of achieving such low temperatures are needed. Neglecting this issue, as an example, the solution with $T_1 = -10°C$ and
- p_{CH_4} = 50 bar (producing G_R = 0.09597 kg/s) provides a good value of L_{tot} (9.59 m) and a high value of COP_{tot} (0.2838). This COP_{tot} value corresponds to an overall specific consumption equal to 0.72854 kWh/kg_{CH_4}. For this solution, the overall pressure drop (calculated as the sum of the pressure drops in all the modules of the PHEX and the SHEX) is less than 0.1 bar. For this solution, **Figure 24** shows the graphs of temperatures vs thermal power, obtained for the PHEX (**Figure 24**a) and for the SHEX (**Figure 24**b).

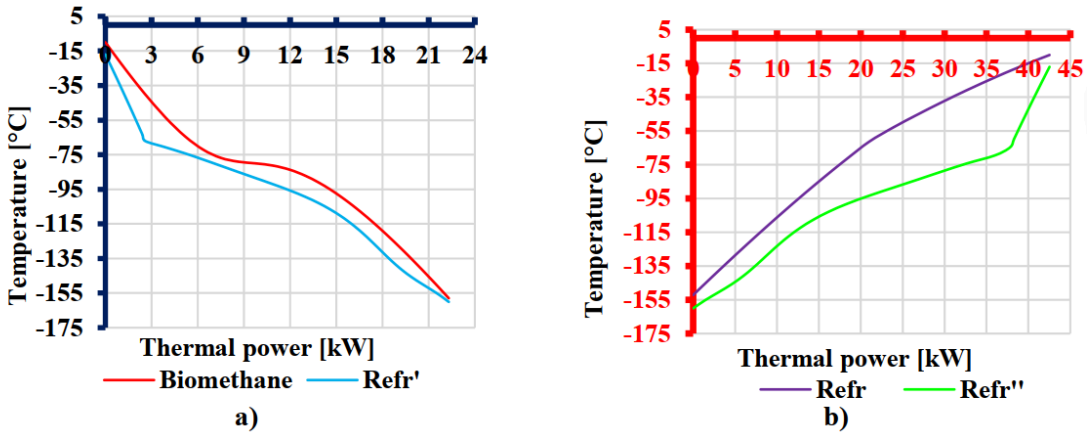

***Figure 24**. Temperature-thermal power: (a) PHEX, (b) SHEX.*

In conclusion, Tables and graphs were obtained to illustrate how the two key variables change as a function of the input parameters. Compared to our previous studies, this analysis has shown that COP_{tot} can further be increased by decreasing T_1 for a given value of p_{CH_4}. However, this choice would lead to the use of complex and expensive chillers to be placed upstream of the heat exchangers. In this parametric analysis, the maximum registered value of COP_{tot} was 0.2838 (corresponding to an overall specific consumption equal to 0.72854 kWh/kg_{CH_4}) and the minimum registered length was $L_{tot} = 8.84\,m$.

3.1.1.2.2. Optimisation of the performance by means of the use of the MOGA II algorithm

The computational domain in this specific case is very extensive for comprehensive exploration. Consequently, there is a need for an exploration criterion, specifically an optimization algorithm [100]. This algorithm plays a vital role in identifying the direction of improvement and efficiently allocating computational resources, leading to a substantial reduction in computational costs. This eliminates the necessity for exhaustive exploration of each design point of the computational domain. To effectively enable the algorithm to trace the direction of improvement, it is imperative to choose an appropriate one. In this context, a genetic algorithm is a frequently employed solution. Its unique ability to trace the direction of improvement makes it well-suited for this task.

Below, the design input variables (**Table 8**), along with the Design of Experiments (DOE) and the algorithm utilized to obtain it, will be specified. Subsequently, the objectives and constraints imposed for the resolution of the optimization problem will be outlined. Lastly, the optimization algorithm employed to achieve the optimal values will be described in detail.

The multi-objective optimization problem is configured with three degrees of freedom. Specifically, the three thermodynamic quantities, selected as design input variables for optimizing the proposed biomethane liquefaction plant, are detailed below (refer to **Figure 18** for a better understanding of symbols). Please note that $\Delta T_{1,4}$ indicates the temperature difference between the pre-compressed and pre-cooled gaseous biomethane at the PHEX inlet (T_1) and the refrigerant ($Refr'$ and $Refr''$) exiting the PHEX and SHEX (T_4), i.e., $\Delta T_{1,4} = T_1 - T_4$.

***Table 8**. Design input variables for optimization: Range Values, Step Size, and Maximum Design Points.*

Desing Input Variable	Range Values	Step Size	Maximum Number of Design Points
$T_1 = T_6$	-10 ÷ 10 [°C]	1 °C	21
$p_{CH_4} = p_R$	46 ÷ 60 [bar]	1 bar	15
$\Delta T_{1,4}$	3 ÷ 10 [°C]	1 °C	8

It is important to note that, the temperature (T_6) and the pressure (p_R) of the whole pre-compressed and pre-cooled refrigerant ($Refr$) at the SHEX inlet are constrained in this optimization problem. Specifically, T_6 and p_R are assumed to be equal to T_1 and p_{CH_4}, respectively. Therefore, since $T_6 = T_1$ and $p_R = p_{CH_4}$, these thermodynamic quantities can be considered as input variables of the optimization process. This strategy was selected in order to make the evaporation curve of the refrigerant very close to the cooling curve of the biomethane [99].

Table 8 outlines the design input variables involved in the optimization problem, along with their value ranges, the considered variation step, and the resulting maximum number of design points obtained. To comprehensively explore the optimization calculation domain, the total number of design points required can be determined by multiplying the maximum number of design points for each input variable. This results in a total of 2520 design points. To significantly reduce this number while still considering all potential values for each input variable, the Uniform Latin Hypercube (ULH) algorithm was employed. This algorithm generates a predefined number of design points, ensuring that every potential value for each variable is represented at least once [101]. With this approach, an initial population (DOE) consisting of thirty design points was generated. These design points, labelled with identifiers (ID) ranging from 0 to 29, are detailed in **Table 9**, alongside the respective values assigned to each input thermodynamic variable.

***Table 9**. Initial population (DOE).*

ID	T_1 [°C]	p_{CH_4} [bar]	$\Delta T_{1,4}$ [°C]
0	0	57	3
1	-6	52	10
2	2	54	5
3	8	52	7
4	-1	59	7
5	-7	48	9
6	-9	51	9
7	3	59	8
8	3	56	5
9	5	50	7
10	-2	57	10
11	1	45	6
12	-10	48	3
13	5	53	6
14	10	45	4
15	-5	58	9
16	-10	47	3
17	-3	60	7
18	-8	50	8
19	-4	50	4
20	7	48	10
21	9	55	3
22	-2	51	4
23	4	47	10
24	-1	46	6
25	8	49	8
26	6	57	4
27	8	54	8
28	-7	53	5
29	-5	60	5

To ensure optimal performance of the proposed liquefaction plant, two main output variables are closely monitored during the optimization process. The first output variable is the specific energy consumption (E_{n2}), enabling the evaluation of the energy efficiency of the system. The second output variable is the total tubes length (L_{tot}), which reflects the cost of the heat exchangers. Specifically, it combines the lengths of tubes from both the PHEX (L_{PHEX}) and the SHEX (L_{SHEX}), resulting in $L_{tot} = L_{PHEX} + L_{SHEX}$.

These variables (E_{n2} and L_{tot}) are established as the objective functions of the optimization problem, with the goal of minimizing both of them. Additionally, it is important to ensure that the temperature difference (ΔT_2) between the outlet temperature of the hot fluid ($(T_{out,H})_i$) and the inlet temperature of the cold fluid ($(T_{in,C})_i$) remains above 2°C in each PHEX and SHEX module to avoid unrealistic scenarios. **Table 10** provides an overview of the objective functions and constraints assumed in the optimization problem.

Table 10. *Objective functions and constraints assumed in the optimisation problem.*

Variable	Typology	Goal
En_2	Objective Function	Minimize
L_{tot}	Objective Function	Minimize
ΔT_2	Constraint	Above 2 [°C]

The Multi Objective Genetic Algorithm (MOGA II) optimization algorithm was chosen to find the optimal values for the objective functions. This evolutionary algorithm utilizes a directional crossover operator for fast convergence and a smart multisearch elitism for a uniform spread of solutions [102]. It has proven to be highly efficient in solving multi-objective optimization problems [103].

Inspired by Charles Darwin's evolutionary theory, the MOGA II algorithm treats the initial design points from the DOE (refer to previous **Table 9**) as individuals. In this context, each individual's genetic material corresponds to a specific design point, evaluated based on a combination of T_1, p_{CH_4} and $\Delta T_{1,4}$ values.

The initial individuals from the DOE represent the zero generation. As the algorithm progresses through successive generations, obtained by recombining individuals' genetic material, it generates new individuals with improved genetic material (also referred to as superior fitness). To facilitate this recombination process, the MOGA II algorithm employs four distinct genetic operators:

- Selection: This operator involves simply copying the genetic material of each individual to the next generation without making any modifications;
- Classical crossover: This operator enables the genetic material of two individuals (parents) to be recombined in order to obtain an individual (child) with superior fitness;
- Directional crossover: This operator determines the direction of improvement for the optimization problem. It compares an individual's fitness from a specific generation with its parents' fitness from the previous generation. Subsequently, it creates a new individual by moving in a randomly weighted direction within the range determined by the individual and its parents [42]. This operator has proven to enhance the algorithm's convergence across a wide range of numerical problems [102], [103];
- Mutation: This operator changes the genetic material in a random way, ensuring algorithm robustness. This introduces additional randomness, which allows for a deeper exploration of the calculus domain and prevents premature convergence of the algorithm.

At each step of the reproduction process, one of the four operators is selected based on predefined probabilities and applied to the current individual.

Once each generation, containing the same number of individuals as in the DOE, is formed, the algorithm identifies individuals with the most favourable fitness, known as non-dominated design points. These are then included in the "elite set", which consists of individuals excelling in optimizing all previously detailed objective functions, i.e. E_{n2} and L_{tot}. Elitism is crucial in multi-objective optimization for preserving individuals closest to the Pareto front and those with the best dispersion [102], [103]. Consequently, when

updating the elite set, any duplicated or dominated design points are discarded. This process is repeated for every generation.

The MOGA II algorithm was implemented using the Esteco modeFRONTIER software [104]. Its graphic interface provides a manual configuration option, allowing users to customize the algorithm settings. **Table 11** displays all the chosen values for the configurable parameters.

***Table 11**. Objective functions and constraints assumed in the optimization problem.*

Parameters	
Number of generations	30
Algorithm type	MOGA – Adaptive evolution
GA operators	
Probability of directional crossover	0.5
Probability of selection	0.05
Probability of mutation	0.1
DNA string mutation ratio	0.05
Advanced parameters	
Elitism	Enabled
Treat constraints	Penalizing objectives
Reject input-unfeasible designs	☑
Random generator seed [0,999]	1
Category parameters	
Categorize generations	☑
Categorize operators	☑

Considering these settings, the optimization process was conducted across thirty generations, each consisting of thirty individuals (design points). Notably, the utilization of the evolutionary MOGA-II algorithm reduced the required calculations from an estimated 2520 to 900 design points. Furthermore, out of these 900 design points calculated, any unfeasible or erroneous design points were excluded.

Figure 25 depicts the outcomes of the calculations, showing design points that converge to the high-efficiency region of the diagram over the generations. It displays the two objective functions, E_{n2} on the x-axis and L_{tot} on the y-axis, with the thirty different generations (from 0 to 29) identifiable by a chromatic scale. Additionally, both the Pareto front and the design point analysed in our previous work [99] are highlighted.

Examining the graph, it is crucial to observe that refining the input thermodynamic variables through the optimization process enables achieving significantly better performance compared to the previous design point analysed in [99]. **Table 12** provides the Pareto front design points, taking into account both the input thermodynamic variable values and the objective function values.

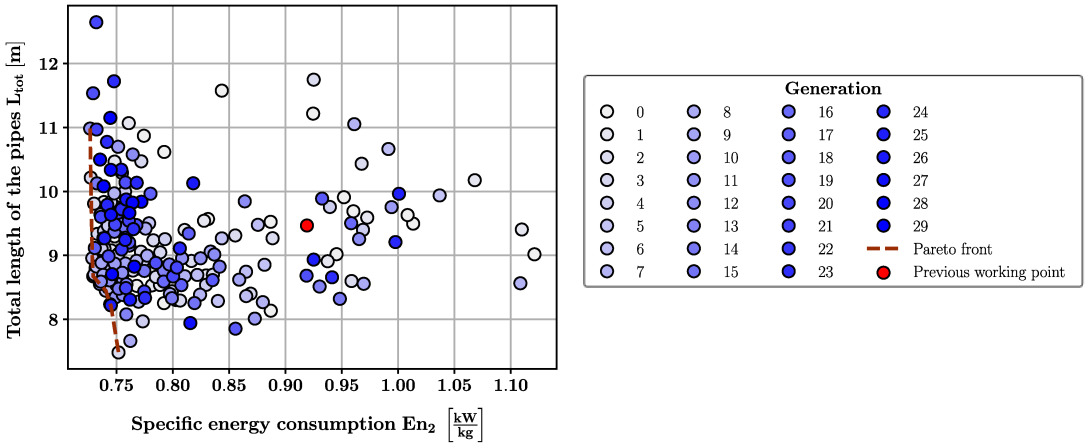

Figure 25. *L_{tot} and $E_{n,2}$ plot showing the calculated design points over the MOGA II generations (identified with a chromatic scale), the Pareto front and the previous design point examined in [99].*

Table 12. *Pareto front design points.*

ID	$T_1[°C]$	$p_{CH_4}[bar]$	$\Delta T_{1,4}$ [°C]	En_2 $[kW/kg]$	L_{tot} $[m]$
355	-10	48	5	0.7266	10.98
112	-10	49	6	0.7272	10.22
166	-10	51	8	0.7285	8.96
100	-10	52	9	0.7293	8.67
325	-9	53	9	0.7353	8.55
158	-9	52	10	0.7405	8.45
503	-8	54	10	0.7444	8.24
774	-10	45	8	0.7450	8.22
75	-10	45	10	0.7518	7.48

The random distribution of design points generated by the MOGA II algorithm means that the entire computational domain, encompassing all possible combinations of input thermodynamic variables, has not been thoroughly explored. To address this limitation and examine the relationship between the objective functions and input thermodynamic variables, a fitting process was conducted using all the collected data from the optimization process. Notably, only the fitting for the specific energy consumption (E_{n2}) provided some satisfying results, with a correlation factor equal to $R^2 = 0.979143$. Specifically, E_{n2} can be expressed as a second-degree polynomial function of the three input thermodynamic variables, as depicted in (44):

$$En_2 = c_1 + c_2 \cdot T_1 + c_3 \cdot p_{CH_4} + c_4 \cdot \Delta T_{1,4} + c_5 \cdot T_1^2 + c_6 \cdot p_{CH_4}^2 + c_7 \cdot \Delta T_{1,4}^2 \qquad (44)$$

This equation provides a good approximation of the calculated En_2 data over the entire computational domain. The coefficients for this equation are listed in **Table 13**. The graphical representation of (44) is depicted in **Figure 26**.

***Table 13**. Values of the coefficients used in (44).*

Coefficient	Value	R^2
c_1	0.766363	
c_2	0.015667	
c_3	0.008808	
c_4	-0.002156	0.979143
c_5	0.000398	
c_6	-0.000150	
c_7	0.000449	

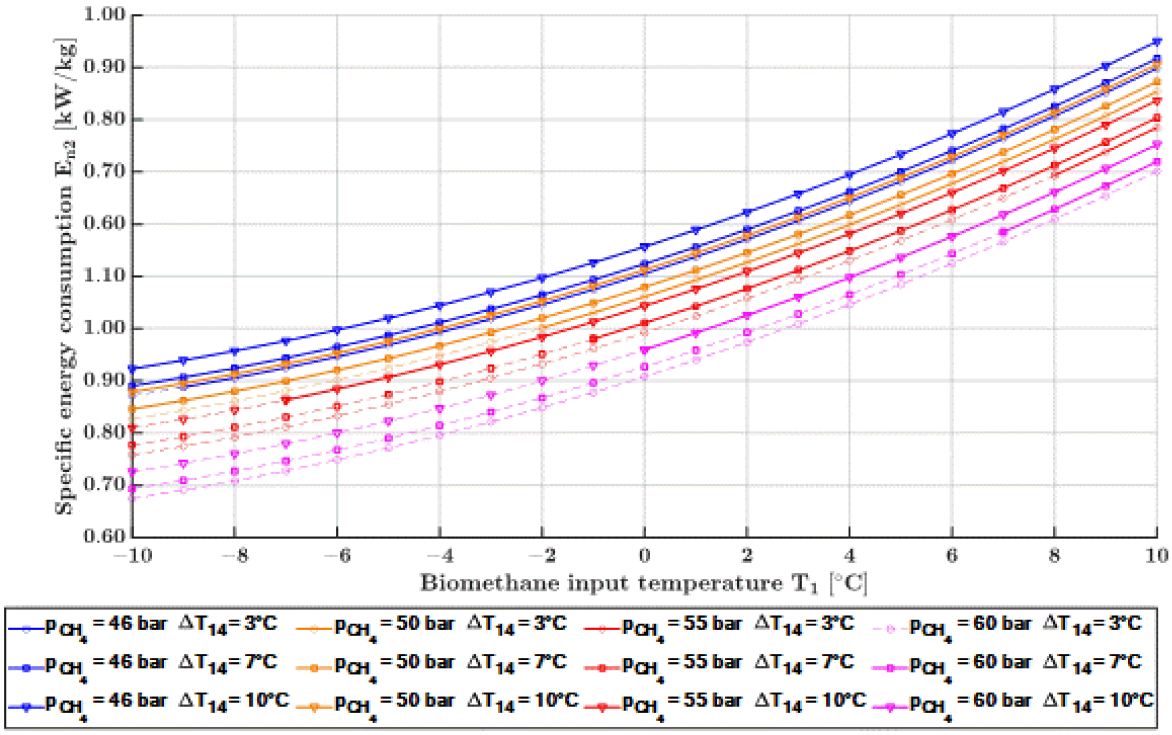

***Figure 26**. Influence of the input thermodynamic variables on the objective function E_{n2} .*

It numerically describes the relationship of the specific energy consumption (E_{n2}) while considering variations in the three input thermodynamic variables within the entire computational domain. Dotted lines on the graph signify unfeasible conditions, while continuous lines represent physically plausible results.

Upon examining **Figure 26**, several key observations can be noted:

- Fixed values for all input thermodynamic variables (p_{CH_4}, T_1 and $\Delta T_{1,4}$) result in well-defined values of En_2;
- Maintaining constant values for p_{CH_4} and T_1 while increasing $\Delta T_{1,4}$ leads to a rise in En_2;
- With fixed values for p_{CH_4} and $\Delta T_{1,4}$, increasing T_1 causes En_2 to increase;
- When p_{CH_4} remains constant, increasing values of both T_1 and $\Delta T_{1,4}$ correspond to rising values of En_2, with $\Delta T_{1,4}$ having a greater impact on the increasing trend of En_2 compared to T_1;
- Fixed values of T_1 and $\Delta T_{1,4}$, with rising values for p_{CH_4}, result in decreasing values of En_2;
- Fixed values of T_1, with rising values of $\Delta T_{1,4}$ and p_{CH_4}, exhibit a decreasing trend in En_2 primarily due to the influence of p_{CH_4}, which dominates the increasing trend given by $\Delta T_{1,4}$;
- With fixed values for T_1 and $\Delta T_{1,4}$, increasing p_{CH_4} causes En_2 to decrease;
- When T_1 remains constant, increasing values of both p_{CH_4} and $\Delta T_{1,4}$, En_2 shows a decreasing trend due to p_{CH_4}, which is dominant compared to the increasing trend caused by $\Delta T_{1,4}$;
- When both p_{CH_4} and T_1 increase, while $\Delta T_{1,4}$ remains fixed, En_2 exhibits an increasing trend driven by T_1, which is dominant compared to the decreasing trend caused by p_{CH_4};
- For increasing values of all input variables (p_{CH_4}, T_1 and $\Delta T_{1,4}$), En_2 demonstrates an increasing trend given by T_1, which exerts greater influence on the increasing trend provided by $\Delta T_{1,4}$, while also dominating the decreasing trend provided by p_{CH_4}.

A summary of the trend observed in the objective function En_2, concerning the variation of the input thermodynamic variables (p_{CH_4}, T_1 , and $\Delta T_{1,4}$) is provided in **Figure 27**. Additionally, the influence of varying the input thermodynamic variables (p_{CH_4}, T_1 and $\Delta T_{1,4}$) on both the objective functions (E_{n2} and L_{tot}) can be assessed by examining the following **Figure 29**. Specifically, when considering the impact of these variables on the objective functions, it becomes evident that lower values of T_1, intermediate values of p_{CH_4}, and higher values of $\Delta T_{1,4}$contribute to minimizing both E_{n2} and L_{tot}.

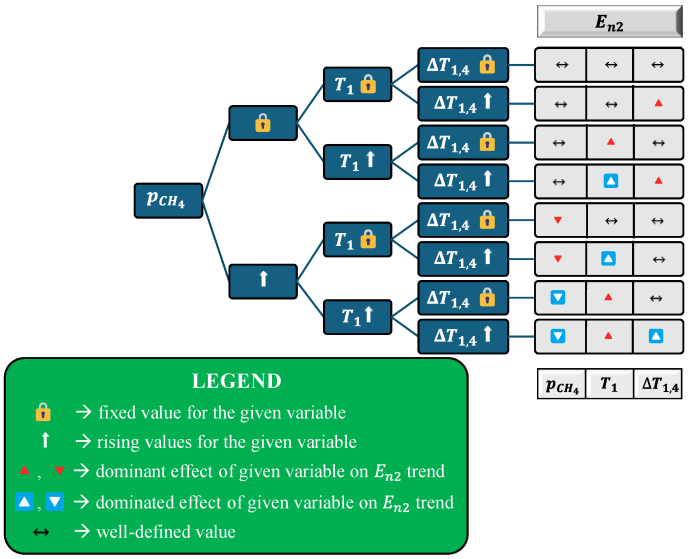

***Figure 27**. Summary scheme evidencing the influence of varying the input thermodynamic variables on the objective function E_{n2} .*

In **Figure 28** the Pareto front is shown, representing the top-performing solutions, encompassing all non-dominated design points collected across the thirty generations. It illustrates potential optimal solutions derived from the optimization process. To determine the optimal solution from these design points, a decision criterion becomes indispensable.

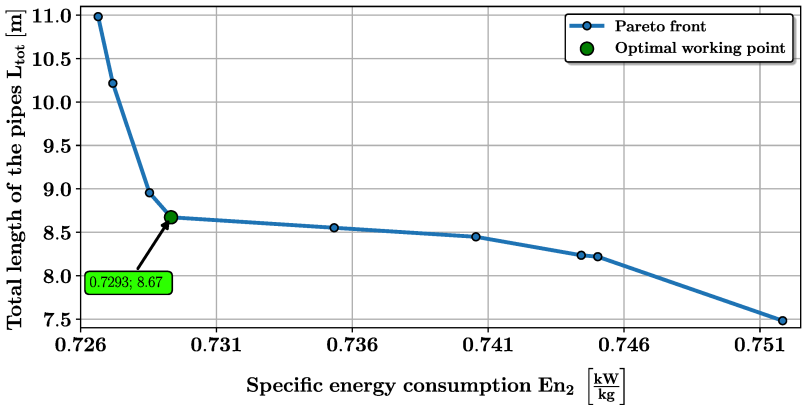

***Figure 28**. Pareto Front generated by the MOGA II algorithm for the optimization problem.*

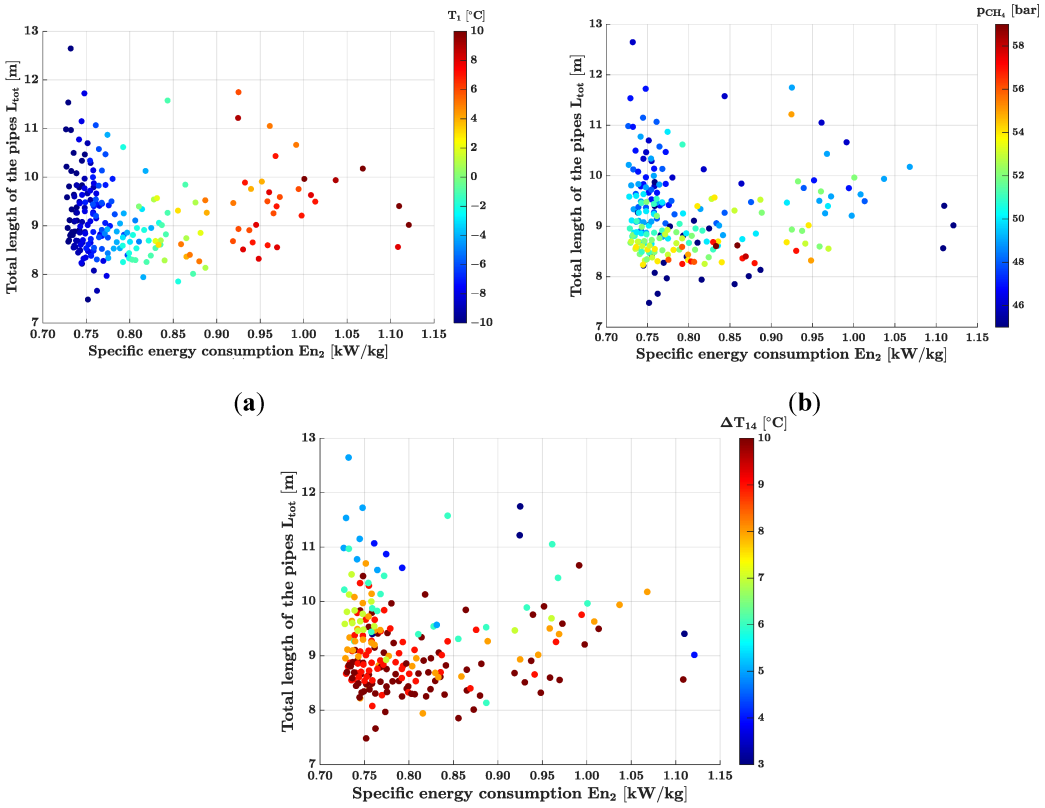

Figure 29. $L_{tot} - E_{n2}$ *plots showing the influence of the input thermodynamic variables on both the objective functions:* ***(a)*** T_1 *;* ***(b)*** p_{CH_4}*;* ***(c)*** ΔT_{14} .

It is important to note that, when moving across the Pareto front from right to left, the curve demonstrates to possess a limited slope until a distinct turning point is encountered. Beyond this particular juncture, the curve exhibits a significantly steeper slope. Consequently, this turning point represents the optimal design point, where the objective functions (En_2 and L_{tot}) are satisfied with low values for both. The optimal design point is highlighted in green on the Pareto front provided in **Figure 28**.

The same result can be obtained using the "parallel coordinates" tool available within the modeFRONTIER software [45]. This tool enables filtering of the Pareto front design points by setting value ranges for the objective functions using sliders. In **Figure 30**, for instance, En_2 has been set below 0.73 [kW/kg] (highlighted in a red box), and the L_{tot} slider (also highlighted in red) has been adjusted to achieve the minimum available length, revealing only one possible design point. Automatically, design points that don't meet these constraints are hidden. The remaining design point, highlighted in green, signifies the optimal solution that best fulfils the objective functions simultaneously. Its corresponding ID, 100, and the recorded values of input thermodynamic variables and objective functions are detailed in **Table 12**. The ID is also visible in **Figure 30**.

Figure 31 shows the Temperature-Entropy thermodynamic plot for both the biomethane (**Figure 31a**) and the refrigerants ($Refr$, $Refr'$ and $Refr''$)(**Figure 31b**) under the optimal condition obtained through the optimization process. These graphs reveal that the curves of $Refr'$ and $Refr''$ are, for a large part, situated within the two-phase zone well below the critical point, which validates the use of Chen's correlation. Additionally, it is important to note that the isobaric curves for refrigerant exhibit a non-isothermal behaviour in the two-phase zone, primarily due to the considered composition of the refrigerant mixture.

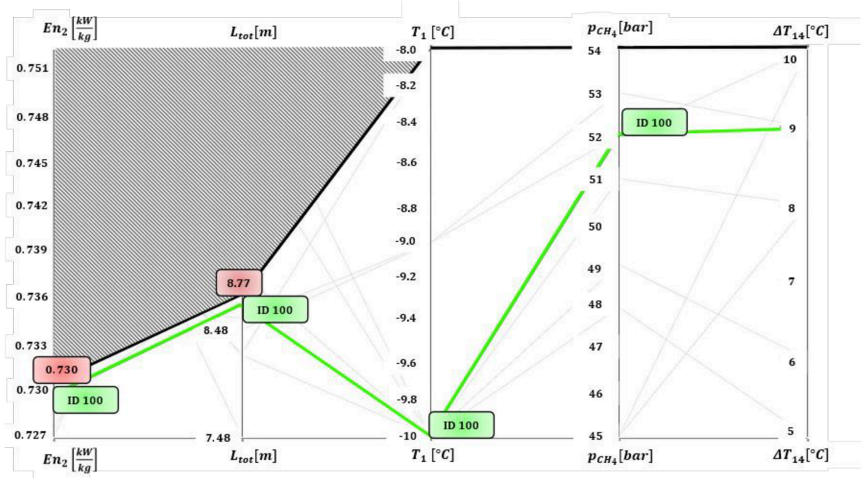

***Figure 30**. Optimal design point using the "parallel coordinates" tool available in modeFRONTIER.*

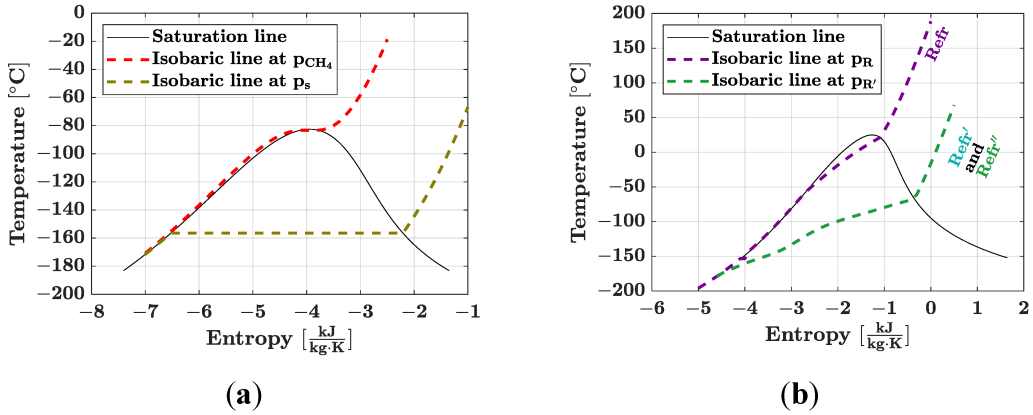

(a) **(b)**

***Figure 31.** Temperature-Entropy diagrams for **(a)**: biomethane and **(b)**: refrigerant under the optimal conditions.*

Furthermore, **Figure 32** illustrates the Temperature-Thermal power plots for both the PHEX (**Figure 32a**) and the SHEX (**Figure 32b**), taking into account the identified optimal condition. As shown in the graph, there is no temperature cross inside both the PHEX and SHEX, with temperature difference at the pinch point for the PHEX equal to $\Delta T_{pp} = 6.55\ [K]$.

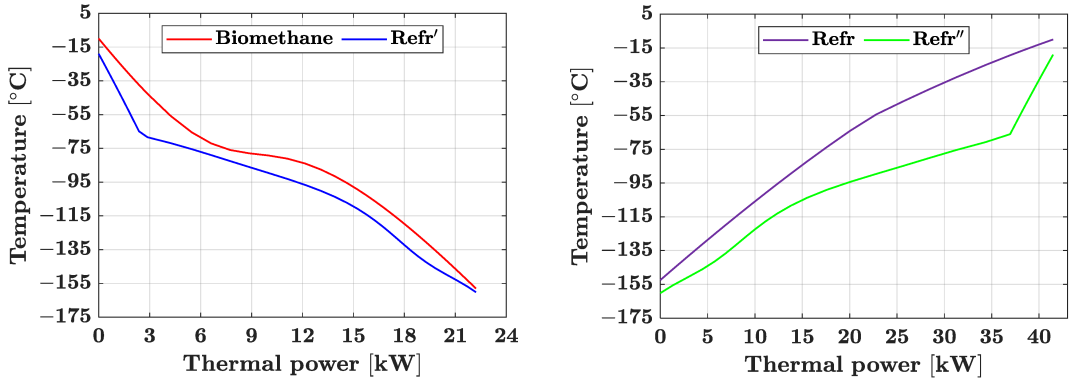

(a) **(b)**

***Figure 32**. Temperature-Thermal power plot for the optimal design point: **(a)** PHEX; **(b)** SHEX.*

In conclusion, **Table 1Table 14** presents the values of heat exchanger lengths, pressure drops, and performance coefficients for the entire system under optimal conditions. Additionally, it includes main intermediate variable values for the biomethane liquefaction plant, including the temperature difference at the pinch point for the PHEX. Notably, the table highlights that the pressure drops in both heat exchangers are minimal, indicating they can be considered negligible, consistent with the evaluation in [99].

Table 14. *Values assumed by the main intermediate variables and output variables for the optimal design point.*

Parameter	Symbol	Value
Compression ratios of the biomethane compressors	$\beta_{CH_4}^{I} = \beta_{CH_4}^{II}$	5.9
Compression ratios of the refrigerant compressors	$\beta_R{}^{I}=\beta_R{}^{II}$	5.9
Refrigerant inlet temperature ($Refr'$ and $Refr''$)	T_3	-160.2 [°C]
Refrigerant ($Refr$)inlet temperature of the first compressor	$T_R{}^{I} = T_4$	-19 [°C]
Refrigerant ($Refr$) inlet temperature of the second compressor	$T_R{}^{II} = T_8$	74.4 [°C]
Refrigerant ($Refr''$) mass flow rate in the $SHEX$	G_R''	0.062 [kg/s]
Refrigerant ($Refr$) mass flow rate	G_R	0.095 [kg/s]
Temperature difference at the pinch point	ΔT_{pp}	6.55 [K]
Length of the $PHEX$	L_{PHEX}	5.90 [m]
Length of the $SHEX$	L_{SHEX}	2.77 [m]
Pressure drop CH_4	Δp_{CH_4}	0.0139 [bar]
Pressure drop $Refr'$	$\Delta p_{refr'}$	0.0161 [bar]
Pressure drop $Refr$	Δp_{refr}	0.0124 [bar]
Pressure drop $Refr''$	$\Delta p_{refr''}$	0.0101 [bar]
Specific energy consumption excluding power absorbed by compression and pre-cooling of biomethane	En_1	0.477
First coefficient of performance	COP_1	0431
Second coefficient of performance	COP_2	0.282

3.1.2. A nitrogen-hydrogen heat exchanger for liquid hydrogen vaporisation

The pipe-in-pipe technology, in addition to enabling fluid liquefaction, can also be utilized for the opposite process—fluid vaporization—since heat exchange always involves one fluid releasing heat and another absorbing it. Consequently, studies in [42], [43] have proposed a heat exchanger designed for liquid hydrogen vaporization, supported by preliminary zero-dimensional thermodynamic calculations confirming the results in [41]. For detailed information on this vaporizer, please refer to the following chapter.

4. Towards Sustainable Aviation: An Innovative Hydrogen Fuel System

Hydrogen-based propulsion offers several pathways to more environmentally sound, next-generation aircraft [105], [106], [107], [108]. To that effect, several feasibility studies have suggested that a 50-90% reduction in flight emissions is possible in the next 10-15 years for aircraft leveraging hydrogen combustion or fuel cell technology compared to forecasts for kerosene-fuelled aircraft [109]. At present, the combustion route is a more practical option for a wider array of aircraft due to insufficient hydrogen fuel cell power densities [105],[109]. Aircraft powered by hydrogen combustion are also envisioned to have a large technology overlap with existing kerosene designs, which aids development and adoption of the technology in the short-term. Indeed, companies such as Moog, Eaton Aerospace, and Parker Aerospace, well established in the fluid power domain, are also extremely active in the emerging field of hydrogen fuel systems [110].

Generally, the fuel system encompasses fuel storage, transfer, distribution, and metering processes throughout all flight phases expected of the aircraft [111], [112], [113]. These functions are carried out by a network of interconnected fuel tanks, pumps, valves, and transfer lines, with the aim of providing desirable fuel conditions for combustion at the gas turbine aeroengine. At a high level, common architectures for a kerosene-fuelled system involve a series of boost pumps connected to a fuel storage tank, which deliver fuel to the inlet of a larger positive displacement pump referred to here as the main fuel pump. The main pump elevates the fuel to the correct pressure and transfers the fluid to a fuel metering unit (FMU) downstream [114], [115].

Before reaching the FMU, a heat exchanger (HEX) or series of HEXs, raise the temperature of the fuel to the ideal range for combustion [116]. The FMU then regulates the amount of fuel passing through to the engine to facilitate dynamic thrusting of the aircraft on demand [117]. Consequently, the fuel storage tank(s), pumps, HEX and FMU are central to responsive and accurate fuel delivery [118], [119]. Notably, while these high-level features can be retained for hydrogen aircraft, additional design challenges must be addressed.

Similar to the kerosene architecture, tank-mounted boost pumps will be relied on to initiate transfer of the LH_2 to the engines [120]. On the contrary, while positive displacement pumps are appropriate for kerosene handling, evidence suggests that they are not suitable for cryogenic LH_2 application. Deficiencies are linked to intensified thermal contraction and cycling, which have been shown to penalize the leakage performance in piston-type displacement pumps, shortening their operational life [121], [122]. Moreover, the pumps would be required to run at low rotational speed under these conditions giving poor power-to-weight ratio. Reports on vane-type configurations for LH_2 use have been equally unpromising [123]. The centrifugal pump is thus favoured in the literature as a substitute for the conventional positive displacement configuration [120].

The impact of heat exchangers on a hydrogen system also deviates from the baseline case. Reduced temperatures associated with LH_2 can be leveraged at the HEX for enhanced cooling of the components nearer to the engine [114], [115], but the low boiling point (i.e., 20 [K]) of hydrogen, results in a phase change to gaseous hydrogen (GH_2) at the HEX. This does not occur when dealing with kerosene fuels, so the heat exchangers can often be excluded from numerical kerosene-based analysis in favour of simplifying assumptions, e.g., constant density [124], [125]. Hydrogen architectures on the other hand must account for the gas compressibility downstream of the HEX.

Essential elements of a conventional FMU subassembly include the main fuel metering (FM) servovalve, and bypass valve [126]. The FM servovalve controls the explicit fuel volume (or mass) flowrate supplied to the engine, while the bypass valve enforces a linear relationship between the FM servovalve opening and the fuel flow rate by maintaining a constant pressure ratio across the FM servovalve [124], [125]. Despite its high-performance characteristics, the FM servovalve represents a significant source of energy dissipation within the system [127], [128], [129], [130], [131], [132]. Once exposed to GH_2, these components must now be resistant to adverse hydrogen permeation and embrittlement effects caused by ingress of hydrogen molecules into the physical fuel system components. From a modelling perspective, since assumptions of incompressibility no longer hold, the use of components like the bypass valve become significantly more challenging.

The literature supports that the dynamics within a hydrogen architecture are likely to differ significantly from the kerosene baseline despite their shared general features. Models describing these hydrogen systems are valuable for gaining insights into performance. This chapter introduces a novel hydrogen fuel system architecture comprising the entire fuel path from the storage tank to the aeroengine combustor. Design studies on hydrogen-powered aircraft have been identified as a suitable foundation for framing the numerical analysis. Comprehensive examples include [120] and [133]. The former describes the operating conditions for a large, 400-seat, aircraft with a 30,000 [lbs] (133 [kN]) thrust engine, and will be used here to size model components and a control system in Simulink. Firstly, the previously established kerosene fuel system layout is introduced, followed by a description of the derivative hydrogen architecture (Section 4.1.1). Then, the computational model created using the software Simulink by means of the libraries of Simscape Fluids is described and the simulation results of the novel architecture obtained via open-loop control are presented in Section 4.1.2.

4.1. An innovative Hydrogen Aircraft Fuel System Layout

In order to develop a new and innovative aircraft fuel system compatible with hydrogen fuel, an examination was conducted on a conventional aircraft fuel system designed for kerosene operation [124], [125]. The layout of this conventional system is depicted in **Figure 33**.

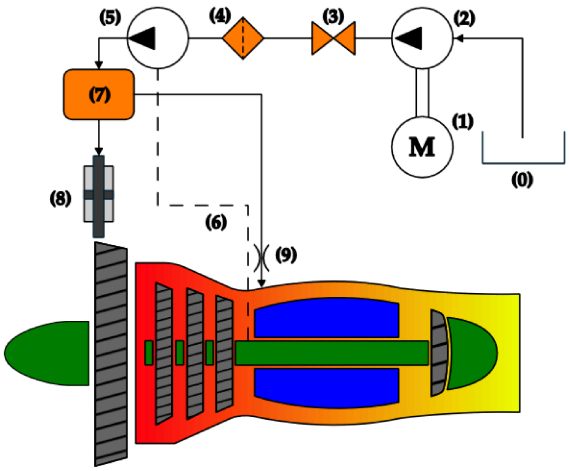

***Figure 33**. Kerosene based fuel system layout, adapted from [124], [125].*

.

In summary, the conventional gas turbine aircraft fuel system comprises several key components:

- The fuel tanks (0): These reservoirs store the necessary fuel for the entire flight and are typically located in the wings, fuselage, or tail;
- The boost pumps (2): Usually electrically driven (1) and of the centrifugal type, these pumps maintain a consistent fuel pressure (around 3 bar) in the fuel line between the tank and the main fuel pump;
- The shut-off valves (3): These components can shut off fuel flow to the engine if necessary, ensuring safety;
- The low-pressure filters (4): Essential for removing solid particles from the fuel flow, preventing damage to the main fuel pump;
- The main fuel pump (5): This is a positive displacement pump driven by the engine via the accessory gearbox (6). Its main function is to supply high-pressure fuel to the Fuel Metering Unit (FMU) for combustion and to act as hydraulic fluid for the compressor inlet guide vanes, providing a flow rate greater than that required by the engine;
- The Fuel Metering Unit (7): Represented within a schematic box, the FMU comprises the bypass valve, Inlet Guide Vane (IGV) servovalve, Fuel Metering (FM) servovalve, pressurizing valve, and engine shut-off valve. The FMU is the most important component of a conventional aircraft fuel system, as it controls the fuel flow rate to the combustion chamber and adjusts the angle position of the IGVs;
- The IGV Actuator (8): Mounted on the compressor casing, this actuator adjusts the position of the IGVs based on the fuel flow rate received from the IGV servovalve;
- The fuel nozzles (9): These nozzles inject fuel into the combustion chamber by vaporizing it, facilitating the combustion process.

Building upon this layout, the authors propose the following hydrogen-based fuel system layouts, depicted in **Figure 34**.

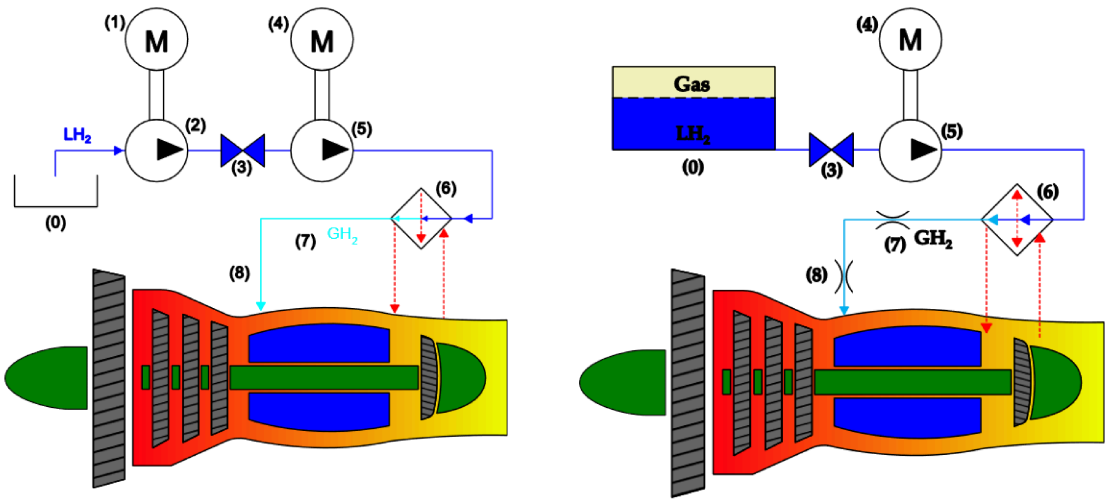

***Figure 34**. Hydrogen based fuel system layouts: **(a)** configuration with the use of boost pumps; **(b)** configuration with the use of slightly pressurized tanks.*

Transitioning from kerosene to hydrogen necessitates several adjustments due to the inherent differences between these two fuels. These adjustments are outlined below:

- The fuel tanks (0): The size of the fuel tanks needs to be modified to accommodate hydrogen, which can be stored either as a liquid or a gas. Cryogenic LH_2 storage offers advantages over compressed GH_2 storage. Firstly, it increases the density of hydrogen by 2 to 3 times. Secondly, it allows storage at a pressure close to atmospheric pressure. However, a notable drawback is that hydrogen boils at 20 [K] at atmospheric pressure, which has significant implications for boil-off regulation, tank venting, and insulation requirements;
- The boost pumps (2): Concerning the configuration of **Figure 34(a)**, centrifugal-type boost pumps can be preferred to positive displacement pumps for supplying LH_2 to the main fuel pump. These pumps have the responsibility of incrementally increasing both pressure and temperature, and then maintaining them to prevent two-phase flow in the fuel lines between the fuel tanks and the main fuel pump. As a result, the temperature of the LH_2 at the inlet of the main fuel pump exceeds the tank value due to heat inputs from the boost pumps and their submerged electric motors (1), as well as heat input along the fuel lines and the presence of shut-off valves (3) necessary for system safety. An alternative configuration, depicted in **Figure 34(b)**, addresses the need for incremental pressure increase using slightly pressurised fuel tanks. In this configuration, tank pressurisation is achieved by introducing inert gas into the tank, e.g. helium. Inert gas and liquid hydrogen must be at the same temperature. At this temperature, it is crucial that the inert gas must be already in a gaseous state. The progressive decrease in liquid hydrogen in the tank for combustion purposes allows the inert gas to expand. This expansion maintains the hydrogen at the correct interval pressure, ensuring its preservation in a liquid form;
- The main fuel pump (5): Considering the reported limitations of positive displacement pumps and the proven success of centrifugal-type pumps in LH_2 service, the decision is to opt for an electrically driven (4) centrifugal pump as the main fuel pump. This pump is tasked with delivering high-pressure LH_2 to fulfil the diverse requirements of the engine across different operating conditions, including startup, idle, takeoff, climb, cruise, and flight idle. The choice to drive the pump using an electric motor instead of the engine accessory gearbox offers control flexibility, allowing the pump's speed to be independently controlled regardless of the engine's speed;
- The heat exchanger (6): This component is crucial for ensuring the phase change of hydrogen from LH_2 to GH_2. The heat flow required for the hydrogen transition phase is provided by burnt gases. This marks a significant difference between kerosene and hydrogen fuel systems, as the latter requires a phase change from liquid to gas for the metering process;
- The metering valve (7): The metering process with GH_2 is conducted using a convergent-divergent nozzle, controlling the flow of GH_2 into the combustion chamber by adjusting the throat area. If sonic velocities are reached at a throat section, it may lead to choked flow or critical flow conditions, making the flow independent of downstream conditions;
- The injector nozzles (8): Although their purpose remains unchanged, namely, to inject fuel into the combustion chamber, the size of hydrogen nozzles differs from that of kerosene nozzles, requiring a wider area due to the gaseous nature of the fuel;

Another notable difference between kerosene and hydrogen fuel systems is that in the latter, it is not possible to use the fuel in an actuator to regulate the position of the IGVs. Therefore, an additional hydraulic circuit will be required to achieve the regulation of the IGVs.

4.1.1. Simulink Model

The novel aircraft fuel system was analysed and modelled within the Simulink environment, leveraging the Simscape libraries [134]. The simulation code, which reproduces the innovative fuel system layout, previously depicted in **Figure 34(b)**, comprises two interconnected Simscape networks. The first network, shown in **Figure 35(a)**, represents a two-phase system where the hydrogen fluid can exist in either liquid (LH_2) or gaseous (GH_2) states. In contrast, the second network, illustrated in **Figure 35(b)**, depicts a single-phase system where the hydrogen fluid remains solely in its gaseous (GH_2) state.

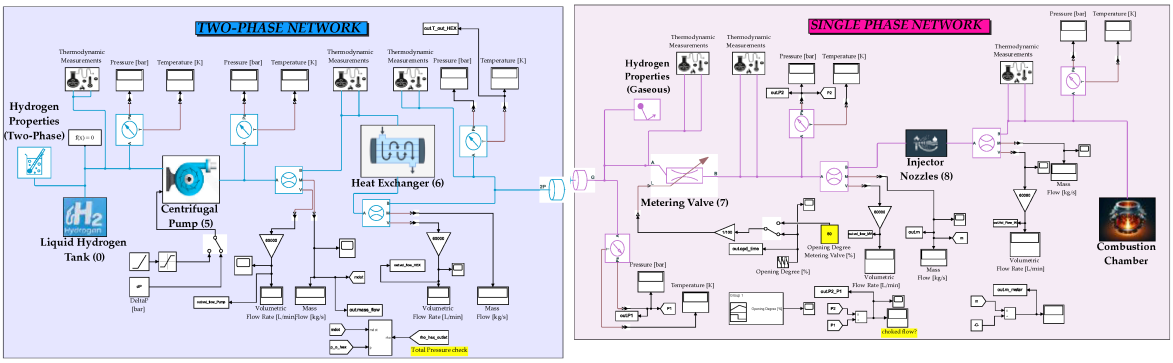

(a) **(b)**

Figure 35*. Simulink model reproducing the innovative aircraft fuel system proposed:* ***(a)*** *two-phase network;* ***(b)*** *single phase network.*

To specify the thermophysical properties of hydrogen (H_2) in the two-phase and gas networks, the "Two-Phase Fluid Properties (2P)" and "Gas Properties (G)" blocks were used, respectively. Leveraging the CoolProp libraries [135], the "Two-Phase Fluid Properties (2P)" block determines H_2 properties based on pressure and a normalized form of internal energy [134]. Specifically, the normalized internal energy, $\bar{u}$, is evaluated with one of the following equations, depending on the state of H_2: [134]:

1. Subcooled liquid state:

$$\bar{u} = \frac{u - u_{min}}{u_{sat}^{L}(p) - u_{min}} - 1, \qquad u_{\min} \le u < u_{sat}^{L}(p) \tag{45}$$

2. Superheated vapor state:

$$\bar{u} = \frac{u - u_{max}}{u_{max} - u_{sat}^{V}(p)} + 2, \qquad u_{sat}^{V}(p) < u \le u_{max} \tag{46}$$

3. Two-phase mixture:

$$\bar{u} = \frac{u - u_{sat}^{L}(p)}{u_{sat}^{V}(p) - u_{sat}^{L}(p)}, \qquad u_{sat}^{L}(p) \le u \le u_{sat}^{V}(p) \tag{47}$$

where:

- u is the specific internal energy of H_2;
- $u_{\min}$ and u_{max} are the lowest and highest specific internal energies allowed in the two-phase network;

- $u_{sat}^{L}(p)$ and $u_{sat}^{V}(p)$ are the specific internal energy of the liquid and vapor phase at saturation, respectively, considering a specific pressure (p).

  In particular, in the two-phase network, the values of specific internal energy range from $u_{min} = -53.952$ [kJ/kg] to $u_{max} = 15{,}000$ [kJ/kg]. The specific internal energies at saturation depend on pressure, which varies across a vector of 60 values from $p_{min} = 0.0074$ [MPa] to $p_{max} = 10$ [MPa]. This results in:

- $u_{sat}^{L}(p)$ ranging from -53.952 [kJ/kg] at p_{min} to 351.791 [kJ/kg] at p_{max};
- $u_{sat}^{V}(p)$ ranging from 343.219 [kJ/kg] at p_{min} to 351.791 [kJ/kg] at p_{max}.

On the other hand, regarding the "Gas Properties (G)" block, it offers a choice between three gas property models: perfect gas, semi-perfect gas, and real gas [134]. For higher accuracy, the real gas model was selected. Using this model, the thermophysical properties of H_2 in the gas network were determined once more by utilizing the CoolProp libraries, based on a specific range of pressure and temperature [135]. It is important to note that, in order to conserve fluid properties, the "Gas Properties (G)" block and the "Two-Phase Fluid Properties (2P)" block have the same settings.

The thermophysical properties of hydrogen (H_2), collected in the "Two-Phase Fluid Properties (2P)" and "Gas Properties (G)" blocks, can be visualized in **Figure 36** and **Figure 37**, respectively.

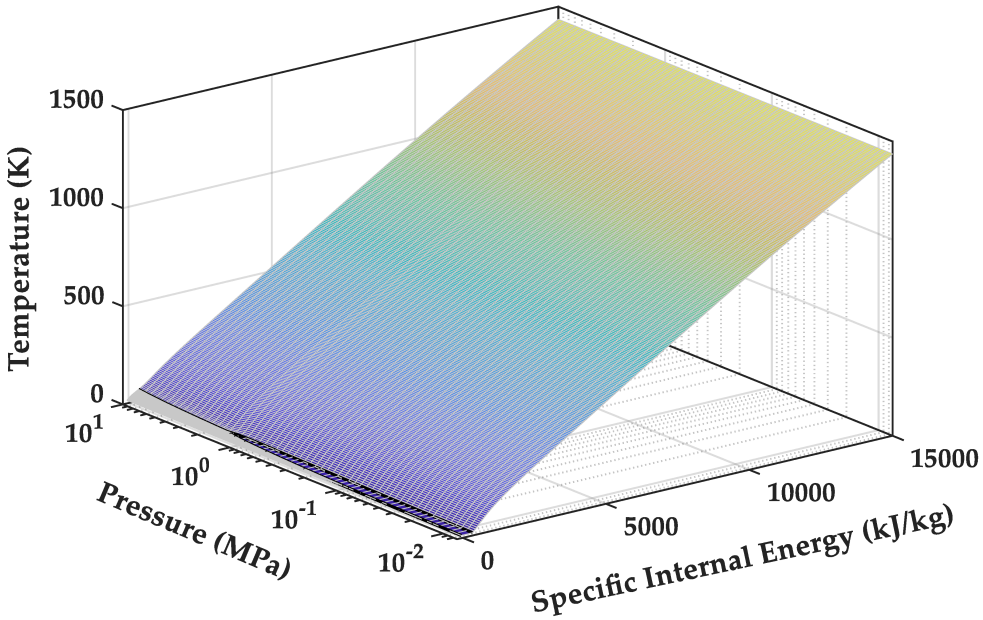

***Figure 36**. Specified H_2 properties as a function of pressure and specific internal energy for the connected two-phase network.*

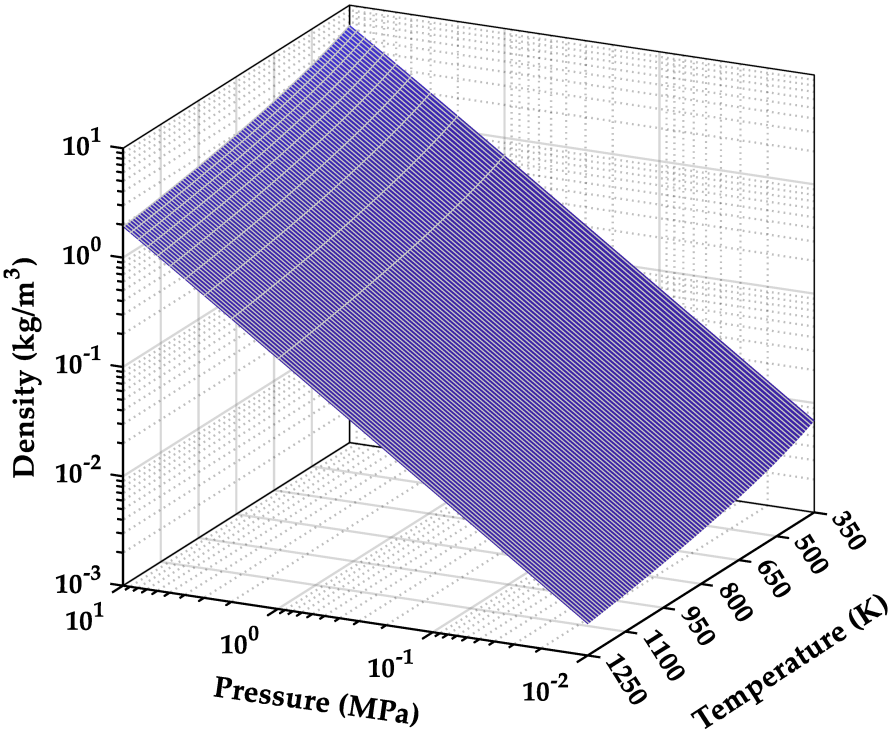

***Figure 37**. Specified H_2 properties as a function of pressure and temperature for the connected single phase (gas) network.*

4.1.1.1. Fuel Tanks

The configuration proposed in **Figure 34(b)** is analysed. Hydrogen is stored onboard as a liquid (LH_2) under cryogenic conditions, with low temperature and a pressure slightly higher than the atmospheric pressure due to the presence of the inert gas. According to [120], the LH_2 delivery to the main fuel pump inlet is specified to be at a condition of saturated liquid at 3.45 [bar], corresponding to a saturated temperature of around 25.2 [K].

In this initial analysis, the slightly pressurized fuel tanks (0) are represented in the model by the "Controlled Reservoir (2P)" block. This block enables the setting of boundary conditions in the two-phase network, reflecting the thermodynamic conditions of hydrogen at the inlet of the main fuel pump. Specifically, LH_2 exits the reservoir at the reservoir pressure (which corresponds to the pressure required at the inlet of the main fuel pump) and a specific internal energy, determined by setting the vapor quality (x) equal to zero to meet the saturated conditions required at the main fuel pump inlet. Vapor quality refers to the mass fraction of vapor in the liquid-vapor mixture.

Since the shut-off valves are not modelled in this preliminary study, the conditions need to be set in the block as $p^{TK} = 3.45$ [bar] and $x^{TK} = 0$, where the superscript "TK" denotes the quantities related to the fuel tanks (or to the inlet of the main fuel pump).

4.1.1.2 Main Fuel Pump

The main fuel pump, designed by Brewer [120], is a two-stage centrifugal system. At the design point, it achieves a mass flow rate $\dot{m} = 0.453$ [kg/s] and generates a pressure increase of approximately $\Delta p^{MP} = 48.1$ [bar] while rotating at $N^{MP} = 50{,}000$ [rpm]. It is important to note that the superscript "MP" denotes the quantities related to the main fuel pump. For

further details about the pump design, please refer to [120]. The performance map of this pump, illustrating the pressure increase as a function of mass flow rate and rotational speed, is depicted in **Figure 38**.

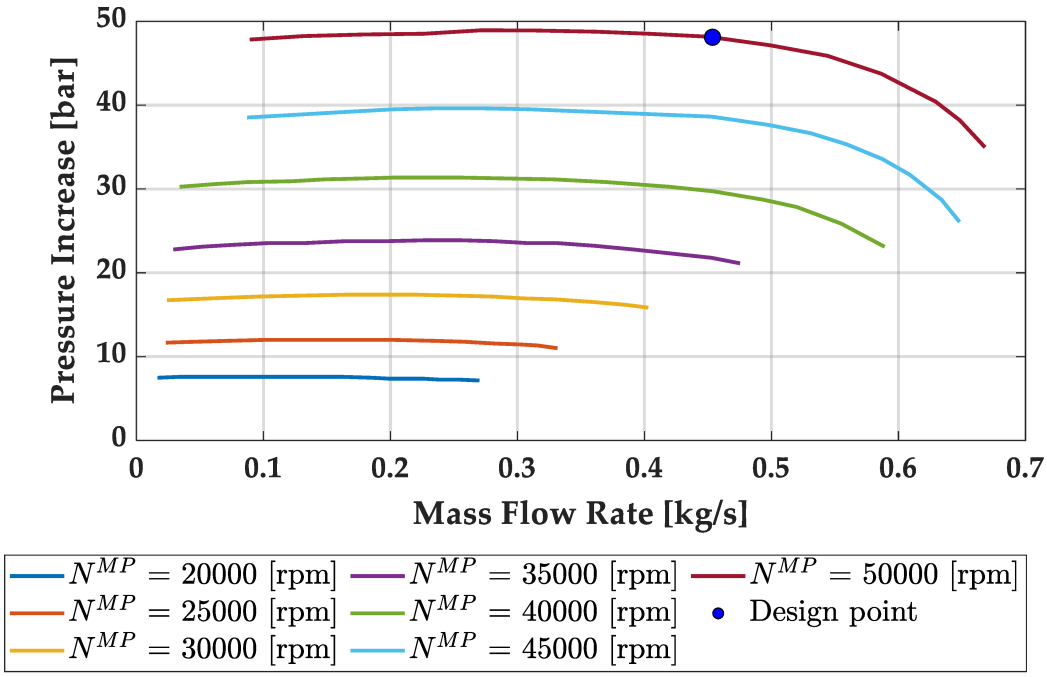

***Figure 38**. Main fuel pump performance map, adapted from [120].*

In this preliminary analysis, the main fuel pump is modelled solely based on its design curve, which operates at a rotational speed of N^{MP} = 50,000 [rpm]. Regarding the mass flow rate, the range considered spans from the lower limit up to the design point on the curve. It is worth noting that within this range, the curve exhibits an almost constant behaviour. Therefore, a simple "Pressure Source (2P)" block is used to represent the main fuel pump. This approach allows for the regulation of the pump's mass flow rate by adjusting the system characteristic while maintaining a constant pressure increase. Additionally, the modelling does not include the power absorbed by the pump or its efficiency. As a result, the pump is assumed to perform isentropic work on the incoming fluid, and thus, the specific entropy, "s", must have the same value at its inlet ("in") and at its outlet ("out"):

$$s_{in}^{MP}(p_{in}^{MP}, u_{in}^{MP}) = s_{out}^{MP}(p_{out}^{MP}, u_{out}^{MP}) \tag{48}$$

4.1.1.3. Heat Exchanger

The heat exchanger, where the transition phase of hydrogen occurs, is modelled with a pipe containing a two-phase fluid (represented by the "Pipe (2P)" block) and a controlled heat flow rate source. The heat flow rate source supplies a precise amount of energy to the pipe, enabling the phase transition of hydrogen from LH_2 to GH_2. This transformation is assumed to occur under isobaric conditions. Given that the temperature of hydrogen at the heat exchanger outlet is fixed (T_{out}^{HEX} = 353 [K], where the superscript "HEX" denotes quantities related to the heat exchanger), the transmitted thermal power to the pipe can be calculated. This calculation takes into account the time variation of the mass flow rate ($\dot{m}$) during the simulation, using the following equation:

$$\dot{Q}^{HEX} = \dot{m} \cdot (h_{out}^{HEX} - h_{in}^{HEX}) \tag{49}$$

where the hydrogen inlet and outlet enthalpies (h_{out}^{HEX} and h_{in}^{HEX}) are well determined, given the main fuel pump outlet conditions (see section 3.2) and the fixed temperature of hydrogen at the heat exchanger outlet.

Thermal power is then transferred convectively between the pipe wall and the internal fluid (hydrogen), as described by the following equation [134]:

$$\dot{Q}^{HEX} = h_{conv} \cdot S_p \cdot (T_w - T_f) \tag{50}$$

where S_p is the pipe surface area of the pipe, T_w is the pipe wall temperature, T_f is the fluid (hydrogen) temperature inside the pipe and h_{conv} is the convective heat transfer coefficient.

The calculation of the convective heat transfer coefficient depends on the hydrogen phase. In the subcooled liquid and superheated vapor phases, the coefficient can be determined by the following equation [134]:

$$h_{conv} = \frac{\overline{K}^* \cdot Nu^*}{D^{HEX}} \tag{51}$$

where $\overline{K}$, Nu represent the average thermal conductivity and average Nusselt number of the hydrogen inside the pipe, respectively, and D^{HEX} represents the hydraulic diameter of the pipe. It is important to note that the asterisk denotes a value specific to the hydrogen phase being considered in the pipe.

On the other hand, in a two-phase mixture, the convective heat transfer coefficient is evaluated as follows [134]:

$$h_{conv}^{M} = \frac{\overline{K}_{SL}^{M} \cdot Nu_{SL}^{M}}{D^{HEX}} \tag{52}$$

where the superscript M denotes a value specific to the two-phase mixture and the subscript SL indicates a value obtained for the saturated liquid.

In the liquid and vapor phases, the Nusselt number for turbulent flow can be calculated using the Gnielinski correlation [134]:

$$Nu^* = \frac{\frac{f}{8}(Re^* - 1000)\, Pr^*}{1 + 12.7\sqrt{\frac{f}{8}}\left(Pr^{*2/3} - 1\right)} \tag{53}$$

where Pr is the Prandtl Number and f represents the friction factor, which is given by [134]:

$$f = \left\{-1.8\log_{10}\left[\frac{6.9}{Re^*} + \left(\frac{\varepsilon^{HEX}}{3.7}\right)^{1.11}\right]\right\}^{-2} \tag{54}$$

where ε^{HEX} represents the roughness of the pipe internal surface and Re is the Reynolds number, which can be calculated using the following equation [134]:

$$Re^* = \frac{|\dot{m}| \cdot D^{HEX} \cdot v^*}{S \cdot k^*} \tag{55}$$

where v and k represent the specific volume and the kinematic viscosity of the hydrogen inside the pipe, respectively; whereas S is the cross-sectional area of the pipe.

On the other hand, in the two-phase mixture, the Nusselt number for turbulent flow can be determined using the Cavallini and Zecchin correlation [134]:

$$Nu^M = 0.05 \cdot \left[\left(1 - x - x \cdot \sqrt{\frac{v_{SV}}{v_{SL}}}\right) \cdot Re_{SL}\right]^{0.8} Pr_{SL}^{0.3} \tag{56}$$

where the subscript SV denotes a value for saturated vapor. The Reynolds number of the saturated liquid is calculated as follows [134]:

$$Re_{SL} = \frac{|\dot{m}| \cdot D^{HEX} \cdot v_{SL}}{S \cdot k_{SL}} \tag{57}$$

The modelled heat exchanger does not account for any transient phases, as they are not crucial for the aims of this preliminary study.

4.1.1.4. Metering Valve

In this preliminary analysis, the metering valve is modelled in a very simple way in order to simulate choked flow in the throat section. The main assumption is that the adiabatic index γ can be considered equal to 1.4, even though the gas network is modelled with real gas. This is because within the range of pressures and temperatures considered, the value of the adiabatic index, γ, typically remains around 1.4. A practical demonstration of this concept is provided in **Figure 39**.

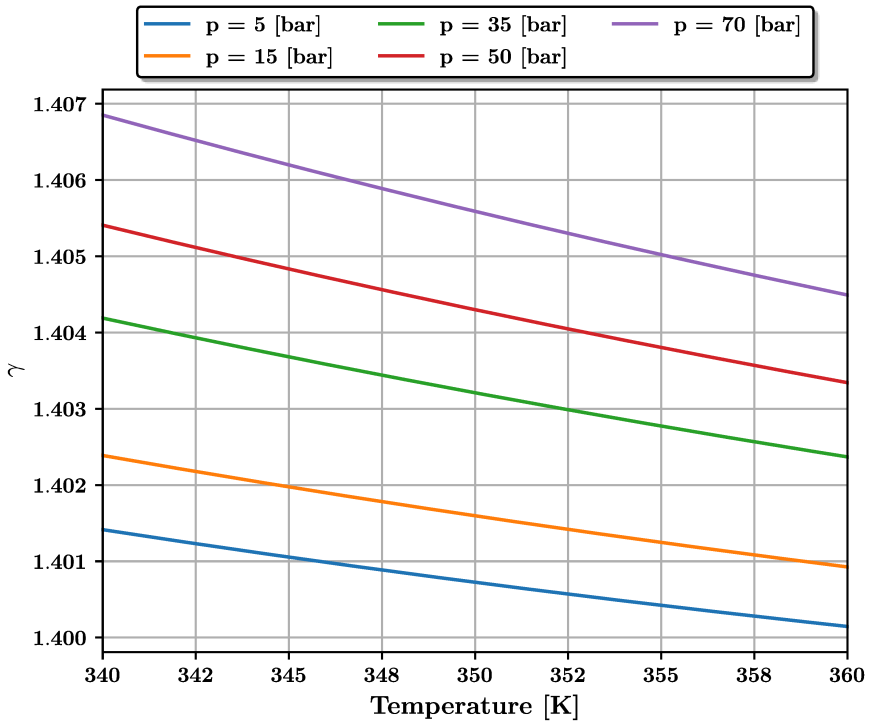

Figure 39. *Invariance of the adiabatic index for the working range of pressures and temperatures.*

Since the Simscape library does not include a block that replicates a convergent-divergent nozzle, the "Orifice (G)" block has been used to approximate the behaviour of the metering valve. This block employs gas dynamics equations for compressible flows, allowing the system to reach sonic conditions in the restriction section. However, it is crucial to understand that this block only simulates an orifice, which can be used to reproduce the convergent part of a nozzle. Consequently, due to the lack of the divergent section, the thermodynamic conditions at the block's exit correspond to those at the nozzle's throat, preventing the simulation of supersonic conditions.

The mass flow rate passing through the metering valve can be calculated, in the most general case, as a function of the pressure ratio, as shown in the following equation [134], [136]:

$$\dot{m} = C_d^{MV} A_r^{MV} \sqrt{\frac{2\gamma}{\gamma-1} p_{in}^{MV} \cdot \rho_{in}^{MV} \left(\frac{p_{out}^{MV}}{p_{in}^{MV}}\right)^{\frac{2}{\gamma}} \left[\frac{1-\left(\frac{p_{out}^{MV}}{p_{in}^{MV}}\right)^{\frac{\gamma-1}{\gamma}}}{1-\left(\frac{A_r^{MV}}{A^{MV}}\right)^2 \left(\frac{p_{out}^{MV}}{p_{in}^{MV}}\right)^{\frac{2}{\gamma}}}\right]} \tag{58}$$

where C_d, A_r, A represent the discharge coefficient, the restricted area and the area at the inlet section of the metering valve; whereas ρ is inlet density of the hydrogen. It is important to note that the superscript *"MV"* denotes the quantities related to the metering valve. Additionally, it is important to observe that in equation (14), p_{in}^{MV} denotes the static pressure at the inlet of the metering valve, not the total pressure p_0. The latter can be evaluated by the following equation:

$$p_0 = p_{in}^{MV} + \frac{1}{2}\rho_{in}^{MV}(c_{in}^{MV})^2 \tag{59}$$

where c_{in}^{MV} represents the absolute velocity of the GH_2 flow at the inlet of the metering valve. This assumption, considering the static pressure instead of the total pressure, is valid because the difference between the static and total pressure is negligible. A practical demonstration of this will be provided in Section 4, which covers the simulation results.
When critical conditions are reached, the pressure ratio drops below the threshold value of $\frac{p_{out}^{MV}}{p_{in}^{MV}} = \left(\frac{2}{\gamma+1}\right)^{\frac{\gamma}{\gamma-1}} = 0.5283,$ indicating choked conditions in the throat section. As a result, the mass flow rate reaches its maximum value and becomes independent of the downstream pressure. The mass flow rate in this specific case can be modelled by the following equation [134], [136]:

$$\dot{m} = C_d^{MV} A_r^{MV} \sqrt{\frac{2\gamma}{\gamma-1} p_{in}^{MV} \cdot \rho_{in}^{MV} \cdot \frac{1}{\left(\frac{\gamma+1}{2}\right)^{\frac{2}{\gamma-1}} - \left(\frac{A_r^{MV}}{A^{MV}}\right)^2}} \tag{60}$$

Equations (59) and (60) used by the Simscape "Orifice (G)" block are slightly different from those commonly found in gas dynamics literature. However, the authors compared the results from the literature and the Simscape equations and found that the error when using the Simscape equations is approximately in the range of ±1%.

4.1.1.5. Injector Nozzles

To model the injector nozzles, the same Simulink block previously described in section 3.4 has been adopted. The aim of the injector nozzles is to inject the fuel in the combustion chamber, producing a pressure drop with respect to the upstream conditions. In accordance with the conditions outlined in the literature [120], the total injecting area has been set to $A_{TOT}^{IN} = 380$ [mm^2]. This value can be distributed among 20 different nozzles used for injecting fuel into the combustion chamber. Thus, the injecting area for each individual nozzle is $A^{IN} = 19$ [mm^2], corresponding to a single nozzle diameter of approximately $D^{IN} \approx 5$ [mm].

4.1.1.6. Combustion Chamber

The combustion chamber is modelled using a “Controlled Reservoir (G)” block. This block sets controlled boundary conditions in a gas network. Specifically, GH_2 enters the reservoir at the reservoir specified pressure (p^{cc}), but its temperature (T^{cc}) is determined by the gas network upstream conditions. Note that the superscript "cc" denotes the quantities related to the combustion chamber.

4.1.2. Simulation Results

In this section, the numerical results of the simulations are discussed. To validate the numerical model, the operating conditions simulated here are compared with those reported in the literature [120], particularly concerning the takeoff phase. **Table 15** offers a concise summary of all the fuel system conditions related to the most demanding scenario in terms of fuel flow rate required in the combustion chamber, specifically during takeoff. In **Table 15**, Δp^{HEX} and Δp^{MV+IN} represent the pressure drops due to the heat exchanger and metering valve plus injector nozzles, respectively.

***Table 15**. Takeoff conditions reported in [120].*

$\dot{m}$	N^{MP}	Δp^{MP}	Δp^{HEX}	Δp^{MV+IN}	p^{cc}
[kg/s]	[rpm]	[bar]	[bar]	[bar]	[bar]
0.411	50,000	48.1	5	10.34	36.06

Table 15 and **Table 16** show the input parameters of the simulations and the controlled output variables, respectively. It is important to note that two different simulations were conducted. The first simulation aimed to demonstrate the metering valve choking conditions by decreasing in a linear way the combustion chamber pressure. On the other hand, the second simulation focused on accurately describing the behaviour of the fuel system by adjusting the metering valve's restricted area (or metering valve's opening degree (X^{MV})). To maintain consistency across both simulations, **Table 16** and **Table 17** present the nomenclature for all input parameters and output variables. Furthermore, **Table 18** displays the changing input parameters and their respective values in the two simulations.

***Table 16**. Simulated input parameters and corresponding nomenclature.*

Component	Input parameter (symbol)	Value	Unit
Fuel Tanks (0)	Vapour quality (x^{TK})	0	[-]
	Pressure (p^{TK})	3.45	[bar]
Main Fuel Pump (5)	Pressure increase (Δp^{MP})	48.1	[bar]
	Rotational Speed (N^{MP})	50,000	[rpm]
Heat Exchanger (6)	Tubes total length (L^{HEX})	2	[m]
	Tubes diameter (D^{HEX})	5	[cm]
	Outlet temperature (T_{out}^{HEX})	353	[K]
	Tubes roughness (ε^{HEX})	$1.5 \cdot 10^{-4}$	[μm]
Metering Valve (7)	Max. restricted area ($A_{r,max}^{MV}$)	300	[mm^2]
	Inlet area (A^{MV})	1257	[mm^2]
	Discharge Coefficient (C_D^{MV})	0.7	[-]
Injector Nozzles (8)	Restricted area (A_{TOT}^{IN})	380	[mm^2]

***Table 17**. Simulations' output variables and corresponding nomenclature.*

Component	Output variables	Symbols
Main Fuel Pump (5)	In. thermod. properties	$u_{in}^{MP}, h_{in}^{MP}, s_{in}^{MP}, \rho_{in}^{MP}$
	Out. thermod. properties	$u_{out}^{MP}, h_{out}^{MP}, s_{out}^{MP}, \rho_{out}^{MP}$
	Out. temperature	T_{out}^{MP}
	Out. pressure	p_{out}^{MP}
Heat Exchanger (6)	In. temperature	T_{in}^{HEX}
	In. – Out. pressure	$p_{in}^{HEX} - p_{out}^{HEX}$
	In. thermod. properties	$u_{in}^{HEX}, h_{in}^{HEX}, s_{in}^{HEX}, \rho_{in}^{HEX}$
	Out. thermod. properties	$u_{out}^{HEX}, h_{out}^{HEX}, s_{out}^{HEX}, \rho_{out}^{HEX}$
	Thermal power	$\dot{Q}^{HEX}$
Metering Valve (7)	Out. temperature	T_{out}^{MV}
	In. – Out. pressure	$p_{in}^{MV} - p_{out}^{MV}$
	In. thermod. properties	$h_{in}^{MV}, s_{in}^{MV}, \rho_{in}^{MV}$
	Out. thermo. Properties	$h_{out}^{MV}, s_{out}^{MV}, \rho_{out}^{MV}$
	In. Velocity	c_{in}^{MV}
Injector Nozzles (8)	In. – Out. temperature	$T_{in}^{IN} - T_{out}^{IN}$
	In. – Out. pressure	$p_{in}^{IN} - p_{out}^{IN}$
	In. thermod. properties	$h_{in}^{IN}, s_{in}^{IN}, \rho_{in}^{IN}$
	Out. thermod. properties	$h_{out}^{IN}, s_{out}^{IN}, \rho_{out}^{IN}$
System	Mass Flow Rate	$\dot{m}$
	Total Pressure	p_0

In addition to pressure (p) and temperature (T), other thermodynamic properties can be evaluated at the inlet (*in*) and outlet (*out*) of each component from the simulation results. These properties include entropy (s), enthalpy (h), density (ρ), and internal energy (u), as detailed in **Table 17**.

***Table 18.** Changing input parameters from the first to the second simulation.*

Simulation	X^{MV} [%]	p^{cc} [bar]
I	60	50÷15
II	30 – 50 – 80	Output Variable

Open-loop simulations are considered sufficient for a preliminary investigation into the hydrogen fuel system model. The first simulation aims to profile the system dynamics and investigate the choking conditions of the metering valve. Pressure within the combustion chamber decreased linearly from 50 bar to 15 bar, as depicted in **Figure 40**. The opening degree of the metering valve was set at 60%.

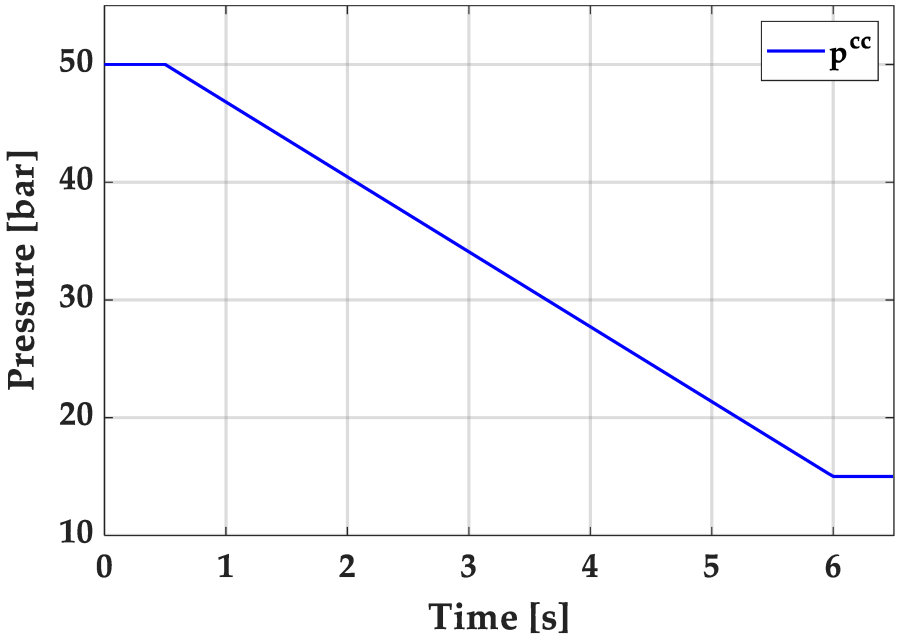

Figure 40. *Linear decreasing of the combustion chamber pressure.*

In equation (58), the static pressure at the inlet of the metering valve (p_{in}^{MV}) is used instead of the total pressure (p_0) because the difference between them is negligible, as illustrated in **Figure 41**.

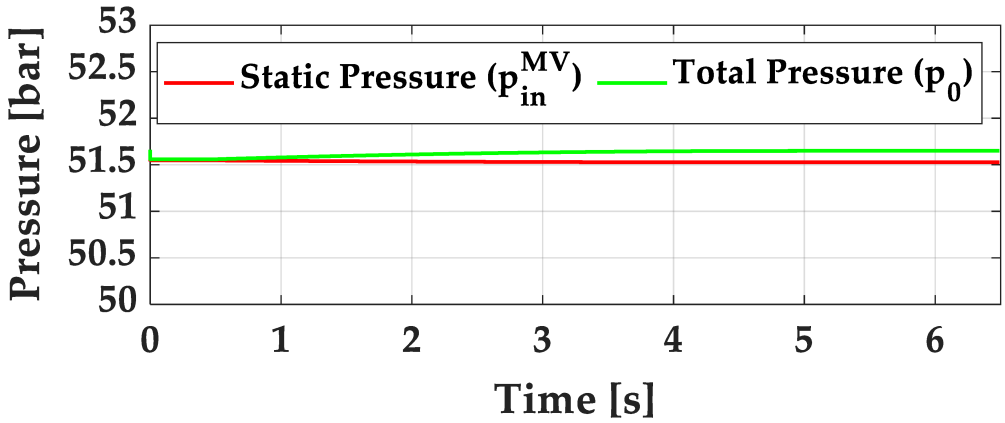

Figure 41*. Practical demonstration of the negligible deviation between total pressure and static pressure at the inlet of the metering valve for the first simulation.*

Figure 42 shows that the main fuel pump supplies LH_2 at a pressure of $p_{out}^{MP} = p_{in}^{HEX} = 51.55$ [bar]. Since the LH_2 to GH_2 transition in the heat exchanger occurs at constant pressure, $p_{in}^{HEX} = p_{out}^{HEX} = p_{in}^{MV}$, as the pressure in the combustion chamber decreases linearly, the pressure at the metering valve outlet or injector nozzles inlet (p_{out}^{MV} or p_{in}^{IN}) also decreases. Once the pressure ratio across the metering valve reaches the critical pressure ratio of $\frac{p_{out}^{MV}}{p_{in}^{MV}} = 0.5283$, the flow through it reaches maximum velocity conditions in the restricted section, resulting in choked flow. Consequently, further reduction in p_{out}^{MV} will not increase the mass flow rate.

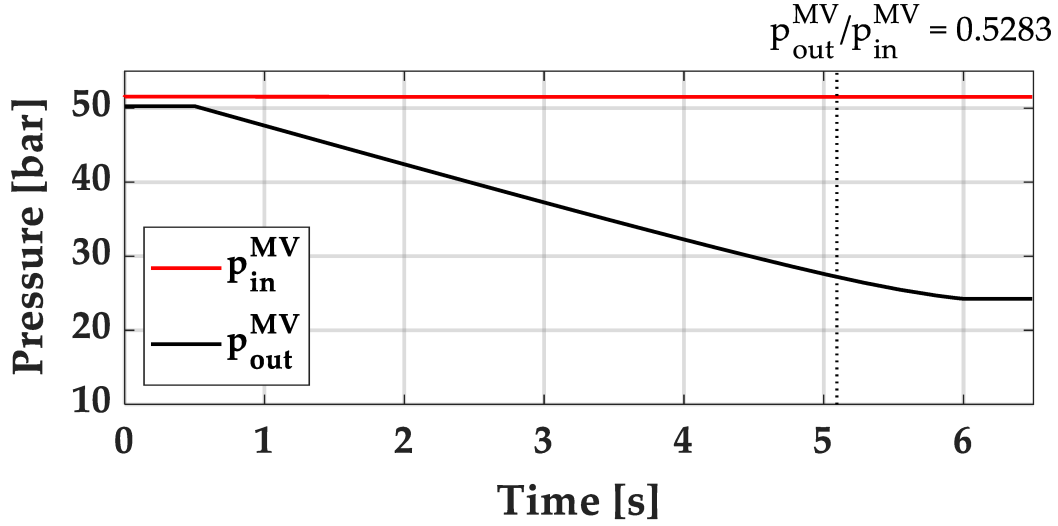

***Figure 42**. Upstream and downstream pressures for the metering valve under choking verification test conditions.*

Inspection of the mass flow through the metering valve in **Figure 43** confirms the expected behaviour. Initially, the pressure ratio across the valve is constant, resulting in a constant 0.11 [kg/s] mass flow rate through the orifice. As the downstream pressure drops, the mass flow rate increases up to the choke point at $\frac{p_{out}^{MV}}{p_{in}^{MV}} = 0.5283$, after which a mass flow rate of 0.38 [kg/s] is maintained constant despite further reductions of p_{out}^{MV}. Notably, while the difference between the valve upstream and downstream pressures is linear, the mass flow response is nonlinear and asymptotic as the pressure ratio approaches the choke point. This implies that mass flow sensitivity is reduced as the pressure ratio moves toward the critical value of 0.5283. A more explicit relationship between the mass flow rate and the metering valve pressure ratio is provided in **Figure 44**.

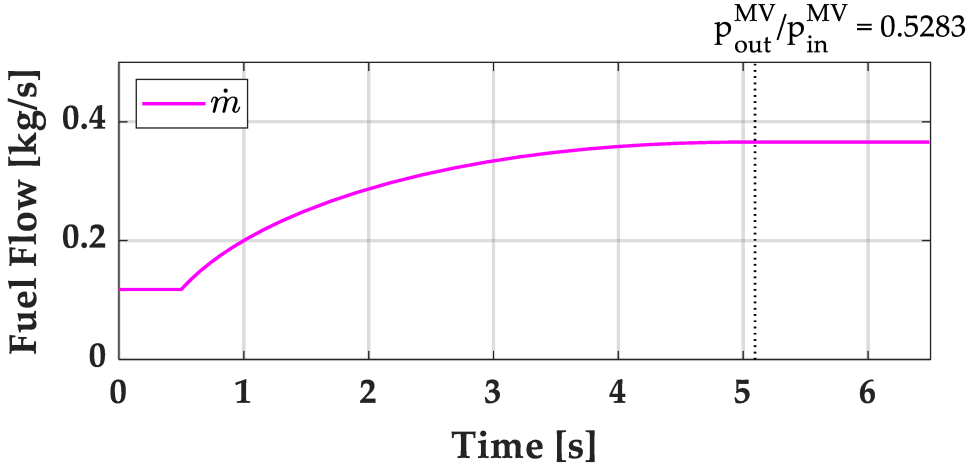

***Figure 43**. Metering orifice mass flow rate under choking verifcation test conditions.*

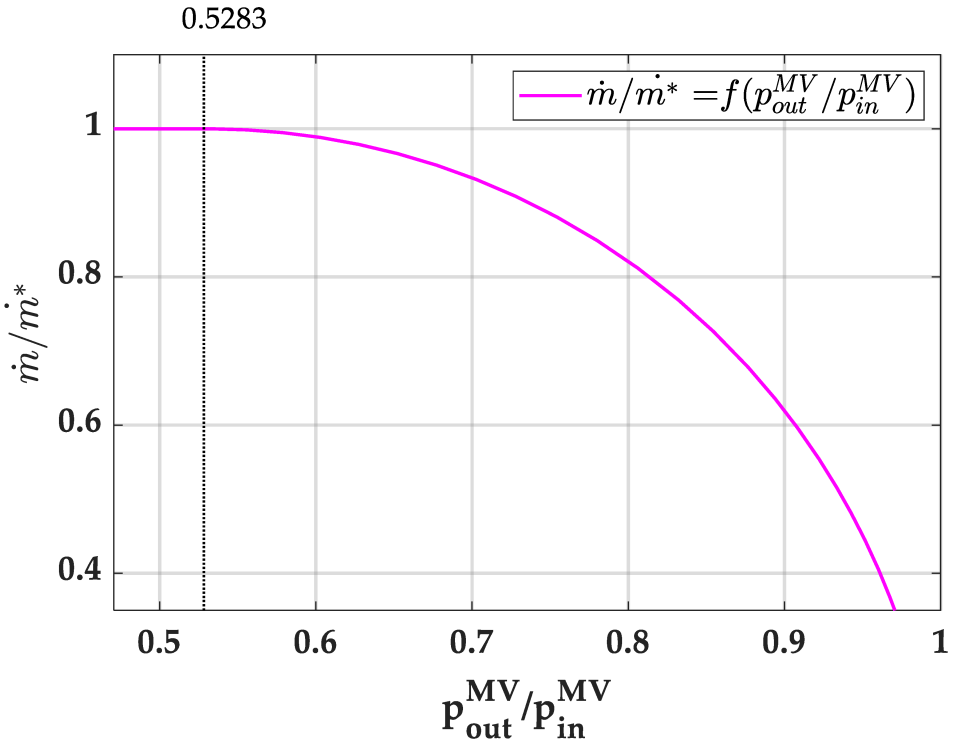

Figure 44. *Normalised mass flow rate vs metering valve pressure ratio.*

Considering **Figure 44**, the mass flow rate, $\dot{m}$, is normalized by its maximum value, $\dot{m}^*$, to confine the mass flow behaviour in a range between 0 and 1. Given that the pressure difference across the valve is responsible for driving the flow, a pressure ratio of 1 corresponds to stagnant flow, i.e., $\dot{m} = 0$. The choked gas condition at the orifice is also clearly visible at $\frac{p_{out}^{MV}}{p_{in}^{MV}} = 0.5283$, such that $\dot{m}$ converges to $\dot{m}^*$.

The heat exchanger used in the model is designed to maintain a constant GH_2 temperature equal to $T_{out}^{HEX} = 353$ [K]. This temperature target approximates values envisioned by the authors for a fuel system of this type. For effective temperature control, the heat addition must be proportional to the mass flow rate across the delivery line. This is demonstrated in **Figure 45** for the same aforementioned choking test conditions. The asymptotic mass flow behaviour is immediately visible in the heat exchanger thermal power response.

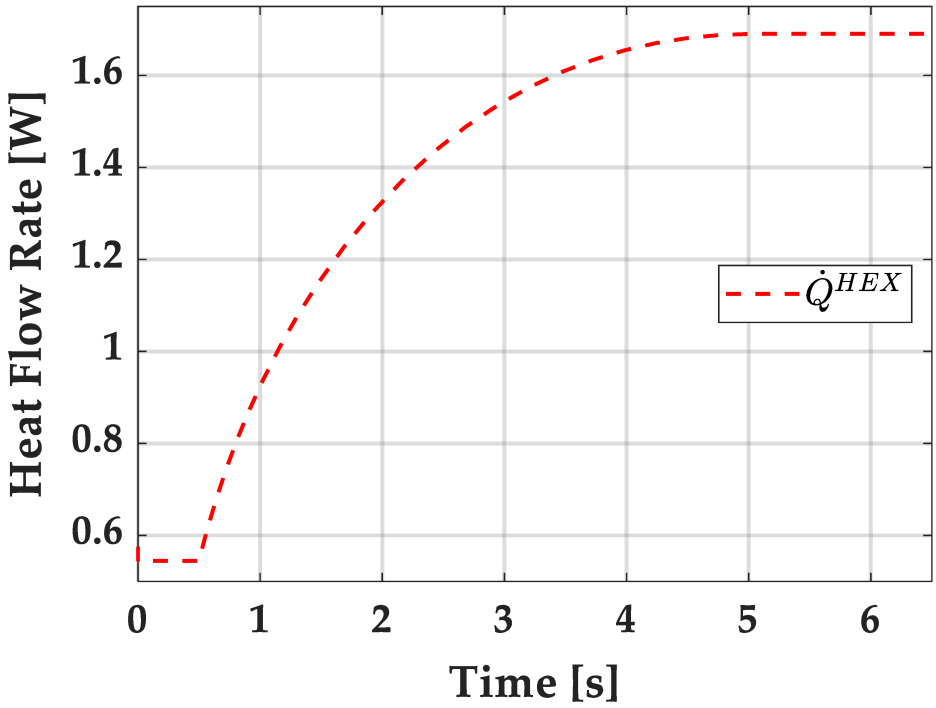

***Figure 45**. Thermal power required at the heat exchanger to maintain 353k gh2 temperature under choking test conditions.*

Internal thermodynamic properties at the heat exchanger are summarized in **Figure 46**. The characteristics of hydrogen across the heat exchanger block, monitored at the pump's operating pressure, include density, temperature, and entropy at both the inlet and outlet of the heat exchanger.

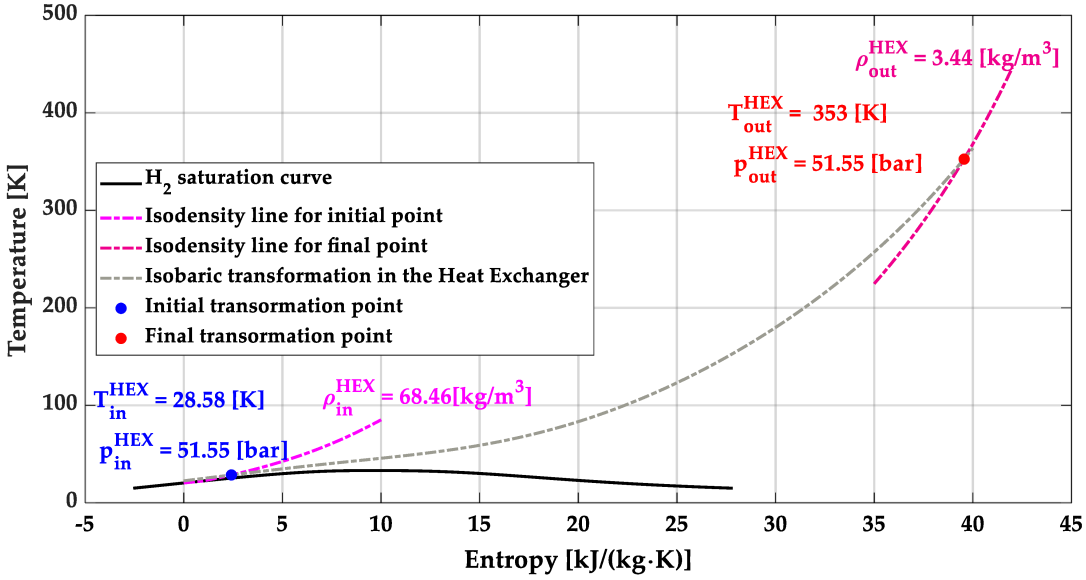

***Figure 46.** Thermodynamic properties at the hex inlet and outlet.*

The heat exchanger receives LH_2 at roughly $T_{out}^{MP} = T_{in}^{HEX} = 28$ [K] at the inlet and raises its temperature to the desired $T_{out}^{HEX} = T_{in}^{MV} = 353$ [K] in an isobaric process maintaining the prescribed $p_{out}^{MP} = p_{in}^{HEX} = p_{out}^{HEX} = 51.55$ [bar] pressure. In doing so, the density of the hydrogen drops from $\rho_{out}^{MP} = \rho_{in}^{HEX} = 68.95$ [kg/m^3] to $\rho_{out}^{HEX} = \rho_{in}^{MV} = 3.44$ [kg/m^3] with a large increase in entropy. This is within expectations for a phase change from LH_2 to GH_2.

To validate the model under takeoff conditions, the analysis now focuses simulating the behaviour of the fuel system for three specific metering valve opening degrees: 30%, 50%, and 80%, as illustrated in **Figure 47**.

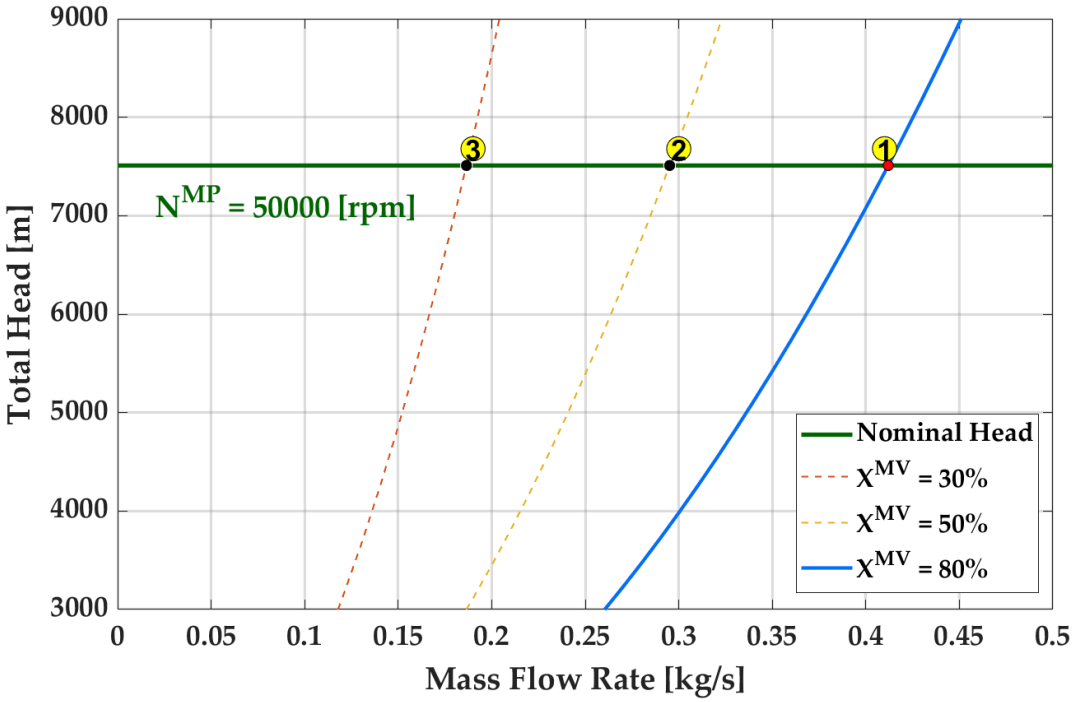

***Figure 47**. System and pump characteristic for three different metering valve opening degree: (1) $x^{MV} = 80\%$ working point; (2) $x^{MV} = 50\%$ working point; (3) $x^{MV} = 30\%$ working point.*

Brewer's analysis [120] of pump characteristics suggests that the pump design curve can achieve a suitable range of flow rates up to the design take-off condition. This curve corresponds to a nominal pump head of $H_u^{MP} = \frac{\Delta p^{MP}}{\rho_{in}^{MP} \cdot g} = 7509$ [m] (where g represents the gravitational acceleration) and a rotational speed N^{MP}=50,000 [rpm]. As described earlier, the main fuel pump is modelled to operate exclusively on its design curve in order to meet the takeoff condition and validate the model. From the lower limit to the design point on the curve, the behaviour remains relatively constant. This allows for flow rate regulation by adjusting the system characteristic through the metering valve opening degree. Despite changes in flow rate, a constant pressure increase is maintained.

The mass flow rate response at the metering orifice is verified with respect to a dynamic valve opening sequence as depicted in **Figure 48**. It is important to note that the takeoff conditions specified in [120] are achieved with a metering valve opening degree of $X^{MV} = 80\%$, corresponding to the first working point.

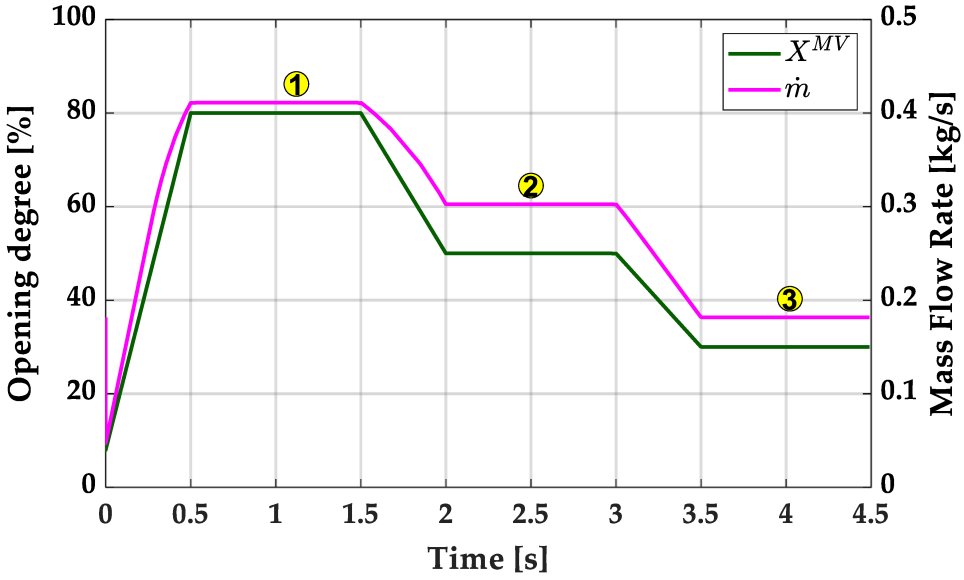

***Figure 48**. Mass flow rate response to dynamic valve opening profile.*

By analysing **Figure 48**, it is evident that initially, the valve is slightly opened. Over 0.5 seconds, the opening degree gradually increases to 80% and stays constant for 1.0 second. Following this, in the next 0.5 seconds, the opening degree decreases to 50% and remains at this level for 1.0 second. Finally, within the subsequent 0.5 seconds, the opening degree decreases further to 30% and maintains this value for 1.0 second. It is important to note that the adaptation of the mass flow rate to the metering valve opening degree is both rapid and reliable. In this second simulation, a linear characteristic proportional to the mass flow rate is employed to assess the pressure in the combustion chamber. As a result, when the opening degree of the metering valve increases, the flow rate to the combustion chamber also increases, resulting in higher combustion chamber pressure values. The trend of combustion chamber pressure is illustrated in **Figure 49**.

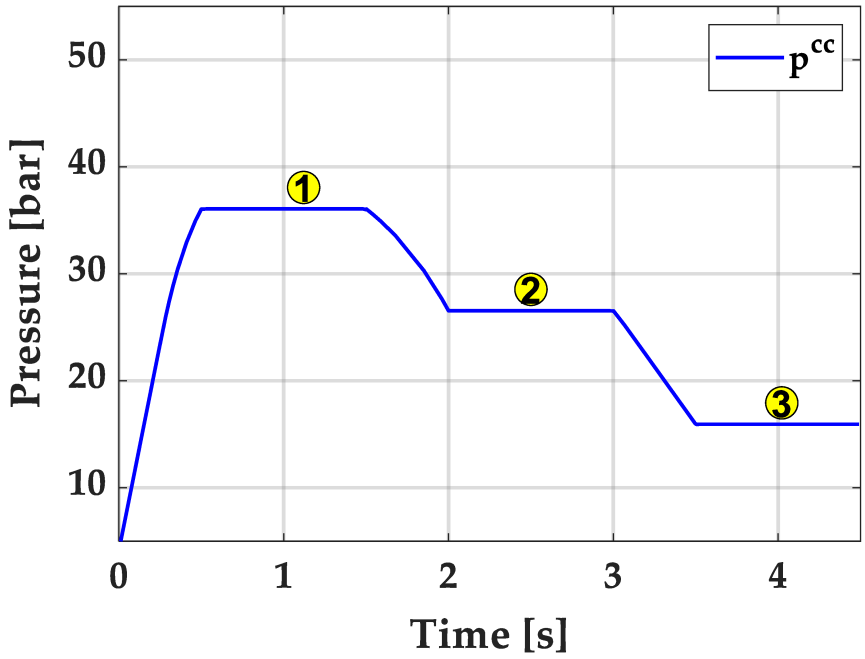

***Figure 49.** Combustion chamber pressure response to dynamic valve opening profile.*

Once again, **Figure 50** highlights the negligible difference between the static pressure at the inlet of the metering valve (p_{in}^{MV}) and the total pressure (p_0) for this second simulation, validating the previous assumption made in equation 58.

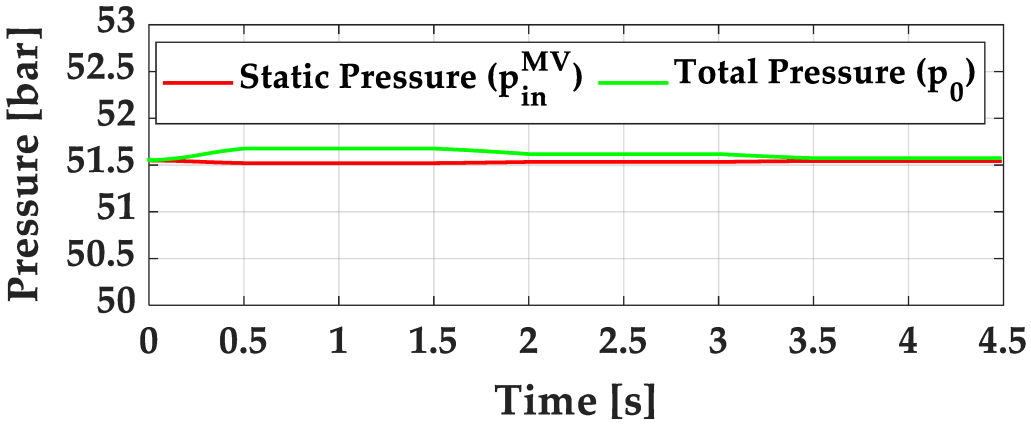

Figure 50. *Practical demonstration of the negligible deviation between total pressure and static pressure at the inlet of the metering valve for the second simulation.*

The pressure ratio trend for the metering valve is illustrated in **Figure 51**. Opening the valve to 80% results in a sharp increase in the pressure ratio, reaching up to 0.8. This occurs because the higher the opening degree, the higher the combustion chamber pressure, and consequently, the pressure downstream of the metering valve. Subsequent closure of the valve reduces the mass flow rate to the engine, thereby affecting the pressure ratio equilibrium. It's worth noting that once the valve opening decreases to 30%, the pressure ratio falls below $\frac{p_{out}^{MV}}{p_{in}^{MV}} = 0.5283$, indicating that under such conditions, flow through the orifice becomes choked.

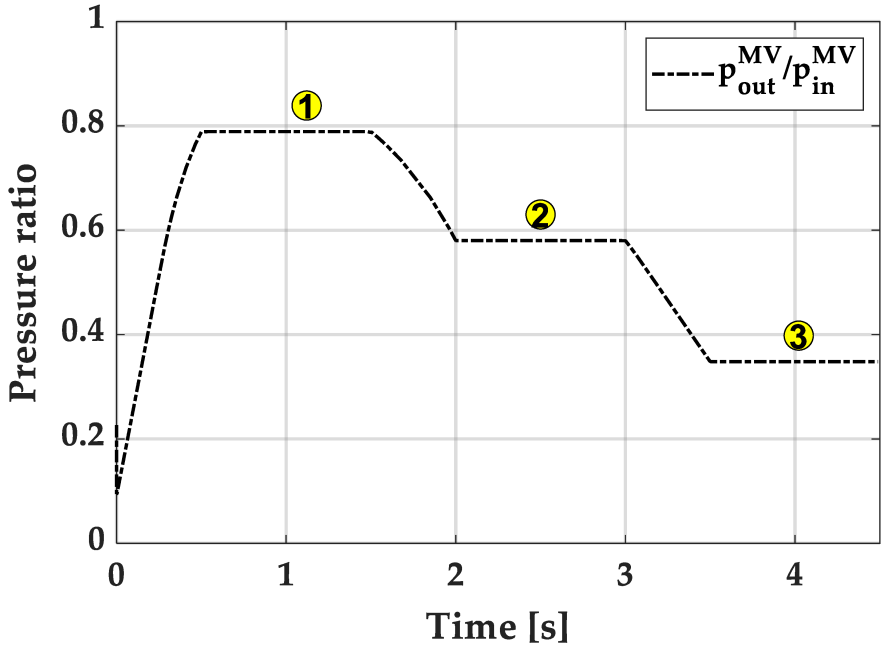

Figure 51*. Metering valve pressure ratio trend to dynamic valve opening profile.*

In conclusion, **Figure 52** and **Figure 53** depict the mass flow rate and density at the outlet of the main fuel pump and metering valve, respectively, for this second simulation.

Specifically, **Figure 52** demonstrates that the density of the liquid phase of hydrogen at the pump outlet remains constant at $\rho_{out}^{MP} = 68.95$ [kg/m^3], regardless of changes in the metering valve opening degree and the resulting variations in the mass flow rate needed for the combustion process. On the other hand, **Figure 53** highlights that due to the gas phase of hydrogen at the metering valve outlet, the density ρ_{out}^{MV} is not constant during changes in the metering valve opening degree and it is significantly lower than ρ_{out}^{MP}.

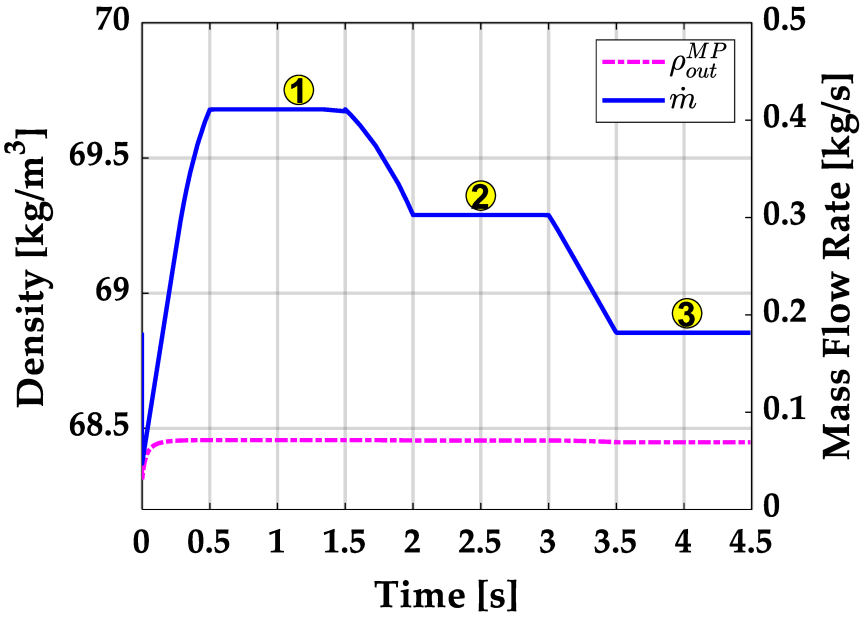

***Figure 52**. Main fuel pump outlet density and mass flow rate profile during the second simulation.*

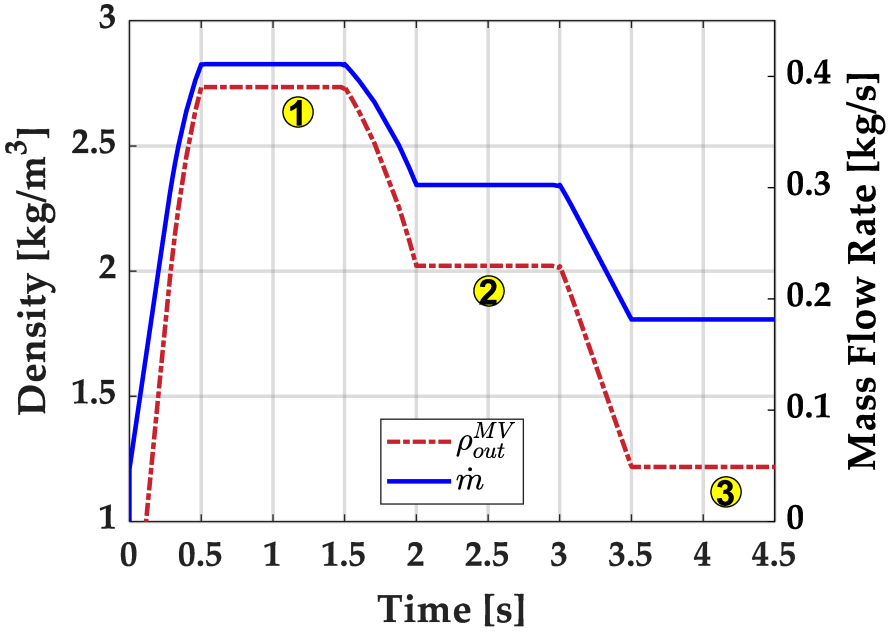

***Figure 53**. Metering valve outlet density and mass flow rate profile during the second simulation.*

In this study, a potential fuel system architecture for hydrogen-powered aircraft was investigated and compared to a previously established kerosene architecture based on the General Electric CJ610 fuel system. Focus was placed on the simulation of the entire fuel system extending from the fuel storage tank to the engine injectors, found to be lacking in the current literature.

The numerical results demonstrated that choked flow could be accurately modelled, with the mass flow rate remaining independent of downstream conditions. The simulations produced realistic outcomes, which were validated by comparing them under takeoff conditions with previous comprehensive studies reported in the literature. Additionally, the model proved robust to variations such as the metering valve's opening degree and the combustion chamber pressure.

Further research will aim at more detailed modelling of both the fuel system components and the control scheme. Specifically, the development of a new Simscape block that accurately replicates a convergent-divergent nozzle is planned, which will simulate the real behaviour of the metering valve, including the presence of supersonic flow and shock waves in the divergent section. Additionally, simulating this novel metering valve under closed-loop conditions will provide better insights into the geometric and functional improvements needed for hydrogen fuel systems.

4.2. A Possible Layout Of The Heat Exchanger In The Hydrogen Fuel System

Cryogenic LH_2 storage is the most viable solution for aviation, offering significant advantages over compressed GH_2 storage. Firstly, LH_2 can be stored at pressures close to atmospheric levels, eliminating the need for high-pressure tanks. Additionally, LH_2 enhances hydrogen's density by 2 to 3 times over GH_2. Despite this increase, LH_2 remains approximately 11 times less dense than kerosene. Consequently, although LH_2 has a specific energy nearly 3 times greater than kerosene, LH_2 tanks need about 4 times the volumetric capacity to store the same amount of energy. The main challenge with LH_2 is maintaining its cryogenic temperature, as it boils at 20 K under atmospheric pressure. This necessitates boil-off management, tank venting, and extensive insulation [137], [138]. However, the cryogenic temperature and high specific heat capacity of LH_2 also make it an excellent coolant, offering potential use as a heat sink for components close to the engine [139], [140], [141].

According to the ZEROe project of Airbus, using LH_2 as fuel for modified gas turbine engines, along with hydrogen fuel cells for generating electrical power, is considered the right green solution for next-generation aircraft [142].

In a recent research study, a potential architecture for an innovative aircraft fuel system using H_2 as fuel was proposed [143], [144]. This system, which was developed based on conventional layouts [145], is illustrated in **Figure 54**.

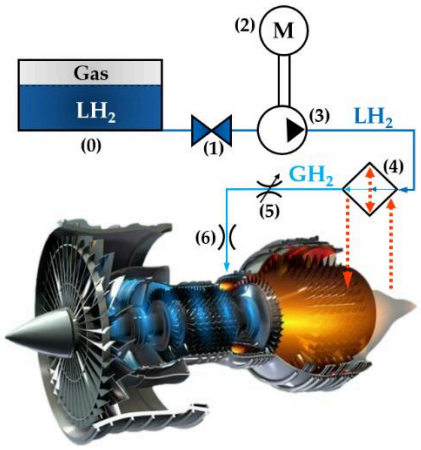

Number	Component
0	Pressurized Tank
1	Shut-off Valve
2	Electric Motor
3	Two-stage Centrifugal Pump
4	Heat Exchanger
5	Metering Valve
6	Injector Nozzles

***Figure 54**. Innovative aircraft fuel system proposed in [143], [144].*

A significant modification involves adapting the system to handle LH_2 instead of kerosene. In conventional aircraft fuel systems, tank-mounted boost pumps are used to transfer fuel to the engines and slightly increase its pressure. For hydrogen aircraft fuel system, a similar setup can be employed, potentially using slightly pressurized tanks with inert gases (0). Shut-off valves (1), as in conventional aircraft fuel systems, can be used to stop LH_2 flow for safety. While positive displacement pumps are suitable for kerosene handling, they are not appropriate for LH_2. The literature suggests that centrifugal pumps are better suited for handling LH_2, which is why the main fuel pump in this innovative system is an electrically driven (2) two-stage centrifugal pump (3). This design allows for greater control flexibility, as the pump's speed can be independently regulated, unlike conventional systems where the main fuel pump is driven through the engine's accessory gearbox [145].

Maintaining cryogenic conditions along the supply line poses a challenge in controlling the flow of LH_2. This challenge is addressed by vaporizing the LH_2 upstream of the metering system using a heat exchanger (4) that recovers heat from exhaust gases exiting the turbine. Thus, after the main fuel pump, H_2 is vaporized and heated to an optimal temperature for combustion in the engine. The downstream components involved in fuel metering are then adapted to handle GH_2. Specifically, while a conventional engine's fuel metering unit (FMU) includes components such as a fuel metering servovalve, bypass valve, actuator valve, pressurizing valve, and shut-off valve to control the flow of liquid kerosene delivered for combustion and for adjusting the position of compressor inlet guide vanes [145], this innovative system uses a cutting-edge metering valve (5) for handling GH_2. The novel metering valve is a convergent-divergent nozzle that precisely controls the flow of GH_2 into the combustion chamber by adjusting the throat area. Additionally, an external hydraulic unit with conventional two-stage servovalves is used for primary and secondary flight controls. It is important to note that, despite their high complexity and high internal leakage issues, which can be addressed with piezoelectric actuators [132], [146], two-stage servovalves are preferred over single-stage proportional solenoid valves in aeronautical applications due to their better response time and advantages in compactness and lightweight [147].

One of the key components of this innovative aircraft fuel system, which operates initially with LH_2 and then with GH_2, is the heat exchanger. This component marks a significant difference between kerosene and hydrogen fuel systems. Although conventional aircraft fuel systems also use heat exchangers to raise the fuel temperature to the ideal range for combustion before it reaches the FMU, the heat exchanger plays a more crucial role in hydrogen-powered aircraft fuel systems because H_2 requires a phase change from cryogenic liquid to gas for the metering process.

To the authors' knowledge, there are only a few studies in the literature focusing on the design of cryogenic heat exchangers for hydrogen-powered aircraft engines [148], [149], [150]. In particular, one such study [150], examined the use of compact, engine-integrated heat exchangers for intercooling and recuperation systems in hydrogen-fuelled turbofan engines for short-to-medium range aircraft. The authors specifically evaluated the impact of these heat exchangers on fuel consumption and emissions, discovering that an intercooled-recuperated engine could reduce specific fuel consumption at take-off by up to 7.7%, while an intercooled engine achieved a 4% improvement compared to a baseline uncooled engine.

In this context, this paper extends the work presented in [151] by designing and modelling a novel cryogenic heat exchanger for the innovative fuel system illustrated in **Figure 54**, with the goal of advancing sustainable aviation. Indeed, in previous studies [143], [144] the heat exchanger (4) was modelled by means of Matlab/Simulink as a "black box" to facilitate the phase change from LH_2 to GH_2 using exhaust gas thermal energy. This paper

expands on that work by proposing and modelling a feasible heat exchanger architecture based on the take-off phase. Specifically, the pipe-in-pipe technology is used, which, to the authors' knowledge, is not yet available on the market. The paper starts by presenting the proposed heat exchanger architecture in Section 4.2.1. Section 4.2.2 then investigates the feasibility of the proposed configuration using a detailed thermodynamic model based on well-established equations. Finally, Section 4.2.3 provides the results of the calculations, focusing on minimizing the key performance parameters of the heat exchanger architecture, including mass, length, and volume.

4.2.1. Heat Exchanger Layout

As shown in **Figure 54**, LH_2 vaporizes upstream of the metering system via a heat exchanger (4), which uses heat from the exhaust gases exiting the turbine to convert H_2 from its liquid form (LH_2) to a gaseous form (GH_2).

The proposed heat exchanger design, depicted in **Figure 55**, consists of three subunits (recovery heater, main heater, and pre-heater) and incorporates two separate fluid circuits: nitrogen (N_2) and hydrogen (H_2) circuit. Concerning the fluid circuits:

- N_2 circuit: N_2, a safe and inert gas with excellent thermophysical properties, is widely used in high-performance heat exchangers [152], [153]. Specifically N_2 is particularly suitable for use with H_2 under supercritical conditions, as its critical temperature is moderately higher than that of H_2 and, for both fluids, slightly supercritical operative pressures are employed. This aspect makes N_2 a suitable carrier fluid, favoured over commonly used alternatives like water, ethylene, and glycol, as their critical temperatures are excessively higher compared to that of H_2, thus not allowing a correct heat exchange between the fluids in the exchanger. In this system, N_2 operates within a closed-loop circuit:
    - It absorbs heat from the turbine's exhaust gases (EGs), raising its temperature.
    - This energy is then transferred to the H_2 circuit to heat GH_2 to high temperatures.
    - After completing the heat exchange, N_2 is recirculated and reheated by the EGs, enabling continuous operation.
- H_2 circuit: This circuit ensures the complete phase change of H_2 from liquid form (LH_2) to gaseous form (GH_2) while achieving the desired thermodynamic conditions for metering. Key processes include:
    - Pre–Heating: LH_2 is initially vaporized using a portion of the heat from high-temperature GH_2.
    - Main Heating: The resulting GH_2 is further heated through energy transfer from the N_2 circuit.
    - Final Cooling: A portion of the high-temperature GH_2's energy is used to vaporize incoming LH_2. After this step, the GH_2 exits the heat exchanger at the precise thermodynamic conditions required for metering.

The three subunits of the heat exchanger are detailed below:

- Recovery Heater: The first subunit, the recovery heater, captures thermal energy from the EGs leaving the turbine (EG^{in}), which retain significant heat. The hot EGs transfer this heat to N_2, increasing its temperature (N_2^{in}). After the heat exchange, the EGs are discharged into the atmosphere (EG^{out}).
- Main Heater: The high-temperature N_2 exiting the recovery heater (N_2^{in}) flows into the second subunit, called the main heater, where it transfers heat to the H_2. This H_2, already

in gaseous form due to vaporization by the third subunit (the pre-heater) in the H_2 circuit ($H_2^{out,pre}$), receives additional heat from the N_2, further increasing its temperature ($H_2^{out,main}$). Since the N_2 circuit is closed, the cooled nitrogen (N_2^{out}) exits the main heater and is recirculated back to the inlet of the recovery heater for reheating.

- Pre-Heater: LH_2 from the main fuel pump enters the heat exchanger (H_2^{in}) and flows into the third subunit, the pre-heater. Within this subunit, high-temperature GH_2 from the main heater ($H_2^{out,main}$) transfers a part of heat to the incoming LH_2, causing its vaporization. After this process, the GH_2 from the main heater exits the pre-heater at a slightly reduced temperature (H_2^{out}) and is ready to flow toward the metering system under the required thermodynamic conditions.

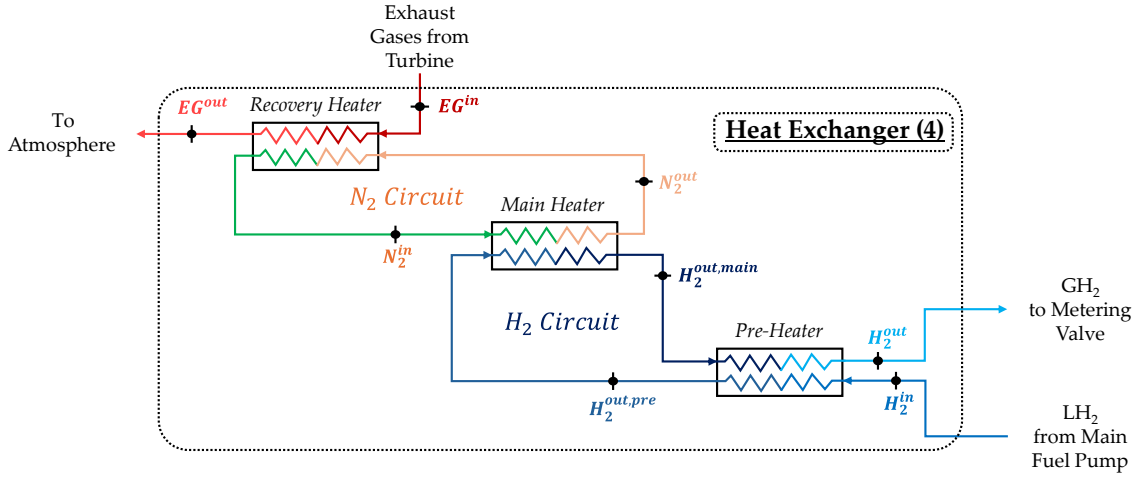

Figure 55. *Heat exchanger layout.*

It is important to note that numerical modelling has been conducted only for the pre-heater and main heater subunits, assuming negligible pressure losses. As a result, the pressure of H_2 in the H_2 circuit and N_2 in the N_2 circuit can be considered constant. This reasonable assumption ensures that pump power consumption remains within acceptable limits, preventing it from rising too high. In this way, the overall system efficiency is not compromised.

For the recovery heater subunit, a possible design is presented in **Figure 56**. This configuration is included for illustrative purposes only and will neither be designed nor modelled in this preliminary analysis. In this concept, the high-temperature EGs exiting the turbine (EG^{in}) transfer heat to N_2 flowing through a serpentine tubular pipe. This pipe, integrated into the structure of the outlet nozzle, acts as the recovery heater subunit. After transferring their heat to the N_2, the EGs are discharged into the atmosphere (EG^{out}).

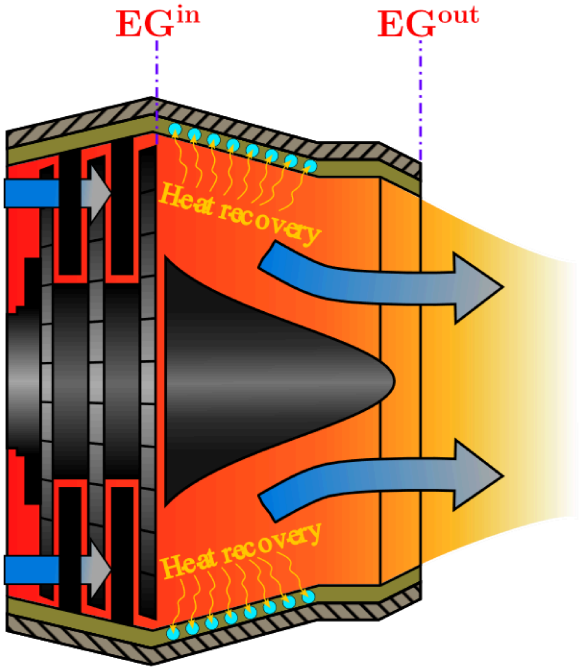

Figure 56. *Possible architecture of the heat recovery subunit.*

4.2.2. Heat Exchanger Numerical Model

This section details the numerical model of the heat exchanger architecture, as previously shown in **Figure 55**. It provides a comprehensive characterization of the system, excluding the recovery heater, which is included only for illustrative purposes. The analysis addresses the input variables, input thermodynamic and geometric parameters, and output variables that define the system's performance.

The thermodynamic model leverages the CoolProp libraries [154] for its calculations. In this model, the two heat exchanger subunits are assumed to be adiabatic to the environment, a valid assumption given that these devices must be effectively insulated using vacuum systems.

The model is structured into three main parts: first, the temperature calculations are detailed (4.2.2.1 Section); second, the heat transfer coefficients are described (4.2.2.2 Section); and finally, the heat exchanger key performance parameters are characterized (4.2.2.3 Section). A schematic representation at the end of this section summarizes the flow of calculations and parameter interrelations.

4.2.2.1. Calculation of the temperatures

Since the recovery heater subunit is included solely to illustrate the heat recovery mechanism from EGs, this study will focus on modelling the remaining two heat exchanger subunits. Each subunit will be represented with four ports, and the corresponding thermodynamic states will be considered.

All thermodynamic calculations are performed using the CoolProp thermodynamic libraries, which are open-source and widely used due to their thorough validation, as shown in [154]. These libraries have the capability to model over 120 fluids with real gas state equations, including HEOS, PR, and SRK [154].

It is important to note that, when referring to H_2, parahydrogen has been considered for these calculations. This choice is driven by the fact that LH_2 storage requires the fuel to

withstand boil-off, a condition that only parahydrogen can meet [155]. Moreover, at 20 K, parahydrogen concentration exceeds 98%, making the presence of orthohydrogen (around 2%) negligible [156]. However, the spontaneous conversion from ortho to para form occurs very slowly, making catalytic conversion unavoidable in hydrogen liquefaction processes [157].

Another key point of this analysis to highlight is that the operating pressures of both fluids in this study considered in the study (N_2 and H_2) are maintained above the critical limit (supercritical conditions) to prevent any two-phase behaviour during the heat exchange process.

The inputs for the calculation are as follows: for the H_2 circuit, the required thermodynamic parameters are the hydrogen mass flow rate ($\dot{m}_{H_2}$), the inlet and outlet temperatures of hydrogen at the heat exchanger ($T_{H_2^{in}}$,$T_{H_2^{out}}$) and the hydrogen pressure (p_{H_2}) [143], [144]. For the N_2 circuit, the input thermodynamic parameters include the inlet and outlet temperatures of nitrogen at the main heater subunit ($T_{N_2^{in}}$,$T_{N_2^{out}}$) and the nitrogen pressure (p_{N_2}). Additionally, the temperature difference between the inlet temperature of nitrogen and the hydrogen outlet temperature at the main heater subunit ($\Delta T_{N_2^{in}\text{-}H_2^{out,main}}$) is required.

Using these inputs, the nitrogen mass flow rate ($\dot{m}_{N_2}$), the main heater hydrogen outlet enthalpy ($h_{H_2^{out,main}}$) and the pre-heater hydrogen outlet enthalpy ($h_{H_2^{out,pre}}$) can be evaluated from the following equations, which describe the power balance for the main heater subunit (1), the pre-heater subunit (2), and the temperature difference between the inlet temperature of nitrogen and the hydrogen outlet temperature at the main heater (3).

$$\dot{m}_{N_2} \cdot \left(h_{N_2^{in}} - h_{N_2^{out}} \right) = \dot{m}_{H_2} \cdot \left(h_{H_2^{out,main}} - h_{H_2^{out,pre}} \right) \tag{61}$$

$$h_{H_2^{out,main}} - h_{H_2^{out}} = h_{H_2^{out,pre}} - h_{H_2^{in}} \tag{62}$$

$$\Delta T_{N_2^{in}\text{-}H_2^{out,main}} = T_{N_2^{in}} - T_{H_2^{out,\,main}}, \tag{63}$$

where:

- $h_{N_2^{in}}$ and $h_{H_2^{in}}$ are the enthalpies for N_2 at the inlet of the main heater subunit and for H_2 at inlet of the heat exchanger, respectively;
- $h_{N_2^{out}}$ and $h_{H_2^{out}}$ are the enthalpies for N_2 at the outlet of the main heater subunit and for H_2 at the outlet of the heat exchanger, respectively;
- $T_{H_2^{out,\,main}}$ is the temperature associated with $h_{H_2^{out,main}}$.

Specifically, to solve these equations, the CoolProp libraries are used to calculate the enthalpies required for equations (1) and (2). Once the enthalpies are obtained ($h_{H_2^{out,main}}$, $h_{H_2^{out,pre}}$), CoolProp is used again to calculate the associated temperatures ($T_{H_2^{out,main}}$, $T_{H_2^{out,pre}}$), which are then used to determine the temperature profile inside the pipes (for both subunits). **Figure 57** illustrates qualitatively the heat exchange process occurring in the pre-heater and main heater subunits.

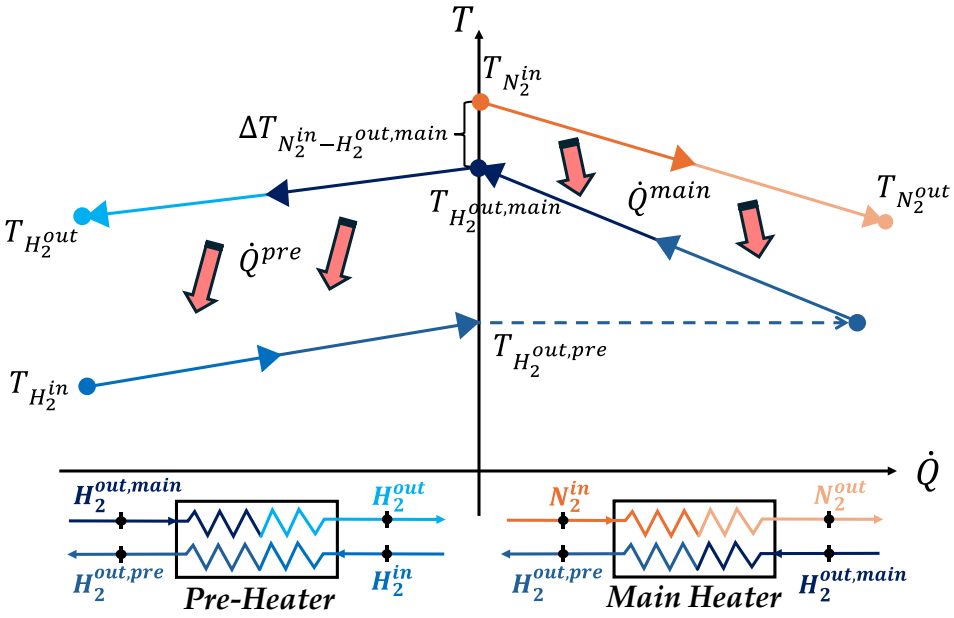

Figure 57. *Qualitative temperature-thermal power diagram schematizing the heat exchanges in both subu-nits and illustrating the working parameters for the process.*

The technology at the core of this study is the pipe-in-pipe technology, where the internal pipes are enclosed within the external ones. In both heat exchanger subunits, the hot fluid flows inside the internal pipe, while the cold fluid circulates in the space between the internal and external pipes. This configuration offers advantages in terms of compactness and reduced system weight. The system geometry is shown in **Figure 58** where $d_{i,i}$ represents the internal diameter of the internal pipe, $d_{e,i}$ represents the external diameter of the internal pipe, $d_{i,e}$ represents the internal diameter of the external pipe and $d_{e,e}$ represents the external diameter of the external pipe. The authors are unaware of any previous market applications of this technology, making it a novel proposal. The number of pipes (n_t) is the same for both the main heater and pre-heater subunits.

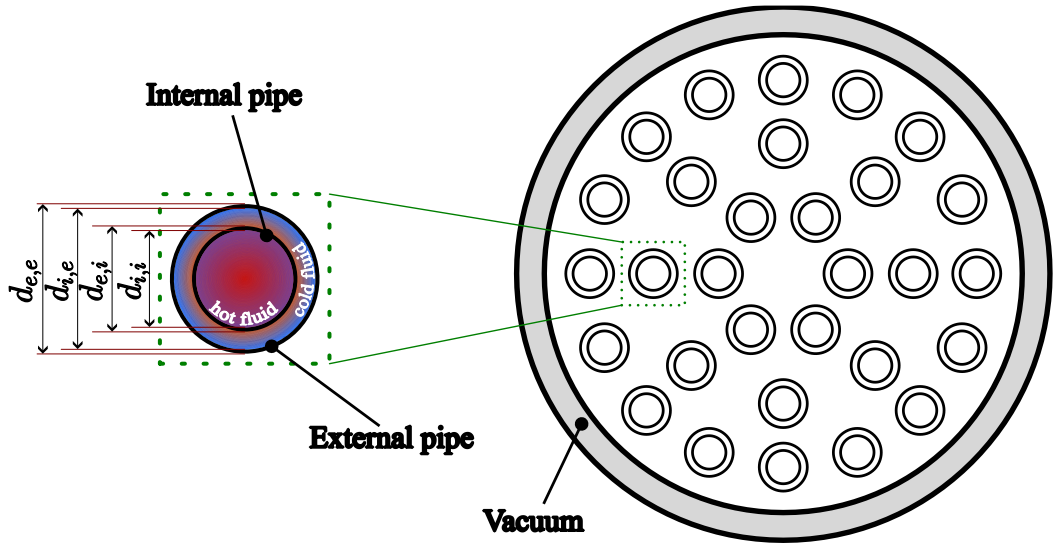

Figure 58*. Schematic representation of the pipe-in-pipe heat exchanger technology with key geometric parameters.*

All considerations regarding the thermodynamic states must align with the material strength of the pipes (for both subunits). The pipes need to withstand the pressure imposed by the system to prevent any potential breakdowns. To ensure that the chosen material can handle the required pressure, a law governing the minimum required thickness for a pressurized vessel is applied, specifically the Mariotte's law which is shown in the following equation:

$$t \geq \frac{p \cdot d_i}{2\sigma_{yield}} \cdot \alpha \tag{64}$$

where t is the minimum thickness required for the generic tube, p is the pressure acting on the pipe walls, d_i is the internal diameter of the generic pipe, σ_{yield} is the yield stress of the material and α is the Mariotte safety coefficient.

Since the two heat exchanger subunits (namely, the pre-heater and the main heater) use the pipe-in-pipe technology for their pipe configuration, it is important to specify the hot and cold fluids in each subunit. For this reason, **Table 19** below details, for each subunit, the hot fluid (denoted by the subscript "h") and the cold fluid (denoted by the subscript "c").

***Table 19**. Specification of cold fluid and hot fluid for both heat exchanger subunits.*

	Cold fluid (c)	**Hot fluid (h)**
Pre-heater	H_2^{in}	$H_2^{out,main}$
Main heater	$H_2^{out,pre}$	N_2^{in}

The flow area for both the cold fluid and the hot fluid can be calculated as:

$$A_h = \frac{\pi \cdot d_{i,i}^2}{4} \tag{65}$$

$$A_c = \frac{\pi \cdot \left(d_{i,e}^2 - d_{e,i}^2\right)}{4} \tag{66}$$

where, A_h represents the flow area for the hot fluid, while A_c represents the flow area for the cold fluid. By means of equations (65–66), the hydraulic diameter for the hot fluid $(d_h)_h$ and the hydraulic diameter for the cold fluid $(d_h)_c$ can be obtained as follows:

$$(d_h)_h = \frac{4 \cdot A_h}{\pi \cdot d_{i,i}} \tag{67}$$

$$(d_h)_c = \frac{4 \cdot A_c}{\pi \cdot (d_{i,e} + d_{e,i})} \tag{68}$$

In order to trace the temperature profile along the pipes, they can be ideally divided into modules, with constant properties assumed for each module. In this analysis, the number of modules is imposed to be n=50 for both subunits. In each module, the cold fluid undergoes a temperature variation given by:

$$\Delta T_c = \frac{T_c^{out} - T_c^{in}}{n} \tag{69}$$

where T_c^{out} and T_c^{in} represent the outlet temperature and the inlet temperature of the generic cold fluid. A single module can be schematically represented in **Figure 59**, where $(T_{in,h})_i$, $(T_{out,h})_i$, $(T_{in,c})_i$, $(T_{out,c})_i$ and $(\Delta x)_i$ are the input and output temperature for the hot fluid, the input and output temperature for the cold fluid, and the length of the i-th module, respectively.

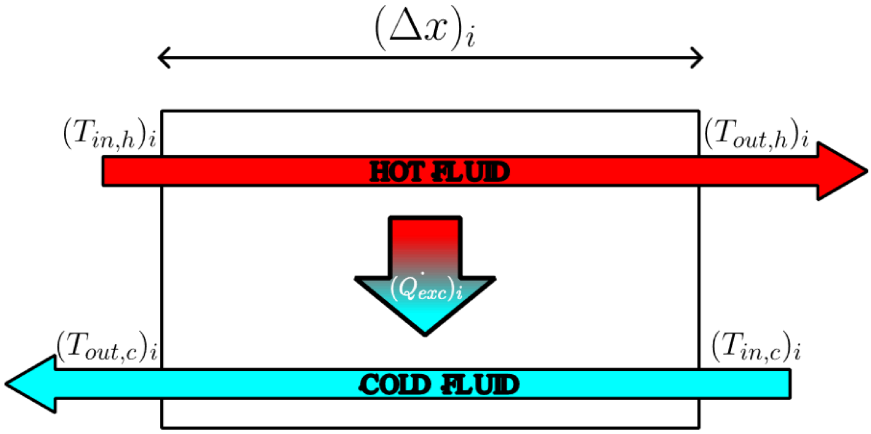

***Figure 59**. Schematic representation of a heat exchanger module.*

The outlet temperature of the cold fluid in each module i (i = 1,…n) is calculated as follows:

$$(T_{out,c})_i = (T_{in,c})_i + \Delta T_c \tag{70}$$

$$(T_{in,c})_i = (T_{out,c})_{i-1} \tag{71}$$

where $(T_{in,c})_1 \equiv T_c^{in}$ and $(T_{out,c})_n \equiv T_c^{out}$. For the pre-heater $T_c^{in} \equiv T_{H_2}^{in}$, while for the main heater $T_c^{in} \equiv T_{H_2}^{out,pre}$. Similarly, for the pre-heater $T_c^{out} \equiv T_{H_2}^{out,pre}$, while for the main heater $T_c^{out} \equiv T_{H_2}^{out,main}$. Once $(T_{in,c})_i$ and $(T_{out,c})_i$ are known, CoolProp libraries can be used to calculate the corresponding enthalpies $(h_{in,c})_i$ and $(h_{out,c})_i$. The values of the latter can be used to calculate the thermal power absorbed by the cold fluid in a single module:

$$(T_{in,c})_i = (T_{out,c})_{i-1} \tag{72}$$

where $\dot{m}_c$ represents the mass flow rate of the generic cold fluid. Since the thermal power absorbed by the cold fluid is equal to the thermal power provided by the hot fluid, the inlet enthalpy and the outlet enthalpy of the hot fluid can be calculated for each module (i) as follows:

$$\left(h_{in,h}\right)_i = \left(h_{out,h}\right)_i + \frac{\left(\dot{Q}_{exc}\right)_i}{\dot{m}_h} \tag{73}$$

$$\left(h_{out,h}\right)_i = \left(h_{in,h}\right)_{i-1} \tag{74}$$

where $\dot{m}_h$ represents the mass flow rate for the hot fluid. Similarly to the cold fluid, when i=1, $\left(h_{out,h}\right)_1 \equiv h_h^{out}$, where h_h^{out} is the outlet enthalpy for the generic hot fluid. For the pre-heater $h_h^{out} \equiv h_{H_2^{out}}$, while for the main heater $h_h^{out} \equiv h_{N_2^{out}}$. Consequently, once $\left(h_{out,h}\right)_i$ and $\left(h_{in,h}\right)_i$ have been determined in each module (i), the temperatures of the hot fluid $\left(T_{out,h}\right)_i$ and $\left(T_{in,h}\right)_i$ can be calculated in each module (i), by using the libraries of CoolProp, as a function of pressure and enthalpy.

4.2.2.2. Calculation Of The Heat Transfer Coefficients

After the temperature profile along the pipes is traced, it is possible to calculate the heat transfer coefficients, with reference to the average fluid properties of each module (i), which are defined for cold fluid $(\overline{T_c})_i$ and hot fluid $(\overline{T_h})_i$ as follows:

$$(\overline{T_h})_i = \frac{(T_{in,h})_i + (T_{out,h})_i}{2};\ (\overline{T_c})_i = \frac{(T_{in,c})_i + (T_{out,c})_i}{2} \tag{75}$$

Once again, by means of CoolProp libraries, once the average temperatures are obtained for each module (i), it is also possible to calculate:

- The average densities of the hot and cold fluids ($(\overline{\rho_h})_i$, $(\overline{\rho_c})_i$);
- The average thermal conductivities of the hot and cold fluids ($(\overline{\lambda_h})_i$, $(\overline{\lambda_c})_i$);
- The average viscosities of the hot and cold fluids ($(\overline{\mu_h})_i$, $(\overline{\mu_c})_i$);
- The average specific heats of the hot and cold fluids ($(\overline{cp_h})_i$, $(\overline{cp_c})_i$).

Another property to be calculated in each module (i) is the average velocity for both the hot fluid and the cold fluid:

$$(\overline{V_x})_i = \frac{\dot{m}_x}{n_t \cdot (\overline{\rho_x})_i \cdot A_x} \tag{76}$$

where either x=h (hot fluid) or x=c (cold fluid).

Along these average thermodynamic and cinematic parameters, also the average Reynolds number and the average Prandtl number of the hot and cold fluids can be calculated in each module (i) as:

$$(\overline{Re_x})_i = \frac{(\overline{V_x})_i \cdot (\overline{\rho_x})_i \cdot d_{h,x}}{(\overline{\mu_x})_i} \tag{77}$$

$$(\overline{Pr_x})_i = \frac{(\overline{\mu_x})_i \cdot (\overline{cp_x})_i}{(\overline{\lambda_x})_i} \tag{78}$$

The Average Nusselt number in each module (i) is expressed as a function of the average Reynolds number as:

- when $(\overline{Re_x})_i < 2300$ $(\overline{Nu_x})_i = 4.36$
- when $2300 < (\overline{Re_x})_i < 10^6$ the Gnielinski correlation can be used
- when $(\overline{Re_x})_i > 10^6$, the Chilton-Coulburn correlation can be used.

The following Equation 79 encloses all the cases above described:

$$(\overline{\mathrm{Nu_x}})_\mathrm{i}=\begin{cases} 4.36, & \text{if } (\overline{\mathrm{Re_x}})_\mathrm{i}<2300 \\ \dfrac{\frac{(\xi)_\mathrm{i}}{8}\cdot((\overline{\mathrm{Re_x}})_\mathrm{i}\text{-}1000)\cdot(\overline{\mathrm{Pr_x}})_\mathrm{i})}{1+12.7\left(\frac{(\xi)_\mathrm{i}}{8}\right)^{0.5}\cdot\left((\overline{\mathrm{Pr_x}})_\mathrm{i}{}^{2/3}\text{-}1\right)}, & \text{if } 2300<(\overline{\mathrm{Re_x}})_\mathrm{i}<10^6 \\ 0.023\cdot(\overline{\mathrm{Re_x}})_\mathrm{i}{}^{0.8}\cdot(\overline{\mathrm{Pr_x}})_\mathrm{i}{}^{1/3}, & \text{if } (\overline{\mathrm{Re_x}})_\mathrm{i}>10^6 \end{cases} \quad (79)$$

where $(\xi)_\mathrm{i}$ represents the friction factor in each module (i), which can be calculated as:

$$(\xi)_i = (1.82 \cdot log(\overline{Re_x})_i - 1.64)^{-2} \quad (80)$$

Equations (79-80) are well established and widely used in the literature [158], [159]; therefore, they are to be considered reliable for fully developed (hydrodynamically and thermally) flow.

Finally, once all these average quantities are available, the convective heat exchange coefficients in each module (*i*), for the hot fluid $\left(\overline{\mathrm{h_h}}\right)_\mathrm{i}$ and cold fluid $\left(\overline{\mathrm{h_c}}\right)_\mathrm{i}$, can be obtained as:

$$\left(\overline{h_h}\right)_i = \frac{(\overline{Nu_h})_i \cdot (\overline{\lambda_h})_i}{d_{h,h}} \;;\; \left(\overline{h_c}\right)_i = \frac{(\overline{Nu_c})_i \cdot (\overline{\lambda_c})_i}{d_{h,c}} \quad (81)$$

4.2.2.3. Calculation of the Performance Parameters

The knowledge of the convective heat exchange coefficients and the temperatures of the hot and cold fluids allows for the determination of the mean heat transfer coefficient $(\mathrm{U})_\mathrm{i}$ and the logarithmic mean temperature difference $(\overline{\Delta \mathrm{T}})_\mathrm{i}$ in each module (i) with the following equations:

$$(U)_i = \frac{1}{\frac{1}{\left(\overline{h_c}\right)_i} + \frac{1}{\left(\overline{h_h}\right)_i \cdot \frac{d_{i,i}}{d_{e,i}}} + \frac{d_{e,i} \cdot ln\frac{d_{e,i}}{d_{i,i}}}{2 \cdot \lambda}} \quad (82)$$

$$(\overline{\Delta T})_i = \frac{[(T_{in,h})_i - (T_{out,c})_i] - [(T_{out,h})_i - (T_{in,c})_i]}{ln\left(\frac{(T_{in,h})_i - (T_{out,c})_i}{(T_{out,h})_i - (T_{in,c})_i}\right)} \quad (83)$$

where λ is the thermal conductivity of the material constituting the pipes. In this way, it is possible to determine the length of each module (Δx_i), and thus the overall length of both heat exchanger subunits (pre-heater and main heater):

$$\Delta x_i = \frac{(\dot{Q}_{exc})_i}{\pi \cdot d_{e,i} \cdot n_t \cdot U_i \cdot (\overline{\Delta T})_i} \tag{84}$$

$$L_y = \sum_{i=1}^{n} \Delta x_i \tag{85}$$

where "y" is a generic subscript indicating the pre-heater when y=pre and the main heater when y=main. To represent the total length of the pipes, considering the lengths of both subunits, it is defined as: $L_{tot}=L_{pre}+L_{main}$. The pressure drop is calculated using the Darcy formula for both the hot (Δp_h) and cold (Δp_c) fluids (for both subunits), based on the average properties of the fluids, as follows:

$$\Delta p_h = \sum_{i=1}^{n} \frac{1}{2} \cdot (f_h)_i \cdot \left(\overline{V_h}\right)_i^2 \cdot (\overline{\rho_h})_i \cdot \frac{\Delta x_i}{d_{h,h}} \tag{86}$$

$$\Delta p_c = \sum_{i=1}^{n} \frac{1}{2} \cdot (f_c)_i \cdot \left(\overline{V_c}\right)_i^2 \cdot (\overline{\rho_c})_i \cdot \frac{\Delta x_i}{d_{h,c}} \tag{87}$$

where $(f_h)_i$ and $(f_c)_i$ are the friction factors in rough pipes for the hot and cold fluids, respectively, calculated based on the value of the average Reynold number in each module (i):

$$(f_x)_i = \begin{cases} \dfrac{64}{(\overline{Re_x})_i}, & \text{if } (\overline{Re_x})_i < 2300 \\ \dfrac{1}{\left[-1.8 \cdot \log\left(\left(\dfrac{\varepsilon}{d_{h,x}3{,}7}\right)^{1.11} + \dfrac{6.9}{(\overline{Re_x})_i}\right)\right]^2}, & \text{if } (\overline{Re_x})_i \geq 2300 \end{cases} \tag{87}$$

where the first expression represents laminar flow condition, while the second expression (also known as Haaland formula) is representative of turbulent flow and ε is the roughness of the tubes. In order to calculate the mass of both the heat exchanger subunits, the following equation is applied:

$$m_y = V_y \cdot \rho_{mat} \tag{88}$$

where ρ_{mat} is the density of the selected material and V_y indicates the volume of the pipes, which is evaluated as:

$$V_y = \pi \cdot \left[\frac{\left(d_{e,e}^2 - d_{i,e}^2\right) + \left(d_{e,i}^2 - d_{i,i}^2\right)}{4}\right] \cdot L_y \tag{89}$$

Similarly to the comprehensive length of the pipes, the total mass of the latter can be indicated as: $m_{tot}=m_{pre}+m_{main}$, while the total volume of the pipes: $V_{tot} = V_{pre} + V_{main}$.

4.2.3. Results

This section evaluates the feasibility of the proposed heat exchanger architecture using the thermodynamic model described earlier. In the calculation, the pre-heater is divided into 50 modules, as is the main heater. **Table 20** summarizes the input parameters for the H_2 circuit, including the inlet LH_2 temperature to the heat exchanger, the outlet GH_2 temperature from the heat exchanger, as well as the H_2 circuit pressure and mass flow rate. These parameters are derived from [143], [144], which introduced and modelled the innovative hydrogen-fuelled aircraft system depicted in **Figure 54** using Matlab/Simulink. The numerical model in these studies was validated by comparing simulated operating conditions with data from the literature [160], focusing on the take-off phase.

Building on this foundation, the current study aims to design the heat exchanger architecture, previously illustrated in **Figure 55** (taking into account only the pre-heater and main heater subunits), suitable for integration into the innovative hydrogen-fuelled aircraft system, with particular attention to the take-off phase. This phase is identified as the most critical for optimizing the dimensions and performance parameters of the heat exchanger [160].

***Table 20**. H_2 thermodynamic parameters used as inputs in the calculation [143], [144], [160].*

	Parameter	Symbol	Take-Off Value [Unit]
H_2 Circuit	Mass flow rate	$\dot{m}_{H_2}$	0.411 [kg/s]
	LH2 inlet heat exchanger temperature (from main fuel pump)	$T_{H_2}^{in}$	29.9 [K]
	GH2 outlet heat exchanger temperature (to metering valve)	$T_{H_2}^{out}$	353 [K]
	Pressure	p_{H_2}	51.55 [bar]

Specific assumptions were made to define the operating thermodynamic conditions of the N_2 circuit:

- The N_2 inlet temperature to the main heater, $T_{N_2}^{in}$, was set to 504 K. This value represents the temperature achieved by N_2 after heat exchange with the EGs in the recovery heater.

- The pressure in the N_2 circuit was set to 70 bar.

These N_2 input thermodynamic parameters, summarized in **Table 21**, were chosen to ensure N_2 in a supercritical gaseous state at high temperature, optimizing its thermophysical properties for effective heat transfer.

***Table 21**. N_2 thermodynamic parameters used as inputs in the calculation.*

	Parameter	Symbol	Value [Unit]
N_2 Circuit	N_2 inlet main heater temperature	$T_{N_2}^{in}$	504 [K]
	Pressure	p_{N_2}	70 [bar]

To comply with the temperature limits outlined in ASME B31.12 (Standard on Hydrogen Piping and Pipelines), austenitic stainless steels (300 series) are recommended for piping in both GH_2 and LH_2 systems, rather than other materials like aluminium, which, despite having better thermal conductivity, offers lower corrosion resistance and mechanical strength [161]. Among the various stainless steel grades, 316/316L is preferred due to its superior stability and resistance to H_2 embrittlement, especially under high-pressure and temperature H_2 exposure [162]. This balance of thermal performance and structural reliability makes it the ideal choice for this application.

For the pre-heater and main heater subunits, piping made from stainless steel 316 was chosen. Using its material properties, along with the pipe key geometric parameters provided as model inputs, the minimum pipe thickness was calculated based on the Mariotte formula.

It is important to remind that in the pipes of pre-heater subunit, the hot fluid (h) is the high-temperature GH_2 exiting the main heater subunit ($H_2^{out,main}$), while the cold fluid (c) is the LH_2 supplied from the main fuel pump (H_2^{in}). Conversely, in the pipes of the main heater subunit, the cold fluid (c) is the vaporized H_2 leaving the pre-heater subunit ($H_2^{out,pre}$), and the hot fluid (h) is the high-temperature N_2 from the recovery heater subunit (N_2^{in}), where it absorbs heat from EGs.

The material properties of stainless steel 316/316L are detailed in **Table 22**, while the considered geometric parameters of the pipes, and the calculated minimum pipe thickness are summarized in **Table 23**.

***Table 22**. Stainless steel 316 properties.*

	Propriety	Symbol	Value [Unit]
Stainless Steel 316	Density	ρ_{mat}	8060 [kg/m3]
	Tensile Strength, Yield	σ_{yield}	200 [MPa]
	Tensile Strength, Max	σ_{max}	550 [MPa]
	Young Modulus	E_{mat}	193 [GPa]
	Specific Heat Capacity	c_{mat}	500 [J/(kg·K)]
	Thermal Conductivity	λ_{mat}	16 [W/(m·K)]

***Table 23**. Key geometric parameters and calculated minimum thickness of the pipes (pre-heater and main heater subunits).*

		Internal tube		External tube	
	Parameter	**Symbol**	**Value [Unit]**	**Symbol**	**Value [Unit]**
Geometry of Pipes (both Subunits)	Internal Diameter	$d_{i,i}$	20 [mm]	$d_{i,e}$	25 [mm]
	External Diameter	$d_{e,i}$	20.8 [mm]	$d_{e,e}$	26 [mm]
	Roughness	ε_i	0.2 [mm]	ε_e	0.2 [mm]
	Safety factor for Mariotte's law	α_i	1.5 [-]	α_e	1.5 [-]
	Calculated Minimum Thickness	t_i	0.22 [mm]	t_e	0.48 [mm]
	Actual Thickness	$t_{i,t}$	0.8 [mm]	$t_{e,t}$	1 [mm]

To identify the optimal design point for the heat exchanger, minimizing its performance parameters, namely the total pipes length ($L_{tot} = L_{pre} + L_{main}$) and mass ($m_{tot} = m_{pre} + m_{main}$), three key input parameters of the thermodynamic model were varied:

1. The outlet N_2 temperature from the main heater ($T_{N_2}^{out}$).
2. The temperature difference between the inlet N_2 temperature to the main heater and the outlet H_2 temperature from the main heater ($\Delta T_{N_2^{in}\text{-}H_2^{out,main}}$).
3. The number of pipes in both the pre-heater and main heater subunits (n_t).

The process was conducted using Esteco modeFRONTIER software [104], with a constraint that the pressure drops across the pipes remains below $\Delta p \leq 0.1$ bar. This applied to both the cold fluids (denoted as "c") and hot fluids (denoted as "h") in the respective subunits, ensuring that the heat exchange process in both subunits could be treated as isobaric.

Table 24 provides a summary of the input variables involved in the calculation, including their value ranges, variation steps and number of points considered. The constraints applied during the process are outlined in **Table 25**. A total of 60 design points were generated, which can be easily obtained by multiplying the individual number of points for each input variable.

***Table 24**. Input thermodynamic and geometric variables: Range values, Step size, and Number of points.*

	Parameter	**Symbol**	**Range Values [Unit]**	**Step size [Unit]**	**Number of Points**
Input Thermodynamic Variables	N_2 outlet main heater temperature	$T_{N_2}^{out}$	(228.15 – 273.15) [K]	15 [K]	4
	Temperature difference between N_2 entering and H_2 exiting the main heater	$\Delta T_{N_2^{in}\text{-}H_2^{out,main}}$	(70 – 130) [K]	15 [K]	5
Input Geometric Variables	Number of pipes (both subunits)	n_t	(80 – 100) [-]	10 [-]	3

Table 25. *Constraints considered in the calculation process.*

	Propriety	Symbol	Objective [Unit]
Constraints	Pressure drops across pipes (both subunits)	Δp	≤ 0.1 [bar]

The results, showing the influence of these input variables ($T_{N_2}^{out}$, $\Delta T_{N_2^{in}\text{-}H_2^{out,main}}$) and n_t) on the performance parameters (L_{tot} and m_{tot}) are presented in **Figure 60**, which highlights the selected optimal design point. The analysis reveals that higher values of the thermodynamic variables ($T_{N_2}^{out}$ and $\Delta T_{N_2^{in}\text{-}H_2^{out,main}}$) combined with intermediate values of the geometric variable (n_t) effectively minimize both the total length (L_{tot}) and mass (m_{tot}) of the heat exchanger. Based on this, the optimal design point has been selected with $T_{N_2}^{out}$ = 273.15 K, $T_{N_2^{in}\text{-}H_2^{out,main}}$ = 130 K and n_t = 90. **Table 26** specifies the thermodynamic and geometric input variable values corresponding to the optimal design point.

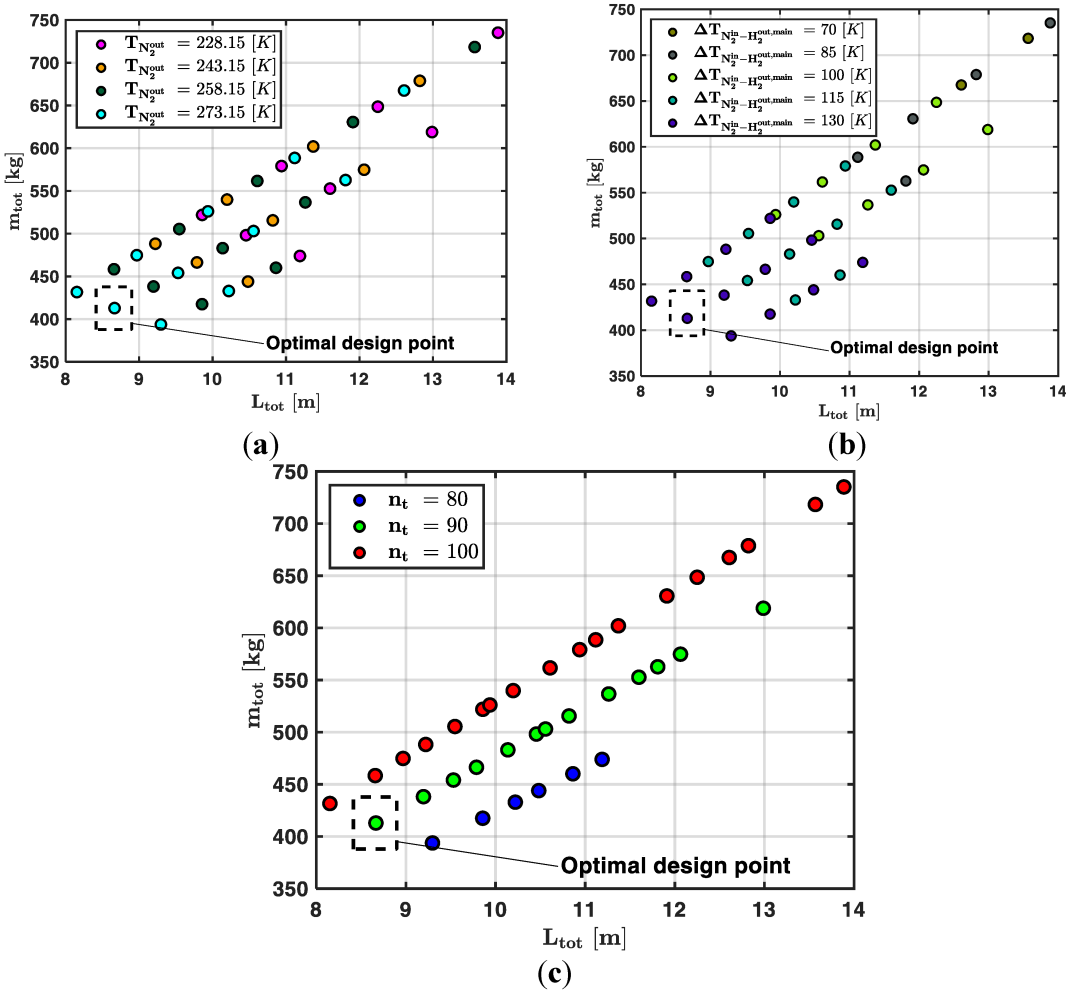

Figure 60. $m_{tot} - L_{tot}$ *plots showing the influence of the input thermodynamic and geometric variables on key performance parameters:* ***(a)*** $T_{N_2}^{out}$ *;* ***(b)*** $\Delta\, T_{N_2^{in}-H_2^{main}}$*;* ***(c)*** *and* n_t .

***Table 26**. Values of thermodynamic and geometric input variables for the selected design point.*

	Parameter	Symbol	Design Point Value [Unit]
Input Thermodynamic Variables	N_2 outlet main heater temperature	$T_{N_2}^{out}$	273.15 [K]
	Temperature difference between N_2 entering and H_2 exiting the main heater	$\Delta T_{N_2^{in}-H_2^{out,main}}$	130 [K]
Input Geometric Variables	Number of pipes (both subunits)	n_t	90 [-]

Considering the thermodynamic input values for N_2 corresponding to the optimal design point from **Table 26** and the assumed values from **Table 21**, along with the input values for H_2 provided in **Table 20** (to meet the take-off phase requirements), the corresponding enthalpies for the H_2 and N_2 circuits, as calculated by the thermodynamic model using CoolProp, are presented in **Table 27**. It is important to note that the thermodynamic model also incorporates the input geometric parameters of the pipes (for both subunits) from **Table 23**, considers the properties of stainless steel 316 for the pipes (for both subunits) from **Table 22**, and uses the optimal number of pipes (for both subunits), as previously obtained and specified in **Table 26**.

***Table 27**. Values of thermodynamic and geometric input variables for the selected design point.*

	Parameter	Symbol	Value [Unit]
H_2 circuit	LH_2 inlet enthalpy (from main fuel pump)	$h_{H_2}^{in}$	148.7 [kJ/kg]
	GH_2 outlet enthalpy (to metering valve)	$h_{H_2}^{out}$	5264 [kJ/kg]
N_2 circuit	N_2 inlet enthalpy (to main heater)	$h_{N_2}^{in}$	522.5 [kJ/kg]
	N_2 outlet enthalpy (from main heater)	$h_{N_2}^{out}$	265.8 [kJ/kg]

Additionally, the results from solving Equations (61–63), as described earlier, are presented in **Table 28**. These outcomes, which are detailed below, also include the thermal powers absorbed/released by the cold/hot fluids in both subunits:

- The temperatures and enthalpies of H_2 at the outlets of the pre-heater and main heater subunits.
- The required mass flow rate of N_2 in the main heater subunit.
- The thermal power absorbed by LH_2 and released by GH_2 in the pre-heater subunit.
- The thermal power absorbed by GH_2 and released by N_2 in the main heater subunit.

These data provide a comprehensive evaluation of the heat exchange process.

***Table 28**. Heat exchange calculations for the pre-heater and main heater subunits.*

	Parameter	Symbol	Value [Unit]
H_2 circuit	Vaporized H_2 outlet temperature (from pre-heater)	$T_{H_2}^{out,pre}$	47.6 [K]
	Vaporized H_2 outlet enthalpy (from pre-heater)	$h_{H_2}^{out,pre}$	457.14 [kJ/kg]
	Thermal Power absorbed by LH_2 (in the pre-heater)	$\dot{Q}_{LH_2}^{pre}$	126.75 [kW]
	GH_2 outlet temperature (from main heater)	$T_{H_2}^{out,main}$	374 [K]
	GH_2 outlet enthalpy (from main heater)	$h_{H_2}^{out,main}$	5572.5 [kJ/kg]
	Thermal Power absorbed by GH_2 (in the main heater)	$\dot{Q}_{GH_2}^{main}$	2102.4 [kW]
	Thermal Power released by GH_2 (in the pre-heater)	$\dot{Q}_{GH_2}^{pre}$	-126.75 [kW]
N_2 circuit	N_2 mass flow rate (in the main heater)	$\dot{m}_{N_2}$	8.19 [kg/s]
	Thermal Power released by N_2 (in the main heater)	$\dot{Q}_{N_2}^{main}$	-2102.4 [kW]

With the thermodynamic data for the heat exchange in both subunits fully determined, the trends of the thermodynamic states of H_2 and N_2 throughout the pre-heater and main heater subunits can be analysed. **Figure 61** illustrates these thermodynamic transformations for both fluids on a temperature-entropy (T-s) diagram, with **Figure 61a** detailing the transformations for H_2 and **Figure 61b** for N_2. It is evident that no two-phase or cyclic behaviours occur during heat exchange, as both fluids are handled at supercritical pressure values.

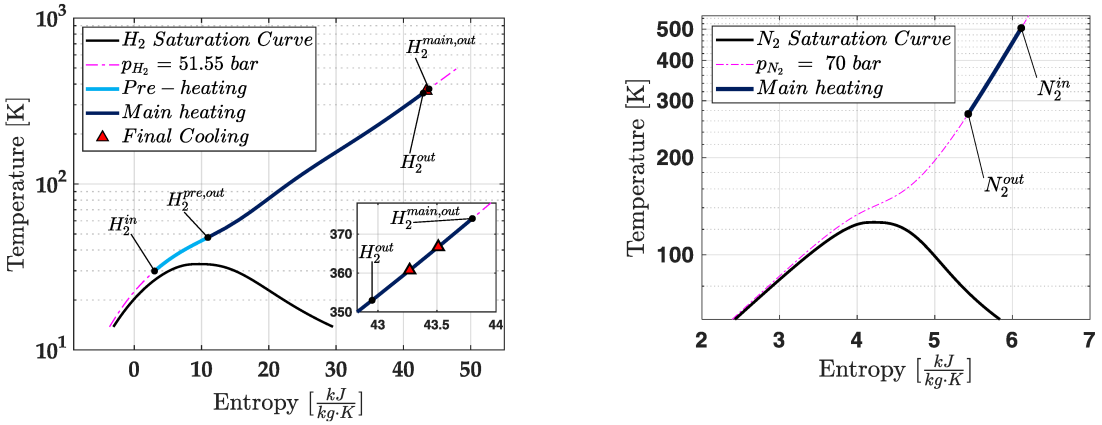

(a) **(b)**

***Figure 61**. Thermodynamical transformations through the heat exchanger subunits for: (a) H_2; (b) N_2.*

Furthermore, **Figure 62** illustrates the temperature-thermal power plots for both the pre-heater (**Figure 62a**) and the main heater (**Figure 62b**), based on the identified optimal design

point. It is evident that this depiction, which includes the calculated data (quantitative graphs), is analogous to **Figure 56**, which instead presents a qualitative graph.

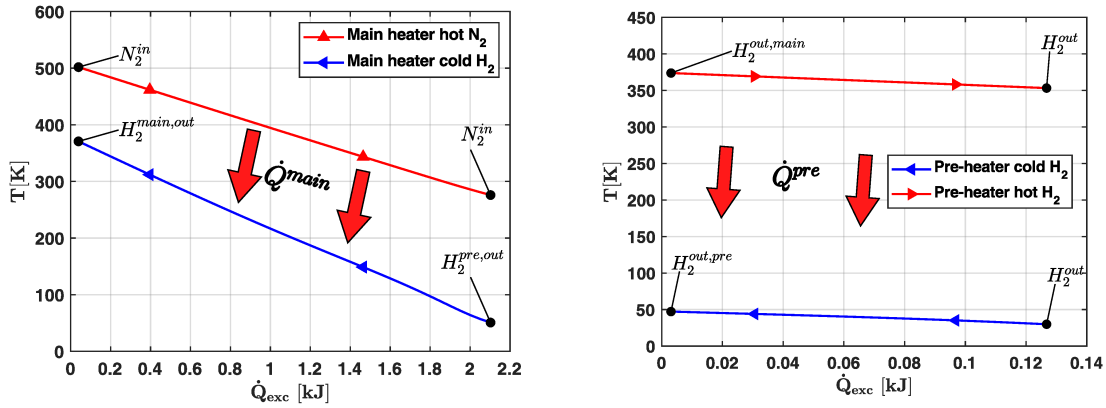

(a) **(b)**

Figure 62. *Temperature-thermal power plot for both subunits: (a) Main heater; (b) Pre-heater.*

In conclusion, **Table 29** summarizes the key performance parameters of the heat exchanger for both the pre-heater and main heater subunits, along with the pressure drop across the pipes for both the hot and cold fluids.

Table 29. *Key performance parameters and pressure drops across the pipes (for both subunits) calculated at the optimal design point.*

	Parameter	Symbol	Value [Unit]
Pre-heater	Length	L_{pre}	0.141 [m]
	Mass	m_{pre}	6.711 [kg]
	Volume	V_{pre}	$9.25 \cdot 10^{-6}$ [m^3]
	Pressure drops hot fluid (GH_2)	Δp_h^{pre}	$5.74 \cdot 10^{-5}$ [bar]
	Pressure drops cold fluid (LH_2)	Δp_c^{pre}	$1.02 \cdot 10^{-4}$ [bar]
Main heater	Length	L_{main}	8.525 [m]
	Mass	m_{main}	406.2 [kJ/kg]
	Volume	V_{main}	$5.60 \cdot 10^{-4}$ [m^3]
	Pressure drops hot fluid (N_2)	Δp_h^{main}	0.064 [bar]
	Pressure drops cold fluid (GH_2)	Δp_c^{main}	0.059 [bar]

The length of the pre-heater is smaller (0.141 m) because the temperature difference between the two fluids is larger in the main heater. In both subunits, the pressure drops are negligible, as the optimal design point analysis was constrained to ensure a pressure drop of $\Delta p \leq 0.1$ bar for the hot and cold fluid.

Based on the values in **Table 29**, the total length, mass, and volume of the heat exchanger pipes are $L_{tot} = 8.666$ m, $m_{tot} = 412{,}9$ kg and $V_{tot} = 5.69 \cdot 10^{-4}$ m^3, respectively. These performance parameters are suitable for a fuel system application.

Moreover, with the heat exchanger's thermal power requirement at approximately 2 MW [144] and the theoretical power generated by fuel combustion at around 48 MW, it is possible conclude that the system is feasible. Specifically, the novel cryogenic heat exchanger operates with a negligible cost for energy use, as it only needs 4% of the thermal power generated by the engine. This is particularly efficient when considering that the overall efficiency of an aircraft engine is around 40%.

5. CONCLUSIONS

This PhD research has addressed the development of innovative technologies for low- and zero-carbon energy systems, focusing on two complementary pathways: the production of carbon-neutral fuels and the integration of hydrogen as an alternative energy carrier in advanced applications. The common guiding principle of the work has been the reduction of environmental impact through system-level optimization, compactness, and technological feasibility.

In the first part of the research, a novel biomethane liquefaction concept was investigated within the framework of small-scale applications. A simplified Single Mixed Refrigerant (SMR) cycle, conceptually inspired by the PRICO process, was developed with the objective of achieving competitive thermodynamic performance while reducing system complexity and capital costs. The adoption of a pipe-in-pipe heat exchanger architecture, which, to the best of the author's knowledge is not currently on the market, proved to be a viable alternative to more conventional cryogenic solutions, offering a favourable compromise between heat transfer performance and geometric compactness. Through a parametric and optimization-based analysis, key operating parameters were identified, allowing the simultaneous maximization of the overall coefficient of performance and the minimization of the total heat exchanger length. The obtained results confirm the potential of the proposed approach for small-scale biomethane liquefaction, contributing to the broader deployment of biofuels with a net-zero CO_2 footprint. The adopted approach has shown that careful fine-tuning of the operating parameters can significantly enhance system performance. This suggests that additional variables—such as the molar fractions of the species composing the refrigerant—could be incorporated into future simulations to further improve the objective functions.

Moreover, the proposed plant is currently in the final stage of construction at Sistemi Energetici, located in Foggia. As a result, experimental validation data will soon become available, providing valuable feedback on the simulation results and supporting further optimization of the plant.

The second part of the work focused on hydrogen as a clean energy carrier, with particular attention to its application in aviation. A preliminary hydrogen-based aircraft fuel system was proposed, addressing the critical challenges associated with liquid hydrogen storage, vaporization, and accurate mass flow metering. Due to the intrinsic physical properties of hydrogen, a dedicated modelling framework was developed to handle compressible flow conditions and phase change phenomena.

Special attention was devoted to key components of the hydrogen fuel system. The vaporizer heat exchanger was designed using the pipe-in-pipe architecture, allowing a significant reduction in the overall volume while ensuring adequate thermal performance and structural integrity under high-pressure conditions. To experimentally evaluate the performance predicted in this work, a dedicated test rig replicating the complete fuel system will be developed in collaboration with Avio Aero. The experimental data collected from this setup will be used to validate the results generated by the digital twin implemented in the Simulink environment.

In parallel, the Simulink model will be enhanced through several improvements to the component modelling. These include adopting a convergent–divergent nozzle as the metering valve, enabling choked flow conditions consistent with real operating scenarios; introducing a buffer in the hydrogen tank to better manage startup conditions; and

implementing a control system designed to regulate the hydrogen boil-off phenomenon while the fuel is stored in liquid form within the tank.

Overall, the results obtained in this research demonstrate that innovative system architectures, combined with analytical modelling, can provide effective solutions to some of the key challenges associated with the transition toward sustainable energy systems. The methodologies and technologies presented in this work represent a meaningful contribution to the fields of biofuel liquefaction and hydrogen fuel systems, and they lay the groundwork for future developments, including experimental scale-up, system integration, and techno-economic assessments aimed at real-world deployment.

References

[1] S. Dahlgren, "Biogas-based fuels as renewable energy in the transport sector: an overview of the potential of using CBG, LBG and other vehicle fuels produced from biogas," *Biofuels*, vol. 13, no. 5, pp. 587–599, May 2022, doi: 10.1080/17597269.2020.1821571.

[2] E. Barbera, S. Menegon, D. Banzato, C. D'Alpaos, and A. Bertucco, "From biogas to biomethane: A process simulation-based techno-economic comparison of different upgrading technologies in the Italian context," *Renew Energy*, vol. 135, pp. 663–673, May 2019, doi: 10.1016/j.renene.2018.12.052.

[3] R. Amirante and P. Catalano, "PH—Postharvest Technology," *Journal of Agricultural Engineering Research*, vol. 77, no. 2, pp. 193–201, Oct. 2000, doi: 10.1006/jaer.2000.0586.

[4] S. Mokhatab, J. Y. Mak, J. V. Valappil, and D. A. Wood, *Handbook of Liquefied Natural Gas*. Elsevier, 2014. doi: 10.1016/C2011-0-07476-8.

[5] A. Naquash, M. A. Qyyum, J. Haider, H. Lim, and M. Lee, "Renewable LNG production: Biogas upgrading through CO2 solidification integrated with single-loop mixed refrigerant biomethane liquefaction process," *Energy Convers Manag*, vol. 243, p. 114363, Sep. 2021, doi: 10.1016/J.ENCONMAN.2021.114363.

[6] F. Capra, F. Magli, and M. Gatti, "Biomethane liquefaction: A systematic comparative analysis of refrigeration technologies," *Appl Therm Eng*, vol. 158, p. 113815, Jul. 2019, doi: 10.1016/j.applthermaleng.2019.113815.

[7] R. Amirante, S. Bruno, E. Distaso, M. La Scala, and P. Tamburrano, "A biomass small-scale externally fired combined cycle plant for heat and power generation in rural communities," *Renewable Energy Focus*, vol. 28, pp. 36–46, Mar. 2019, doi: 10.1016/j.ref.2018.10.002.

[8] L. A. Catalano, F. De Bellis, R. Amirante, and M. Rignanese, "An immersed particle heat exchanger for externally fired and heat recovery gas turbines," *J Eng Gas Turbine Power*, vol. 133, no. 3, Mar. 2011, doi: 10.1115/1.4002157/478130.

[9] M. Prussi, M. Padella, M. Conton, E. D. Postma, and L. Lonza, "Review of technologies for biomethane production and assessment of Eu transport share in 2030," *J Clean Prod*, vol. 222, pp. 565–572, Jun. 2019, doi: 10.1016/j.jclepro.2019.02.271.

[10] S. F. Ferreira, L. S. Buller, M. Berni, and T. Forster-Carneiro, "Environmental impact assessment of end-uses of biomethane," *J Clean Prod*, vol. 230, pp. 613–621, Sep. 2019, doi: 10.1016/J.JCLEPRO.2019.05.034.

[11] N. Ben Yahmed, M. A. Jmel, M. Ben Alaya, H. Bouallagui, M. N. Marzouki, and I. Smaali, "A biorefinery concept using the green macroalgae Chaetomorpha linum for the coproduction of bioethanol and biogas," *Energy Convers Manag*, vol. 119, pp. 257–265, Jul. 2016, doi: 10.1016/J.ENCONMAN.2016.04.046.

[12] I. Doušková, F. Kaštánek, Y. Maléterová, P. Kaštánek, J. Doucha, and V. Zachleder, "Utilization of distillery stillage for energy generation and concurrent production of valuable microalgal biomass in the sequence: Biogas-cogeneration-microalgae-products," *Energy Convers Manag*, vol. 51, no. 3, pp. 606–611, Mar. 2010, doi: 10.1016/J.ENCONMAN.2009.11.008.

[13] M. Kaur, M. Kumar, D. Singh, S. Sachdeva, and S. K. Puri, "A sustainable biorefinery approach for efficient conversion of aquatic weeds into bioethanol and biomethane," *Energy Convers Manag*, vol. 187, pp. 133–147, May 2019, doi: 10.1016/J.ENCONMAN.2019.03.018.

[14] J. Zhang, H. Meerman, R. Benders, and A. Faaij, “Comprehensive review of current natural gas liquefaction processes on technical and economic performance,” *Appl Therm Eng*, vol. 166, p. 114736, Feb. 2020, doi: 10.1016/j.applthermaleng.2019.114736.

[15] N. Ghimire, R. Bakke, and W. H. Bergland, “Liquefaction of lignocellulosic biomass for methane production: A review,” *Bioresour Technol*, vol. 332, p. 125068, Jul. 2021, doi: 10.1016/J.BIORTECH.2021.125068.

[16] W. S. Cao, X. S. Lu, W. S. Lin, and A. Z. Gu, “Parameter comparison of two small-scale natural gas liquefaction processes in skid-mounted packages,” *Appl Therm Eng*, vol. 26, no. 8–9, pp. 898–904, Jun. 2006, doi: 10.1016/J.APPLTHERMALENG.2005.09.014.

[17] T. B. He and Y. L. Ju, “Performance improvement of nitrogen expansion liquefaction process for small-scale LNG plant,” *Cryogenics (Guildf)*, vol. 61, pp. 111–119, May 2014, doi: 10.1016/J.CRYOGENICS.2013.09.004.

[18] M. Omidi, M. Farhadi, and M. Jafari, “A comprehensive review on double pipe heat exchangers,” *Appl Therm Eng*, vol. 110, pp. 1075–1090, Jan. 2017, doi: 10.1016/j.applthermaleng.2016.09.027.

[19] T. Morosuk, S. Tesch, A. Hiemann, G. Tsatsaronis, and N. Bin Omar, “Evaluation of the PRICO liquefaction process using exergy-based methods,” *J Nat Gas Sci Eng*, vol. 27, pp. 23–31, Nov. 2015, doi: 10.1016/j.jngse.2015.02.007.

[20] D. Marmolejo-Correa and T. Gundersen, “A comparison of exergy efficiency definitions with focus on low temperature processes,” *Energy*, vol. 44, no. 1, pp. 477–489, Aug. 2012, doi: 10.1016/j.energy.2012.06.001.

[21] L. Castillo and C. A. Dorao, “Consensual decision-making model based on game theory for LNG processes,” *Energy Convers Manag*, vol. 64, pp. 387–396, Dec. 2012, doi: 10.1016/j.enconman.2012.06.014.

[22] X. Xu, J. Liu, C. Jiang, and L. Cao, “The correlation between mixed refrigerant composition and ambient conditions in the PRICO LNG process,” *Appl Energy*, vol. 102, pp. 1127–1136, Feb. 2013, doi: 10.1016/j.apenergy.2012.06.031.

[23] P. E. Wahl, S. W. Løvseth, and M. J. Mølnvik, “Optimization of a simple LNG process using sequential quadratic programming,” *Comput Chem Eng*, vol. 56, pp. 27–36, Sep. 2013, doi: 10.1016/j.compchemeng.2013.05.001.

[24] A. Morin, P. E. Wahl, and M. Mølnvik, “Using evolutionary search to optimise the energy consumption for natural gas liquefaction,” *Chemical Engineering Research and Design*, vol. 89, no. 11, pp. 2428–2441, Nov. 2011, doi: 10.1016/j.cherd.2011.03.002.

[25] T. B. He and Y. L. Ju, “A novel process for small-scale pipeline natural gas liquefaction,” *Appl Energy*, vol. 115, pp. 17–24, Feb. 2014, doi: 10.1016/j.apenergy.2013.11.016.

[26] A. Aspelund, T. Gundersen, J. Myklebust, M. P. Nowak, and A. Tomasgard, “An optimization-simulation model for a simple LNG process,” *Comput Chem Eng*, vol. 34, no. 10, pp. 1606–1617, Oct. 2010, doi: 10.1016/j.compchemeng.2009.10.018.

[27] M. S. Khan and M. Lee, “Design optimization of single mixed refrigerant natural gas liquefaction process using the particle swarm paradigm with nonlinear constraints,” *Energy*, vol. 49, pp. 146–155, Jan. 2013, doi: 10.1016/j.energy.2012.11.028.

[28] A. Mortazavi, A. Alabdulkarem, Y. Hwang, and R. Radermacher, “Development of a robust refrigerant mixture for liquefaction of highly uncertain natural gas compositions,” *Energy*, vol. 113, pp. 1042–1050, Oct. 2016, doi: 10.1016/j.energy.2016.07.147.

[29] X. Xu, J. Liu, L. Cao, and W. Pang, “Automatically varying the composition of a mixed refrigerant solution for single mixed refrigerant LNG (liquefied natural gas) process at changing working conditions,” *Energy*, vol. 64, pp. 931–941, Jan. 2014, doi: 10.1016/j.energy.2013.10.040.

[30] T. He *et al.*, “Black Hole-Inspired Optimal Design of Biomethane Liquefaction Process for Small-Scale Applications,” *Front Energy Res*, vol. 9, Apr. 2021, doi: 10.3389/fenrg.2021.656165.

[31] D. Popov *et al.*, “Cryogenic heat exchangers for process cooling and renewable energy storage: A review,” *Appl Therm Eng*, vol. 153, pp. 275–290, May 2019, doi: 10.1016/J.APPLTHERMALENG.2019.02.106.

[32] Q. S. Yin *et al.*, “ECONOMIC ANALYSIS OF MIXED-REFRIGERANT CYCLE AND NITROGEN EXPANDER CYCLE IN SMALL SCALE NATURAL GAS LIQUEFIER,” in *AIP Conference Proceedings*, AIP, Mar. 2008, pp. 1159–1165. doi: 10.1063/1.2908467.

[33] P. Tamburrano *et al.*, “Thermodynamic Analysis of a Small-scale Biomethane Liquefaction Process,” *J Phys Conf Ser*, vol. 2385, no. 1, p. 012043, Dec. 2022, doi: 10.1088/1742-6596/2385/1/012043.

[34] P. Tamburrano, E. Distaso, M. Salvatori, M. Fedele, M. Meschia, and R. Amirante, “A novel small-scale biomethane liquefaction process: Assessment through a detailed theoretical analysis,” *Appl Therm Eng*, vol. 233, p. 121145, Oct. 2023, doi: 10.1016/j.applthermaleng.2023.121145.

[35] T. D. Smith, “Hydrogen-powered flight,” 2005.

[36] H. Webber and S. Job, “REALISING ZERO-CARBON EMISSION FLIGHT Primary Energy Source Comparison and Selection,” 2021.

[37] P. Tamburrano *et al.*, “Fuels systems and components for future airliners fuelled with liquid hydrogen,” *J Phys Conf Ser*, vol. 2385, no. 1, p. 012041, Dec. 2022, doi: 10.1088/1742-6596/2385/1/012041.

[38] A. Plummer, D. Adeyemi, N. Sell, F. Sciatti, P. Tamburrano, and R. Amirante, “Fuel System Control for Hydrogen-Powered Aircraft,” *2024 UKACC 14th International Conference on Control, CONTROL 2024*, pp. 201–202, 2024, doi: 10.1109/CONTROL60310.2024.10532046.

[39] F. C. and H. J. Undertaking, “Hydrogen Powered Aviation: A Fact-based Study of Hydrogen Technology, Economics, and Climate Impact by 2050,” Jul. 2020, Accessed: Dec. 21, 2025. [Online]. Available: https://www.h2knowledgecentre.com/content/researchpaper1126

[40] V. Di Domenico, P. Tamburrano, E. Distaso, F. Sciatti, and R. Amirante, “Detailed performance analysis of a novel small-scale biomethane liquefaction plant,” *J Phys Conf Ser*, vol. 2648, no. 1, p. 012014, Dec. 2023, doi: 10.1088/1742-6596/2648/1/012014.

[41] F. Sciatti *et al.*, “PRELIMINARY DESIGN AND MODELLING OF A HYDROGEN-POWERED AIRCRAFT FUEL SYSTEM,” in *FPMC 2024*, 2024.

[42] V. Di Domenico, P. Tamburrano, F. Sciatti, E. Distaso, M. M. Foglia, and R. Amirante, “A Novel Hydrogen-Nitrogen Heat Exchanger For Aeronautical Applications,” *J Phys Conf Ser*, vol. 2893, no. 1, p. 012082, Nov. 2024, doi: 10.1088/1742-6596/2893/1/012082.

[43] F. Sciatti, V. Di Domenico, P. Tamburrano, E. Distaso, and R. Amirante, “An Innovative Cryogenic Heat Exchanger Design for Sustainable Aviation,” *Energies 2025, Vol. 18, Page 1261*, vol. 18, no. 5, p. 1261, Mar. 2025, doi: 10.3390/EN18051261.

[44] F. Sciatti, V. Di Domenico, P. Tamburrano, E. Caprioli, E. Distaso, and R. Amirante, "Simulation and Control of an Advanced Metering Valve for Hydrogen-Powered Aircraft Fuel Systems Using Simscape Language," *J Phys Conf Ser*, vol. 3143, no. 1, p. 012067, Dec. 2025, doi: 10.1088/1742-6596/3143/1/012067.

[45] V. Di Domenico, F. Sciatti, P. Tamburrano, E. Distaso, and R. Amirante, "Optimization of a novel biomethane small-scale liquefaction plant by means of a Multi-Objective Genetic Algorithm," *J Phys Conf Ser*, vol. 3143, no. 1, p. 012021, Dec. 2025, doi: 10.1088/1742-6596/3143/1/012021.

[46] F. Sciatti *et al.*, "Numerical Analysis of a High-Power Piezoelectric Pump using Computational Fluid Dynamics (CFD) Simulations," *Lecture Notes in Mechanical Engineering*, pp. 289–303, 2025, doi: 10.1007/978-3-031-84505-5_19/FIGURES/7.

[47] W. Lim, K. Choi, and I. Moon, "Current Status and Perspectives of Liquefied Natural Gas (LNG) Plant Design," *Ind Eng Chem Res*, vol. 52, no. 9, pp. 3065–3088, Mar. 2013, doi: 10.1021/IE302877G.

[48] P. Bosma and R. K. Nagelvoort, "Liquefaction Technology; Developments through History," *Proceedings of the 1st Annual Gas Processing Symposium*, pp. 19–31, Jan. 2009, doi: 10.1016/B978-0-444-53292-3.50006-7.

[49] "Developments in natural gas liquefaction." Accessed: Dec. 27, 2025. [Online]. Available: https://www.hydrocarbonprocessing.com/magazine/1999/april-1999/special-report-gas-processing-developments/developments-in-natural-gas-liquefaction

[50] "Natural Gas Liquefaction Processes Comparison | PDF | Heat Exchanger | Liquefied Natural Gas." Accessed: Dec. 28, 2025. [Online]. Available: https://it.scribd.com/document/47392340/NATURAL-GAS-LIQUEFACTION-PROCESSES-COMPARISON

[51] D. L. Andress, "THE PHILLIPS OPTIMIZED CASCADE LNG PROCESS A QUARTER CENTURY OF IMPROVEMENTS," 1996.

[52] "Our Technology and Expertise are Ready to Work Toward Your LNG Project Today Optimized Cascade Process LNG Plant Locations".

[53] M. F. M. Fahmy, H. I. Nabih, and M. El-Nigeily, "Enhancement of the efficiency of the Open Cycle Phillips Optimized Cascade LNG process," *Energy Convers Manag*, vol. 112, pp. 308–318, Mar. 2016, doi: 10.1016/J.ENCONMAN.2016.01.022.

[54] F. Are Michelsen, I. Johan Halvorsen, B. Floor Lund, and P. Eilif Wahl, "Modeling and Simulation for Control of the TEALARC Liquified Natural Gas Process", doi: 10.1021/ie901650e.

[55] T. Morosuk, S. Tesch, A. Hiemann, G. Tsatsaronis, and N. Bin Omar, "Evaluation of the PRICO liquefaction process using exergy-based methods," *J Nat Gas Sci Eng*, vol. 27, pp. 23–31, Nov. 2015, doi: 10.1016/J.JNGSE.2015.02.007.

[56] A. Singh and M. Hovd, "Dynamic Modeling and Control of the PRICO © LNG process".

[57] P. M., L. Y. N., P. J., and et al., "The C3MR liquefaction cycle: versatility for a fast growing, ever changing LNG industry.," *LNG 15. Proceedings of the 15th International Conference and Exhibition of Liquefied Natural Gas.*, 2007, Accessed: Jan. 04, 2026. [Online]. Available: https://iifiir.org/en/fridoc/the-c3mr-liquefaction-cycle-versatility-for-a-fast-growing-ever-25093

[58] "Unusual design considerations drive selection of Sakhalin LNG plant facilities." Accessed: Jan. 05, 2026. [Online]. Available: https://www.researchgate.net/publication/292857613_Unusual_design_considerations_drive_selection_of_Sakhalin_LNG_plant_facilities

[59] U. S. Patent, “Hybrid cycle for the production of liquefied natural gas,” Oct. 1999.
[60] E. Berger, W. Forg, R. S. Heiersted, and P. Paurola, “The Snohvit Project: The MFC®(Mixed Fluid Cascade) Process for the first European Baseload LNG Production Plant,” *Linde Technology*, pp. 12–23, 2003.
[61] K. J. Vink and R. K. Nagelvoort, “Baseload liquefaction processes,” *Hydrocarbon Engineering*, vol. 3, no. 9, pp. 30–37, 1998.
[62] A. J. Finn, G. L. Johnson, and T. R. Tomlinson, “LNG technology for offshore and mid-scale plants,” in *79th Annual GPA Convention, Atlanta*, 2000.
[63] A. J. Finn, “Effective LNG production offshore,” in *81st annual GPA convention*, 2002, pp. 10–13.
[64] J. H. Foglietta, “Consider dual independent expander refrigeration for LNG production: new methodology may enable reducing cost to produce stranded gas,” *Hydrocarbon Processing*, vol. 83, no. 1, pp. 39–45, 2004.
[65] J. H. Foglietta -Manager, “Production of LNG using Dual Independent Expander Refrigeration Cycles”.
[66] C. W. Remeljej and A. F. A. Hoadley, “An exergy analysis of small-scale liquefied natural gas (LNG) liquefaction processes,” *Energy*, vol. 31, no. 12, pp. 2005–2019, Sep. 2006, doi: 10.1016/J.ENERGY.2005.09.005.
[67] S. Walther and P. E., “A new generation of liquefaction processes for LNG FPSO applications. In International Gas Union Research Conference, Paris, October 08, 2008.,” in *International Gas Union Research Conference*, Paris, Nov. 2008.
[68] I. B. Waldmann, “Evaluation of process systems for floating LNG production units,” in *Tekna conference*, 2008.
[69] “Small Scale and MiniLNGTM Systems - Hamworthy.” Accessed: Jan. 05, 2026. [Online]. Available: https://www.yumpu.com/en/document/read/2844918/small-scale-and-minilngtm-systems-hamworthy
[70] “Selecting Offshore LNG Processes: Engineering Forum | PDF | Liquefied Natural Gas | Natural Gas.” Accessed: Jan. 05, 2026. [Online]. Available: https://it.scribd.com/document/360652167/LNJ091105p34-36-pdf
[71] “Skyward Action Realizing Aviation’s Sustainable Future 2025 ICAO Environmental Report.”
[72] F. C. and H. J. Undertaking, “Hydrogen Powered Aviation: A Fact-based Study of Hydrogen Technology, Economics, and Climate Impact by 2050,” Jul. 2020, Accessed: Jan. 06, 2026. [Online]. Available: https://www.h2knowledgecentre.com/content/researchpaper1126
[73] “Net zero 2050: sustainable aviation fuels (SAF)”, [Online]. Available: https://www.iata.org/en/iata-repository/pressroom/fact-sheets/fact-sheet-sustainable-aviation-fuels/
[74] “A ROUTE TO NET ZERO EUROPEAN AVIATION,” 2025. Accessed: Jan. 06, 2026. [Online]. Available: https://www.destination2050.eu/wp-content/uploads/2025/02/DESTINATION_2050_Roadmap_2025.pdf
[75] “How SAF mandates in the EU and UK are reshaping aviation fuel markets | Carbon Direct.” Accessed: Jan. 06, 2026. [Online]. Available: https://www.carbon-direct.com/insights/how-saf-mandates-in-the-eu-and-uk-are-reshaping-aviation-fuel-markets
[76] “The Role of Sustainable Aviation Fuel in Decarbonizing the Aviation Industry.” Accessed: Jan. 06, 2026. [Online]. Available: https://insights.issgovernance.com/posts/the-role-of-sustainable-aviation-fuel-in-decarbonizing-the-aviation-industry/

[77] “Skyward Action Realizing Aviation’s Sustainable Future 2025 ICAO Environmental Report”.
[78] “Sustainable fuel alone unlikely to decarbonise the aviation industry - Carbon Tracker Initiative.” Accessed: Jan. 06, 2026. [Online]. Available: https://carbontracker.org/sustainable-fuel-alone-unlikely-to-decarbonise-the-aviation-industry/
[79] “Towards Disruptive Technologies for new Generation Aircraft by 2035,” 2024.
[80] “2024 HIGHLIGHTS”.
[81] “European ATM Master Plan”.
[82] “Research Report of Material Compatibility for Liquid Hydrogen Storage on Marine Application,” 2023.
[83] A. K. Boddorff, “Choosing the Right Stuff: Material Selection for Liquid Hydrogen Aircraft Cryotanks,” 2025, Accessed: Jan. 06, 2026. [Online]. Available: http://www.sti.nasa.gov
[84] “Phoebus project advances composite hydrogen tank testing for Ariane 6.” Accessed: Jan. 06, 2026. [Online]. Available: https://www.spacedaily.com/reports/Phoebus_project_advances_composite_hydrogen_tank_testing_for_Ariane_6_999.html
[85] R. Grugel, “Evaluation of Carbon Composite Overwrap Pressure Vessels Fabricated Using Ionic Liquid Epoxies Project,” 2015.
[86] National Aeronautics and Space Administration, “SAFETY STANDARD FOR HYDROGEN AND HYDROGEN SYSTEMS,” 1997.
[87] J. J. Martin and L. H. Marshall, “Large-Scale Liquid Hydrogen Testing of a Variable Density Multilayer Insulation With a Foam Substrate”, Accessed: Jan. 06, 2026. [Online]. Available: www.sti.nasa.gov
[88] A. Aasen, S. Blakseth, A. Massing, P. Nekså, and M. A. Gjennestad, “Thermal performance estimation for cryogenic storage tanks: Application to liquid hydrogen”.
[89] A. Jacobson and I. Storage Solutions, “Liquid Hydrogen Storage Technologies,” 2022.
[90] W. U. Notardonato, A. M. Swanger, J. E. Fesmire, K. M. Jumper, W. L. Johnson, and T. M. Tomsik, “Zero Boil-Off Methods for Large Scale Liquid Hydrogen Tanks using Integrated Refrigeration and Storage”.
[91] “ZEROe: our hydrogen-powered aircraft | Airbus.” Accessed: Jan. 06, 2026. [Online]. Available: https://www.airbus.com/en/innovation/energy-transition/hydrogen/zeroe-our-hydrogen-powered-aircraft
[92] “Advancing Hydrogen Aviation in 2025 | ZeroAvia.” Accessed: Jan. 06, 2026. [Online]. Available: https://zeroavia.com/blogs/advancing-hydrogen-aviation-in-2025-the-4-pillars-of-success/
[93] “Aviation sector’s climate claims unsupported by credible transition plans - Carbon Tracker Initiative.” Accessed: Jan. 06, 2026. [Online]. Available: https://carbontracker.org/aviation-sectors-climate-claims-unsupported-by-credible-transition-plans/
[94] L. Cao, J. Liu, and X. Xu, “Robustness analysis of the mixed refrigerant composition employed in the single mixed refrigerant (SMR) liquefied natural gas (LNG) process,” *Appl Therm Eng*, vol. 93, pp. 1155–1163, Jan. 2016, doi: 10.1016/J.APPLTHERMALENG.2015.10.072.
[95] D. Taler and J. Taler, “Simple heat transfer correlations for turbulent tube flow,” in *E3S Web of Conferences*, 2017. doi: 10.1051/e3sconf/20171302008.
[96] Y. A. Çengel, “Introduction to thermodynamics and heat transfer / Yunus A. Cengel.,” *Introduction to thermodynamics and heat transfer /*, 2008.

[97] J. C. Chen, “Correlation for boiling heat transfer to saturated fluids in convective flow,” *Industrial and Engineering Chemistry Process Design and Development*, 1966, doi: 10.1021/i260019a023.
[98] V. Di Domenico, F. Sciatti, P. Tamburrano, E. Distaso, and R. Amirante, “Optimization of a novel biomethane small-scale liquefaction plant by means of a Multi-Objective Genetic Algorithm,” *J Phys Conf Ser*, vol. 3143, no. 1, p. 012021, Dec. 2025, doi: 10.1088/1742-6596/3143/1/012021.
[99] P. Tamburrano, E. Distaso, M. Salvatori, M. Fedele, M. Meschia, and R. Amirante, “A novel small-scale biomethane liquefaction process: Assessment through a detailed theoretical analysis,” *Appl Therm Eng*, vol. 233, Oct. 2023, doi: 10.1016/j.applthermaleng.2023.121145.
[100] G. Caramia and A. Dadone, “A General Purpose Adjoint Formulation for Inviscid 2D/3D Fluid Dynamic Optimization,” *10th AIAA Multidisciplinary Design Optimization Conference*, Jan. 2014, doi: 10.2514/6.2014-1174.
[101] M. D. McKay, R. J. Beckman, and W. J. Conover, “A Comparison of Three Methods for Selecting Values of Input Variables in the Analysis of Output from a Computer Code,” *Technometrics*, vol. 21, no. 2, p. 239, May 1979, doi: 10.2307/1268522.
[102] E. Rigoni and S. Poles, “NBI and MOGA-II, two complementary algorithms for multi-objective optimizations,” in *Dagstuhl seminar proceedings*, Schloss Dagstuhl-Leibniz-Zentrum für Informatik, 2005.
[103] S. Poles, E. Rigoni, and T. Robic, “MOGA-II performance on noisy optimization problems,” in *International Conference on Bioinspired Optimization Methods and their Applications, Ljubljana, Slovenia*, 2004.
[104] Accessed on April 2024, “https://engineering.esteco.com/modefrontier/.”
[105] T. D. Smith, “Hydrogen-powered flight,” 2005.
[106] H. Webber and S. Job, “Realising Zero-Carbon Emission Flight. Primary Energy Source Comparison and Selection,” 2021.
[107] P. Tamburrano *et al.*, “Fuels systems and components for future airliners fuelled with liquid hydrogen,” *J Phys Conf Ser*, vol. 2385, no. 1, p. 012041, Dec. 2022, doi: 10.1088/1742-6596/2385/1/012041.
[108] A. Plummer, D. Adeyemi, N. Sell, F. Sciatti, P. Tamburrano, and R. Amirante, “Fuel System Control for Hydrogen-Powered Aircraft,” in *2024 UKACC 14th International Conference on Control (CONTROL)*, IEEE, 2024, pp. 201–202.
[109] H. J. Undertaking, “Hydrogen powered aviation: A fact-based study of hydrogen technology, economics, and climate impact by 2050,” 2020.
[110] Parker Aerospace, “Partnership Developing Liquid Hydrogen Fuel Systems for Zero Emission Aircraft,” Online.
[111] N. Morioka and H. Oyori, “More Electric Architecture for Engine and Aircraft Fuel System,” *SAE Technical Papers*, vol. 8, Sep. 2013, doi: 10.4271/2013-01-2080.
[112] O. D. Lyantsev, T. V. Breikin, G. G. Kulikov, and V. Y. Arkov, “On-line performance optimisation of aero engine control system,” *Automatica*, vol. 39, no. 12, pp. 2115–2121, Dec. 2003, doi: 10.1016/S0005-1098(03)00224-3.
[113] H. Oyori, N. Morioka, M. Seta, Y. Shimomura, and H. Saito, “A Motor Control Design for the More Electric Aero Engine Fuel System,” *SAE Technical Papers*, Oct. 2011, doi: 10.4271/2011-01-2619.
[114] G. D. Brewer, R. E. Morris, G. W. Davis, E. F. Versaw, and J. G. R. Cunnington, “Study of fuel systems for LH2-fueled subsonic transport aircraft. Volume 1. Final report, September 1976--December 1977,” Jul. 01, 1978.

[115] G. D. Brewer *et al.*, “Study of fuel systems for LH2-fueled subsonic transport aircraft, volume 2,” 1978.
[116] D. B. Doman, “Optimal Cruise Altitude for Aircraft Thermal Management,” *https://doi.org/10.2514/1.G000845*, vol. 38, no. 11, pp. 2084–2095, Jun. 2015, doi: 10.2514/1.G000845.
[117] R. Langton, C. Clark, M. Hewitt, L. Richards, I. Moir, and A. Seabridge, *Aircraft fuel systems*. John Wiley & Sons, 2009.
[118] M. Montazeri-Gh and S. Jafari, “Evolutionary Optimization for Gain Tuning of Jet Engine Min-Max Fuel Controller,” *https://doi.org/10.2514/1.B34185*, vol. 27, no. 5, pp. 1015–1023, Sep. 2013, doi: 10.2514/1.B34185.
[119] B. Wang, H. Zhao, and Z. Ye, “A Co-modeling Method Based on Component Features for Mechatronic Devices in Aero-engines,” *International Journal of Turbo and Jet Engines*, vol. 34, no. 3, pp. 255–267, Aug. 2017, doi: 10.1515/TJJ-2016-0007/MACHINEREADABLECITATION/RIS.
[120] G. D. Brewer, “Hydrogen aircraft technology,” *Hydrogen Aircraft Technology*, pp. 1–432, Jan. 2017, doi: 10.1201/9780203751480/HYDROGEN-AIRCRAFT-TECHNOLOGY-DANIEL-BREWER.
[121] A. E. Biermann and R. C. Kohl, “Preliminary Study of a Piston Pump for Cryogenic Fluids,” 1959.
[122] A. E. Bierman and W. G. Shinko, “Performance of a Piston Type Pump for Liquid Hydrogen,” *NASA Technical Note D-276*, 1960.
[123] J. S. Goldsmith and G. W. Bennett, “Hydrogen-methane fuel control systems for turbojet engines,” 1973.
[124] F. Sciatti, P. Tamburrano, E. Distaso, and R. Amirante, “Modelling of the Entire Aircraft Fuel System Through Simulink for Accurate Performance Evaluation,” *Proceedings of ASME/BATH 2023 Symposium on Fluid Power and Motion Control, FPMC 2023*, Nov. 2023, doi: 10.1115/FPMC2023-111795.
[125] F. Sciatti, P. Tamburrano, P. De Palma, E. Distaso, and R. Amirante, “Detailed simulations of an aircraft fuel system by means of Simulink,” in *Journal of Physics: Conference Series*, IOP Publishing, 2022, p. 012033.
[126] Y. Wang, D. Fan, C. Zhang, K. Peng, and D. Shi, “Design and analysis of the variable pressure-drop fuel metering device,” *Chinese Control Conference, CCC*, pp. 6434–6439, Sep. 2017, doi: 10.23919/CHICC.2017.8028379.
[127] P. Tamburrano, F. Sciatti, A. R. Plummer, E. Distaso, P. De Palma, and R. Amirante, “A Review of Novel Architectures of Servovalves Driven by Piezoelectric Actuators,” *Energies 2021, Vol. 14, Page 4858*, vol. 14, no. 16, p. 4858, Aug. 2021, doi: 10.3390/EN14164858.
[128] P. Tamburrano, P. De Palma, A. R. Plummer, E. Distaso, F. Sciatti, and R. Amirante, “Simulation of a high frequency on/off valve actuated by a piezo-ring stack for digital hydraulics,” *E3S Web of Conferences*, vol. 312, p. 05008, Oct. 2021, doi: 10.1051/E3SCONF/202131205008.
[129] F. Sciatti, P. Tamburrano, E. Distaso, and R. Amirante, “Digital hydraulic valves: Advancements in research,” 2024, doi: 10.1016/j.heliyon.2024.e27264.
[130] F. Sciatti, P. Tamburrano, E. Distaso, and R. Amirante, “Digital hydraulic technology: applications, challenges, and future direction,” in *Journal of Physics: Conference Series*, IOP Publishing, 2023, p. 012053.
[131] P. Tamburrano, E. Distaso, A. R. Plummer, F. Sciatti, P. De Palma, and R. Amirante, “Direct drive servovalves actuated by amplified piezo-stacks: Assessment through a

detailed numerical analysis," *Actuators*, vol. 10, no. 7, Jul. 2021, doi: 10.3390/act10070156.
[132] P. Tamburrano, F. Sciatti, E. Distaso, and R. Amirante, "Comprehensive Numerical Analysis of a Four-Way Two-Position (4/2) High-Frequency Switching Digital Hydraulic Valve Driven by a Ring Stack Actuator," *Energies (Basel)*, vol. 16, no. 21, p. 7355, 2023.
[133] A. Westenberger, "Liquid hydrogen fuelled aircraft-system analysis," *CRYOPLANE, The European Commission, Brussels, Belgium, Report No. GRD1-1999-10014*, 2003.
[134] "MathWorks - Creatori di MATLAB e Simulink - MATLAB e Simulink - MATLAB & Simulink." Accessed: Mar. 27, 2024. [Online]. Available: https://it.mathworks.com/
[135] I. H. Bell, J. Wronski, S. Quoilin, and V. Lemort, "Pure and pseudo-pure fluid thermophysical property evaluation and the open-source thermophysical property library coolprop," *Ind Eng Chem Res*, vol. 53, no. 6, pp. 2498–2508, Feb. 2014, doi: 10.1021/IE4033999/SUPPL_FILE/IE4033999_SI_002.ZIP.
[136] P. Beater, "Pneumatic drives: System design, modelling and control," *Pneumatic Drives: System Design, Modelling and Control*, pp. 1–323, 2007, doi: 10.1007/978-3-540-69471-7/COVER.
[137] M. Yamaguchi, K. Takahashi, and T. Ohmori, "Thermal conductivity of polyurethane foam at liquid hydrogen temperature region," *Advances in Cryogenic Engineering: Part A*, pp. 117–122, 1996.
[138] W. J. Buttner, M. Ciotti, K. Hartmann, K. Schmidt, H. Wright, and E. Weidner, "Empirical profiling of cold hydrogen plumes formed from venting of LH2 storage vessels," *Int J Hydrogen Energy*, vol. 46, no. 64, pp. 32723–32734, 2021.
[139] M. Coutinho *et al.*, "A review on the recent developments in thermal management systems for hybrid-electric aircraft," *Appl Therm Eng*, vol. 227, p. 120427, 2023.
[140] A. C. Patrao, I. Jonsson, C. Xisto, A. Lundbladh, M. Lejon, and T. Grönstedt, "The heat transfer potential of compressor vanes on a hydrogen fueled turbofan engine," *Appl Therm Eng*, vol. 236, p. 121722, 2024.
[141] G. D. Brewer, *Hydrogen aircraft technology*. CRC Press, 1991. doi: 10.1201/9780203751480/HYDROGEN-AIRCRAFT-TECHNOLOGY-DANIEL-BREWER.
[142] "ZEROe | Airbus." Accessed: Feb. 28, 2025. [Online]. Available: https://www.airbus.com/en/innovation/energy-transition/hydrogen/zeroe
[143] A. Plummer, D. Adeyemi, N. Sell, F. Sciatti, P. Tamburrano, and R. Amirante, "Fuel System Control for Hydrogen-Powered Aircraft," in *2024 UKACC 14th International Conference on Control (CONTROL)*, IEEE, Apr. 2024, pp. 201–202. doi: 10.1109/CONTROL60310.2024.10532046.
[144] F. Sciatti *et al.*, "Preliminary Design and Modelling of a Hydrogen-Powered Aircraft Fuel System," in *Fluid Power Systems Technology*, American Society of Mechanical Engineers, 2024, p. V001T01A028.
[145] F. Sciatti, P. Tamburrano, E. Distaso, and R. Amirante, "Modelling of the Entire Aircraft Fuel System Through Simulink for Accurate Performance Evaluation," in *Fluid Power Systems Technology*, American Society of Mechanical Engineers, 2023, p. V001T01A050.
[146] F. Sciatti, P. Tamburrano, E. Distaso, and R. Amirante, "Digital Hydraulic Technology: Applications, Challenges, and Future Direction," in *Journal of Physics: Conference Series*, IOP Publishing, 2023, p. 012053.

[147] P. Tamburrano, P. De Palma, A. R. Plummer, E. Distaso, F. Sciatti, and R. Amirante, “Simulation of a high frequency on/off valve actuated by a piezo-ring stack for digital hydraulics,” 2021.
[148] P. Łapka, M. Seredyński, and A. Ćwik, “Preliminary study on supercritical hydrogen and bleed air heat exchanger for aircraft application,” *Proc Inst Mech Eng G J Aerosp Eng*, vol. 232, no. 12, pp. 2231–2243, 2018.
[149] M. Vietze and C. Evrim, “Development of additively manufactured cryogenic heat exchangers for hydrogen-electric aircraft propulsion,” in *IOP Conference Series: Materials Science and Engineering*, IOP Publishing, 2024, p. 012007.
[150] A. C. Patrao, I. Jonsson, C. Xisto, A. Lundbladh, and T. Grönstedt, “Compact heat exchangers for hydrogen-fueled aero engine intercooling and recuperation,” *Appl Therm Eng*, vol. 243, p. 122538, 2024.
[151] V. Di Domenico, P. Tamburrano, F. Sciatti, E. Distaso, M. M. Foglia, and R. Amirante, “A Novel Hydrogen-Nitrogen Heat Exchanger For Aeronautical Applications,” in *Journal of Physics: Conference Series*, IOP Publishing, 2024, p. 012082.
[152] O. Olumayegun, M. Wang, and G. Kelsall, “Thermodynamic analysis and preliminary design of closed Brayton cycle using nitrogen as working fluid and coupled to small modular Sodium-cooled fast reactor (SM-SFR),” *Appl Energy*, vol. 191, pp. 436–453, 2017.
[153] X. Zhang, R. Tiwari, A. H. Shooshtari, and M. M. Ohadi, “An additively manufactured metallic manifold-microchannel heat exchanger for high temperature applications,” *Appl Therm Eng*, vol. 143, pp. 899–908, 2018.
[154] I. H. Bell, J. Wronski, S. Quoilin, and V. Lemort, “Pure and Pseudo-pure Fluid Thermophysical Property Evaluation and the Open-Source Thermophysical Property Library CoolProp,” *Ind Eng Chem Res*, vol. 53, no. 6, pp. 2498–2508, Feb. 2014, doi: 10.1021/ie4033999.
[155] A. Riaz, M. A. Qyyum, A. Hussain, and M. Lee, “Significance of ortho-para hydrogen conversion in the performance of hydrogen liquefaction process,” *Int J Hydrogen Energy*, vol. 48, no. 68, pp. 26568–26582, 2023.
[156] J. Teng *et al.*, “Comparative study on thermodynamic performance of hydrogen liquefaction processes with various ortho-para hydrogen conversion methods,” *Energy*, vol. 271, p. 127016, May 2023, doi: 10.1016/J.ENERGY.2023.127016.
[157] L. Yin and Y. Ju, “Review on the design and optimization of hydrogen liquefaction processes,” *Frontiers in Energy*, vol. 14, no. 3, pp. 530–544, Sep. 2020, doi: 10.1007/S11708-019-0657-4/METRICS.
[158] Y. A. Çengel, *Introduction to thermodynamics and heat transfer*. McGraw-Hill, 2008.
[159] D. Taler and J. Taler, “Simple heat transfer correlations for turbulent tube flow,” *E3S Web of Conferences*, vol. 13, p. 02008, Feb. 2017, doi: 10.1051/e3sconf/20171302008.
[160] G. D. Brewer, *Hydrogen aircraft technology*. Routledge, 2017.
[161] J. Liu, M. Zhao, and L. Rong, “Overview of hydrogen-resistant alloys for high-pressure hydrogen environment: on the hydrogen energy structural materials,” *Clean Energy*, vol. 7, no. 1, pp. 99–115, Feb. 2023, doi: 10.1093/CE/ZKAD009.
[162] C. S. Marchi and B. P. Somerday, “Comparison of Stainless Steels for High-Pressure Hydrogen Service,” *American Society of Mechanical Engineers, Pressure Vessels and Piping Division (Publication) PVP*, vol. 6B, Nov. 2014, doi: 10.1115/PVP2014-28811.